UNIVERSITÉ DE STRASBOURG

Thèse d'astrophysique

Chemodynamical Simulations of Evolution of Galaxies
Implementing a dust model

Observatoire astronomique de Strasbourg
École doctorale des sciences de la terre, de l'univers et de l'environnement
Université de Strasbourg

Nicolas Gaudin
Directeur de thèse : Hervé Wozniak
Rapporteurs: Samuel Boissier, Frédéric Bournaud, Ariane Lançon
Membres du jury: Éric Emsellem, Hervé Wozniak

Soutenance le 18 avril 2013

Abstract

Numerical simulations are a useful tool to understand the complex and non-linear behaviour of galaxies. By using simple N-body calculations they increase our understanding of simple stellar systems like globular clusters or the (dark matter) history of our universe. Chemodynamical simulations are designed to describe intermediate level systems: galaxies. For these bounded stellar systems, in addition to gravitation, other processes must be included: star formation, feedback of newly formed and evolving stars, metal enrichment, cooling of the interstellar medium, etc. Historically semi-analatic calculations have shown their ability to describe the chemical evolution of galaxies using simple, and often strong, assumptions on involved processes. But recent years reveal that processes related to gravitational interactions and chemical enrichment can be mixed in a complex manner, and previous tools show their limits. Then, chemodynamical simulations have to take the best of two worlds, pure N-body simulations and semi-analytic calculations of galactic evolution, to describe in a self-consistent way the dynamical and chemical evolution of galaxies.

In this thesis I use chemodynamical simulations to build up a model of evolution of the dust mass in our Galaxy and in dwarf galaxies. I have searched for dust (re-)processing by stars and in the interstellar medium, using both observations and results from semi-analytic models (eliminating few of their assumptions). Once my model was set up, I have performed simulations of a massive galaxy to understand local effects on dust evolution. Simulations of dwarf galaxies have been carried out to follow the dust mass in low metallicity environments. Comparisons with observations have been performed.

This work is a first step in order to address issues about dust evolution, processing, and properties by using simulations. Our main goal is to show how chemodynamical simulations are useful in order to help to solve these problems. Indeed, the processes relevant for dust production and destruction are still under debate. We confirm that 1–10 % of the dust mass is produced by stars and I also show accretion, eg. dust production in ISM, is necessary to balance dust destruction by SNII. Our results suggest SNe production accelerates the dust mass evolution by few hundred of Myrs. AGB production with accretion could therefore be enough to explain high dust masses in quasars at high redshift. Moreover, in the spectral energy distribution of galaxies a submillimeter excess appears, especially for dwarf, low metallicity galaxies. The origin of this excess is poorly known. Thus, the derived dust mass of a galaxy depends on the assumed origin. Simulations are able to reproduce the dust under-abundance of dwarf galaxies. According to this result, it is not necessary to introduce an additional mass of dust to explain the submillimeter excess. This demonstrates simulations are able to bring new constraints on the dust mass in galaxies. Finally the dust distribution inside galaxies is available. This allows to produce profiles and maps of the dust-to-oxygen mass ratio. Simulations show that we need to properly include localized SNII destruction of dust as well as dust transport on galactic scales. Indeed, profiles and/or gradients are affected by the star formation history and by galactic winds.

To conclude, chemodynamical simulations have shown that they are useful to design and implement a model for dust mass evolution. They allow a galactic view of dust mass as well as an insight into the simulated galaxies. Local effects and transport mechanisms are naturally included and turn out to be important for a model of dust mass production and destruction.

Contents

1 Introduction **1**
- 1.1 Historical review . . . 1
- 1.2 Dust . . . 2

2 Galaxies and dust **5**
- 2.1 Galaxies . . . 5
  - 2.1.1 Introduction . . . 5
  - 2.1.2 Morphology . . . 5
  - 2.1.3 Kinematics . . . 5
  - 2.1.4 Stars . . . 6
  - 2.1.5 The interstellar medium . . . 6
- 2.2 The Milky Way . . . 8
  - 2.2.1 The stellar component . . . 8
  - 2.2.2 The gaseous component . . . 9
- 2.3 Dwarf galaxies . . . 9
- 2.4 Dust . . . 10
  - 2.4.1 Effects on radiation . . . 10
  - 2.4.2 Composition . . . 11
  - 2.4.3 Box model . . . 11
  - 2.4.4 Production and destruction . . . 13
  - 2.4.5 Observations . . . 13

3 Chemodynamical Code **19**
- 3.1 Overview . . . 19
  - 3.1.1 Interaction of gas and stars . . . 20
- 3.2 Dust Mass Evolution . . . 22
  - 3.2.1 The model . . . 22
  - 3.2.2 Production . . . 22
  - 3.2.3 Accretion . . . 24
  - 3.2.4 Destruction . . . 30

4 First Result: The Milky Way **32**
- 4.1 Simulation . . . 32
- 4.2 Analysis . . . 33
  - 4.2.1 Radial distribution of dust . . . 33
  - 4.2.2 Vertical distribution of dust . . . 36
  - 4.2.3 Evolution of the dust-to-gas ratio . . . 38
  - 4.2.4 Evolution of the dust-to-oxygen ratio . . . 38

4.2.5 Dust–metallicity diagram . . . 39
4.2.6 Other diagrams . . . 41

5 Second Result: The Dwarf Galaxies 46
5.1 Simulations . . . 46
5.1.1 Dark matter . . . 46
5.1.2 Stellar and gaseous components . . . 47
5.1.3 Summary . . . 48
5.2 Analysis . . . 53
5.2.1 Evolution of the dust-to-oxygen ratio . . . 53
5.2.2 Maps of the dust-to-oxygen ratio . . . 55
5.2.3 Local correlation . . . 58
5.2.4 Global correlation . . . 61

6 Conclusion 63

A Improvement 71

B Parallelization 75

List of Figures

2.1 Sketch of the dust processes. . . . 14
2.2 Dust–oxygen diagram with observations . . . 17

3.1 Dust returned into ISM by stellar populations . . . 23
3.2 Accretion resolving full partial differential equations . . . 26
3.3 MC mass distribution of massive galaxies . . . 28
3.4 MC lifetime distribution . . . 29

4.1 Dust-to-oxygen gradients . . . 34
4.2 Radial gaseous flow . . . 35
4.3 Evolution of radial dust-to-oxygen ratio . . . 36
4.4 Vertical gradients . . . 37
4.5 Evolution of dust abundance and SFR . . . 39
4.6 Evolution of dust-to-oxygen ratio and SFR . . . 40
4.7 *Global* dust–oxygen diagram . . . 42
4.8 *Local* dust–oxygen diagrams . . . 43
4.9 *Global* dust–iron diagram . . . 44
4.10 *Local* dust/O–O/Fe diagram . . . 45

5.1 Dark core radius vs. density in dwarf galaxies . . . 47
5.2 Mass of stars+gas and dark core of dwarf galaxies . . . 48
5.3 Scale length and mass of stellar disc of dwarf galaxies . . . 49
5.4 Examples of HI fit . . . 50
5.5 Map of a dwarf galaxies. . . . 53
5.6 Dust-to-oxygen evolution of dwarf galaxies. . . . 54
5.7 xy dust-to-oxygen maps of `caaa` around 1 Gyr. . . . 56
5.8 z dust-to-oxygen maps of `caaa`. . . . 57
5.9 R dust-to-oxygen maps of `caaa`. . . . 58
5.10 Local dust–oxygen diagrams of `caab` . . . 59
5.11 Local dust–oxygen diagram of `caae` . . . 60
5.12 Star formation rate of dwarf galaxies . . . 61
5.13 Global dust–oxygen diagrams of dwarf galaxies . . . 62

A.1 Jenkins (2009) depletion rate and the model . . . 73

List of Tables

1 Overview of the frequently used symbols x
2 Overview of the acronyms. x

3.1 Parameters for the size distribution of grains 25
3.2 Power law index of MC mass distribution of dwarf galaxies 27
3.3 MC lifetime statistics in simulations 29

4.1 Parameters for dust model for each run. 33

5.1 Dark core mass of dwarf galaxies 47
5.2 Stellar and HI scale length 49
5.3 Major parameters for simulations of dwarf galaxies and `caaf`, a medium sized galaxy. 52

B.1 Performances of the sequential code 75

Notations

k_b	Boltzmann constant ($1.3806503 \times 10^{-23}$ $\mathrm{m^2\,kg\,s^{-2}\,K^{-1}}$)
ρ	density (in mass)
f'	differentiation of f
$\pm$	error on a given value, unless otherwise specified this is 1-σ error
h	Planck constant (6.626068×10^{-34} $\mathrm{m^2\,kg\,s^{-1}}$)
m_p	proton mass
R	radial coordinate in cylindrical system
r	radial coordinate in spherical system
$\mathrm{M}_\odot$	solar mass
μ	statistical mean (true or from a sample)
σ	statistical dispersion (true or from a sample)
σ^v	statistical dispersion around v, the mean of $(x-v)^2$ (true or from a sample)
Σ	surface density (in mass)

Table 1: Overview of the frequently used symbols. Unless otherwise noted, the symbols in this thesis have the meaning given here.

AGB	Asymptotic giant branch stars
CO	The molecular CO emission lines are tracer of molecular gas
`CP`	Cold phase
GMC	Giant molecular cloud
IMF	Initial mass function
ISM	Interstellar medium
LMC	Large Magellanic Cloud
MC	Molecular cloud
PAH	Polycyclic aromatic hydrocarbon
SED	Spectral emission distribution
SF	Star formation
SFH	Star formation history
SFR	Star formation rate
SMC	Small Magellanic Cloud
SPH	Smooth particle hydrodynamic
THINGS	The HI nearby galaxy survey (Walter et al. 2008)
`VP`	Variable (warm/hot) phase

Table 2: Overview of the acronyms.

Chapter 1

Introduction

1.1 Historical review

For a long time galaxies were thought to be "spiral nebulae", because of their unresolved nature with the available technology of the epoch. In the late 1910's a few clues arose to show the distant nature of these objects. They scientifically credited the idea first proposed by Kant of "island universe" in 1755. This led to the "Great Debate" in 1920. Although the debate opposing Curtis and Shapley originally focused on the true dimensions of the Galaxy, therefore the entire known universe, it includes the question of the nature of spiral nebulae. It is historically interesting as a debate opposing scientific points of view, arguing with poor, sometimes false, data, interpreting them in order to propose a model of the universe, partially closing some issues and opening others (Trimble 1995)[1]. Although the debate emphasizes, once again, the inconspicuous situation of the earth, it has little effect onto the public.

One century ago, in 1785, Herschel estimated the diameter of the Galactic disk is 1.8 kpc. He revised the value to 6.1 kpc in 1806 using the apparent magnitude distribution of stars and assuming a centered Sun. It is noteworthy that Cornelius Easton reported a spiral pattern in 1900; although the Sun is clearly not centered in the pattern, he continued to place it at the center of its map. Later the idea of the Sun far from the center arose. For instance Eddington (1912) moved the Sun 18.4 pc above the disk plane.

Shapley's main argument relied in his works on globular clusters and his estimation of their distance. It was right at moving the sun out of the center. However his model is a large Galaxy having a > 60 kpc diameter, with the sun at 20 kpc from the center. As a consequence of his finding he argued that spiral nebulae are part of the Galaxy, wrongly induced by van Maaner who erroneously claimed to find a rotation in spirals. Curtis studied these nebulae in depth. He was convinced they are outside the Galaxy and therefore estimated a smaller size for the Galaxy (10 kpc diameter) but was false at placing the Sun at the center of the Galaxy. Among numerous arguments a few are interesting in their own way.

Curtis argued about the high novae rate found in spirals supporting the idea of big stellar system. Shapley replied that novae cannot outshine the luminosity of an entire nebula. Indeed, SNe will be discovered later by Baade and Zwicky (1934).

Before the Hubble law, the high radial positive velocity of galaxies had been noticed and it remained unresolved until the expansion of the universe was proposed by the works of Einstein and Friedmann among others. Neither Curtis nor Shapley were successful in finding a satisfactory explanation.

[1] see also `http://apod.nasa.gov/diamond_jubilee/debate20.html`

On the other hand Shapley made a great use of the period–luminosity relation of cepheids, found in the LMC, and calibrated with statistical parallax. He reproduced the standard method for distance estimation in astrophysics, finding "standard candles" and calibrating them with accurate distance determination at smaller scale. Since the Great Debate, the cepheids method had proven its usefulness; Hubble first reported in 1924–1925 huge distances to NGC6822, M33, and M31, thanks to these peculiar stars, thus closing the debate. Cepheids are still used today for standard distance estimation in the local universe.

However the star counts used to derive the Galaxy scale length did not consider absorption by dust. Both sides wrongly agreed on this, especially Curtis thought dust is located only around the Galaxy since other galaxies show dust lanes around them. This lead to underestimation of scales; Kapteyn and van Rhijn provided the most accurate diameter of 17 kpc, and located the Sun at 3 kpc with star counting, without dust correction, reddenning and absorption. Dust corrections were included by Trumpler (1930). Dust also induced in error Shapley when he argued that surface brightnesses and color gradients are different in the Galaxy compared to spiral nebulae.

1.2 Dust

Dust effects on light were critical in the debate opposing Curtis and Shapley. Nowadays we begin to better know the properties of this component responsible for absorption, scattering, and infrared emission, well studied since the advance of modern space observatories. Although dust is negligible in mass, it is of primary importance to accurately know its effects on light in order to produce high quality astronomical data. Dust also receive attention to itself.

Interstellar extinction in UV has a bump located at 2,200 Å, explained with presence of grains by Seaton (1979). Savage & Mathis (1979) is an early review on properties of dust. Mathis et al. (1977) have studied extinction from ultraviolet to infrared to conclude on a power law for size distribution of grains. From these early works, a lot of progress have been done. Now dust is mostly studied from its infrared to submillimeter emission. Using observatories like Spitzer or Herschel, we are able to know emission from few μm to 500 μm adding also terrestrial 850 μm data, SCUBA for instance. Dust composition is also studied from meteoritic materials.

Three main problems still remain in debate.

1. Emission at various wavelength is fitted using SED models. The simplest one uses a modified blackbody (see Sect. 2.4.1). This allows to know mass and temperature of dust. However submillimeter data often show an excess according to the fit. This occurs in dwarf (Lisenfeld et al. 2002, Galliano et al. 2003, and Galliano et al. 2005), starburst (Zhukovska & Gail 2009), and interacting galaxies (Dumke et al. 2004 and Bendo et al. 2006). This excess could be interpreted as a very cold dust component – emitting at large wavelength –, therefore sometimes dramatically increasing dust mass. Reach et al. (1995) propose alternative explanations. Bot et al. (2010) check very cold dust, cosmic microwave background origin, varying spectral index, and spinning dust. They favour the two last for the Magellanic Clouds. Whether due to a cold component or other physical properties, we should be able to bring a new approach to this problem, by independently estimating dust mass from simulations of galaxies.

   Moreover, metal-rich galaxies display a linear relation between oxygen abundance and dust abundance. This shows that there is an approximately constant fraction of metal locked into dust, for any metal-rich galaxy. On contrary, in metal-poor galaxies, dust abundance is lower than their oxygen abundance allows. Moreover this is also the metal-poor, especially dwarf, galaxies which show submillimeter excess. Indeed, the cold component of dust is sometimes assumed to reproduce the constant fraction of oxygen locked into dust grains.

Then, a cold dust component explains either the apparently dust underabundance and submillimeter excess.

In this thesis, we will study the fraction of oxygen locked into grains as a function of metallicity. This should help to discriminate between existence of unseen cold dust component and real departure from the linear relation.

2. Moreover, Bertoldi et al. (2003a) and Bertoldi et al. (2003b) evaluated a dust mass of 7×10^8 $M_\odot$ in the quasar J1148+5251 at redshift 6.42 for H_2 mass of 2×10^{10} $M_\odot$. This indicates a dust-to-H_2 ratio of 3.5 %. This implies a high dust production rate in young universe. Indeed, AGB produces dust in a timescale of about 1 Gyr. Thus, SNII production is a preferred explanation for such high dust amount. However, SNII seem to be poor producers of dust in the local universe.

   In this thesis, we propose to study the early evolution of dust mass with various assumptions on production and destruction process of dust, in young universe.

3. Production and destruction mechanisms are also still poorly known in the local universe. SNe are thought to produce dust, although exact amount is uncertain. Cassiopeia A is a well studied core collapse supernova remnant where Dunne et al. (2003) have detected sufficient quantity of dust. However it is not clear if dust truly originates from SN or underlying ISM (see Dunne et al. 2009, and references therein) and effective dust enrichment into ISM is unknown because of destructive effects of a reverse shock (Barlow et al. 2010). On the other hand the relative amount of dust brought by grain growth through accretion of gas phase elements is still in debate. Draine (2009) argues a large fraction of dust is produced in ISM considering the time rates of destruction and dust from AGB. However Jones & Nuth (2011) have decreased the estimated efficiency of silicates destruction and review arguments against dust accretion.

   In this thesis, we will look at the effects of each processes by performing simulations of the same galaxy with various combinations of production and destruction processes in the local universe: production from AGB and/or SNe, destruction from SNe, and growth in ISM.

Recently, with the advance of modern observatories, resolution increases. This makes studies of dust distribution inside galaxies possible. Mattsson et al. (2012) and Mattsson & Andersen (2012) proposed a first attempt using analytical model to interpret gradients of dust-to-metal ratio. We hope our model using numerical simulations to be useful in order to study local dust abundance and gradients inside galaxies. Unlike semi-analytical models, our performed simulations are well designed to include dynamical effects. This therefore helps to find out mixing, migration, and/or ejection of dust possibly responsible of changes in the dust abundance distribution in galaxies.

We mainly aim to study correlation between oxygen abundance and dust-to-gas mass ratio for entire galaxies as well as galactic gradients. We allow (or not) for dust accretion and SNe production. Hence, this allows us to examine effects of these dust mechanisms in massive discs. We also perform simulations of low-metallicity dwarf galaxies to look at systematic variations of dust-to-oxygen ratio with metallicity, in order to bring constraints on the reliability of cold dust mass estimations.

Although Theis & Orlova (2004) had included dust in simulations to study the dynamical effects of dust as a cold component in gaseous ISM, we explore another way assuming dust has little effect on secular dynamical behaviour of galaxies. We include dust mass evolution model within self-consistent chemodynamical simulations. We exploit subgrid chemical model and

stellar population enrichment of our code. This allow us to design a local model which include the known production and destruction mechanisms. Moreover the delayed effects, specially stellar feedback and enrichment, are considered and properly included. Then secular evolution of both a massive disc and dwarf galaxies is simulated.

We have studied the three exposed problems. However our main goal is to show that simulations can be helpful in these three debates. That is why we have paid attention to mechanisms specific to simulations and their ability to describe both galactic chemistry and dynamic. Then, in addition to the results in these debates, we should be able to show that chemodynamical simulations are a powerful technic for additional studies of the dust mass and evolution.

Chapter 2

Galaxies and dust

2.1 Galaxies

2.1.1 Introduction

New: *Galaxies are gravitationally bound systems of dark matter and gas, with* $\sim 10^8$ *stars for dwarf galaxies, and up to* $\sim 10^{11}$ *stars for massive galaxies (Binney & Tremaine 1987; Binney & Merrifield 1998).* The latter form the most luminous component. **New:** *The stars are born in clusters by the collapse of molecular clouds (MC) in the interstellar medium (McKee & Ostriker 2007).* Stars evolve on a fixed path, depending on their initial mass and metallicity, in the well know Hertzprung-Russel diagram. The evolution of a stellar population, and subsequently the metal enrichment and the energetic feedback are fully determined by its initial metallicity. **New:** *The interstellar medium consists of gas in molecular, neutral, or ionized phase and includes a solid component known as dust (Tielens 2005).* The kinematics reveal the gravitational effects of dark matter.

2.1.2 Morphology

The well known Hubble classification makes use of morphological patterns, from elliptical, early-type galaxies to late-type galaxies. Elliptical galaxies have no or faded structures. They are classified into 7 classes, depending on the degree of ellipticity (earlier galaxies are perfectly round). After that, moving to late-type galaxies, two branches appear according to the presence or absence of a bar. Moving from early to late type, we firstly encounter lenticular galaxies. Their central region is similar to elliptical galaxies, but they have a large flat structure. Further down the sequence, spiral galaxies contains a bulge similar to an elliptic galaxy, and a full featured disk with spiral arms. Late spirals have no bulge, while early type ones have a prominent bulge.

Morphology is strongly affected by the environment as morphology–density (of galaxies) or morphology–radius (in clusters) relations show. Galaxies are believed to evolve from late-type to early-type, in the hierarchical scenario, through merging events and/or secular evolution.

2.1.3 Kinematics

New: *Spiral galaxies have a rotating stellar and gaseous disk component. For instance, the Sun has a typical circular speed of 220* $km\,s^{-1}$*. Near the center, the circular speed increases with radius. Then the rotation curve flattens at high radius. The highest speed is related to the luminosity of the spiral galaxy via the Tully-Fisher relation.*

New: *For elliptical galaxies as well as bulges of spiral galaxies, the kinematics are described by the dispersion velocity of stars, since there is no global motion of stars. Typical dispersions are about 100 km s^{-1}.*

2.1.4 Stars

It is generally assumed stars born with an universal IMF, then the number of stars of mass in $[m, m + \mathrm{d}m]$ is

$$\mathrm{d}n = m^{-\alpha}\mathrm{d}m, \tag{2.1}$$

found by Salpeter (1955).

Stars born mainly in clusters, from collapsing then fragmenting GMC. Initial stellar mass and metallicity fix evolution during the entire life of a star. Above 7–8 $M_\odot$ stars will become SNII (eg. core-collapse SN) after hundred of Myrs, and after few Myrs for the most massive stars.

2.1.5 The interstellar medium

Tielens (2005) is a review of chemistry and physic in ISM.

The distance between stars in Solar neighbour is about 1 pc. This space is filled by ISM, mainly gas, with dust as solid state. It is of primary importance for galactic evolution. Indeed, stars born in cloud of collapsing gas and ISM evolves with feedback and metal enrichment from stellar winds and SNe remnant. Many objects reveal the richness of ISM and emphasizes its morphological complexity and the numerous physical processes inside ISM.

Objects

HII regions, like M42, are nebulosity ionized by the intense radiation of early-type (OB) and young stars. Their temperature is about 10^4 K at density > 10 cm^{-3} and their size are about 1 pc. Warm dust, heated, emits inside these regions.

Reflection nebulae are gaseous clouds illuminated by radiation field of neighbour stars. However it is not sufficiently heated to be ionised and to emit themselves. Dust is also heated.

Dark clouds are dense regions where dust could absorbs up to > 10 mag. They have a size of $\lesssim 10$ pc. They usually emit in IR but some can be also dark at these wavelength.

Photodissociation regions are usually at the interface between molecular and ionized phases. Their molecules and atoms receive a sufficiently intense level of UV (or even far ultraviolet) to dissociate molecules and ionize them. They show also an IR continuum due to their dust.

SNe leave materials, ejected by these highly energetic events. With time the surrounding ISM is shocked and it therefore forms SN remnants. These remnants have hot gas at about $\sim 10^6$ K emitting X-rays and a synchrotron emission at radio wavelength.

Phases

ISM can be splitted in unmixed phases: cold neutral medium, warm atomic, either neutral or ionized, hot phase and MC.

Neutral medium is observed using 21 cm HI line and absorption of light passing through ISM from bright sources. Cold neutral medium has a temperature of ~ 100 K in diffuse clouds of ~ 10 pc diameter at density ~ 50 cm^{-3}. In the Galaxy, this phase is located in a thin disk having height of 100 pc. Intercloud medium is filled by a warm neutral phase at $\sim$ 8,000 K at $\sim$ 0,5 cm^{-3}. It is a little thicker with a scale height of 220 pc and an observable tail unlike gaussian distributions. Although clouds contain 80 % of mass in disk plane between 4 and 8 kpc

from center, these two phases, cold and warm neutral, have the same surface density on average. Warm ionized medium, also at $\sim$ 8,000 K, which is the transition temperature for ionisation of hydrogen, have a more extended altitude with scale height about 1 kpc, and a volume filling factor of 0.25. Hot ionised medium at 10^5–10^6 K replenishes the halo (scale height of 3 kpc). It is observed through continuum and lines in UV and X-ray wavelengths. It is also located in SN remnants. All these phases are generally assumed to be in pressure equilibrium.

On the contrary, MC are thought to be gravitationally bound. They are dense objects, > 200 cm^{-3} and cores in them can exceed 10^4 cm^{-3}, at very low temperature: 10 K. GMC span a large range of properties. However a typical GMC has a size of 40 pc, a lifetime of about 3×10^7 yr and a mass of 4×10^5 M$_\odot$. Although H_2 is the most abundant molecule in them, they are usually observed using CO (1-0) transition line at millimeter wavelength. MC form from HI filaments thanks to thermal/gravitational instabilities and/or shock compression (Fukui & Kawamura 2010). MC are therefore surrounded by HI envelope, and theoretical studies emphasizes on pressure and radiation field for HI conversion to H_2. HI filaments are themselves formed by supershells and from density waves in spiral galaxies. GMC mass distribution follows the law:

$$\frac{\mathrm{d}n}{\mathrm{d}m} \propto m^{-\alpha}, \tag{2.2}$$

with α from 1.55 ± 0.20 for M31 up to 2.49 ± 0.48 for M33 and above $\sim 10^5$ M$_\odot$.

Stellar feedback

ISM is heated by radiation. Submillimeter radiations of the cosmic microwave background, visible and NIR of cool stars are absorbed, specially by dust. Far ultraviolet radiations from early-type (OB) stars also heat ISM, at extreme ultra violet the lyman edge from H absorption causes an abrupt drop of radiation field. X-rays emission lines from hot plasma and SNR also help. Magnetic field is an important energy and pressure source, specially in MC. Cosmic rays which are relativistic particles (protons, He, electrons) are another source of energy in ISM. Although the mechanical energy released by stars is small ($\sim 0.5\%$), it has morphological consequences. Indeed, turbulent energy supports gas collapse in molecular clouds and shapes the density distribution of ISM.

New: *Galactic winds are likely to be induced by starbursts. Gas is ejected at a few tens of km s^{-1} up to 1,500 km s^{-1}, depending on temperature. Outflows are perpendicular to the disk plane. They form structures extending from 1 kpc to tens of kpc (Veilleux et al. 2005).*

Cooling

We have seen in the previous section that gas is heated. However ISM can reach low temperature as low as $\sim$ 10 K in MC providing evidence for efficient cooling processes.

Radiative cooling occurs through the transition of atomic and molecular states. For atoms, energy is released as photons by quantified jump of electrons of about eV. Spectroscopy reveals this by emission lines typically located at UV and visible wavelength. Molecules show also bands from MIR to millimeter in spectrum, due to their vibrational and rotational energy. For instance, the well used CO rotational lines at 2.6 mm is used to trace molecular gas.

For optically thin plasma with two level system approximation, if the density of medium is sufficient, collision dominates the de-excitation process of particles. Hence, medium reaches local thermodynamic equilibrium. HI hyperfine transitions, specially 21 cm line useful to trace neutral gas, are in such collisional equilibrium. Otherwise it is not the general case in ISM and photon emission occurs before collisions. Hydrogen is usually an important cooling element,

until temperature reaches $\sim 10^4$ K. Above, it is totally ionised and cooling mainly occurs through metals. Free-free radiation plays a role at about $\sim 10^7$ K.

Gaseous metallicity

López-Sánchez et al. (2012) review the state of the art technics to get metallicity in ISM and their respective reliability. All are based on emission lines of HII regions. Here we study only oxygen abundance, which is one of the more accessible. Oxygen is a product of the α-process sitting in short-lived stars and fortunately represents a fraction of ~ 50 % of the mass of heavy elements. It is therefore a good indicator of the overall metallicity of ISM.

Three technics to derive oxygen abundances are available.

1. Directly measured temperature of e^- is based on collisionally excited lines. It uses [OIII] line ratio λ4363 (an auroral weak line) to λ5007 (strong nebular line). Since intensity ratio is only few percent, spectra need a high signal-to-noise ratio. Moreover in heterogeneous HII regions (temperature gradients, shocks, dense inclusions), temperature can be overestimated. This leads to an underestimated abundance by an estimation of 0.2–0.3 dex.

2. Techniques based on recombination lines seem to be the most reliable, when comparing with neighbour stellar metallicity. However they are not used in papers referenced by this thesis.

3. Strong emission line method is suited to distant galaxies, where poor spectra are obtained and/or stellar continuum hides the weak lines used in other methods. The method makes use of an ionisation parameter. Referenced papers in this thesis use the ratio

$$R_{23} = \frac{[\mathrm{OII}]\lambda 3726.9 + [\mathrm{OIII}]\lambda 4959 + [\mathrm{OIII}]\lambda 5007}{[\mathrm{H}\beta]} \tag{2.3}$$

   which has the default to be 2-valued as a function of oxygen abundance. Two classes of method exist with strong emission line. The first uses empirical calibration from HII region where T_{e^-} is available, they seems to be in better agreement with recombination lines technic. The second takes advantage of photoionization model of HII regions to predicts oxygen abundance. The later seems to overestimate by 0.2–0.5 dex.

The scatter of the used methods is typically of ~ 0.1 dex.

2.2 The Milky Way

2.2.1 The stellar component

Milky Way, like typical spiral galaxies, has a thin and a thick disk component, a stellar halo including globular clusters, a bulge and a bar. With a mass of $\sim 2 \times 10^{11}$ $\mathrm{M}_\odot$, Milky Way is a massive disk galaxy.

Two scenarii exist for formation of the bar/bulge system of ~ 3.5 kpc: secular evolution, by growth of the instabilities of the disk, heating central part of the stellar disk, or the instabilities caused by a minor merger.

The rotating disk has an exponential scale length of $R_d = 3.5 \pm 0.5$ kpc (the solar system is located at 8.3 ± 0.4 kpc at rotating speed ~ 200 $\mathrm{km\,s^{-1}}$). It can be splitted into two components: one of typical scale height $h \sim 200$ pc, the thin disk, and the thick disk with a scale height

of $\sim$ 1 kpc, has a surface brightness $\sim$ 10 % of the thin disk one. The thick disk has an old stellar population ($>$ 10 Gyr), with metal poor ([Fe/H] $\in [-1, -0.5]$) stars and enhanced [α/Fe] ratio. It was formed by gas-rich merger with in-situ star formation, accretion of a stellar system, heating of the thin disk, or migration of stars to larger radius.

2.2.2 The gaseous component

Radial distribution of the gas shows a hole for $R \lesssim 4$ kpc, a molecular ring at 4.5 kpc and, for molecular gas, an exponential distribution with a scale length of $\sim$ 3 kpc. The scale height is 75 pc for molecular gas and 200 pc for the neutral one, decreasing to $<$ 100 pc near the nucleus. Total gas mass is 4.5×10^9 $M_\odot$ ($\sim$ 2 % of the stellar mass)

2.3 Dwarf galaxies

In order to describe properties of dwarf galaxies, I use two reviews, one from Mateo (1998) and the other from Tolstoy et al. (2009).

Although definition varies with authors, dwarf galaxies are considered as low-luminosity galaxies ($M_B \gtrsim -16$, $M_V \gtrsim -17$), more extended than globular clusters (half-light radius $r_{1/2} \geq 1.6$ pc) and having a dark halo. This definition has not a physical meaning because there is not a clear distinction with less massive disk systems. Dwarf galaxies are well studied in the Local Group (Milky Way and M31), where $\sim$40 galaxies of such type have been found, and other $\sim$ 20 galaxies are expected and not yet been found because of their low galactic latitude. Well known exemples are the Small and Large Magellanic Cloud (SMC and LMC), neighbours of our Galaxy at 58 and 49 kpc respectively. Dwarf galaxies of the Local Group extend to $1,600 \pm 200$ kpc (for IC5152), which is approximatively the size of the Local Group ($\sim$ 1.8 Mpc) when considering dynamical approach using zero velocity surface[1]. Dwarf galaxies are the most numerous galaxies and own a large fraction of a cluster mass.

Fig. 1 of Tolstoy et al. (2009) allows to distinguish different classes of objects. Note that M32 falls in the definition of dwarf galaxies but looks like a low-luminosity elliptical, indeed it is a compact galaxy. Dwarf spheroidal (dSph) are early-type galaxies and dwarf irregular (dIrr) are late type, while transition type are at an intermediate state. Blue compact disk (BCD), not observed in Local Group, are less extended and have a high SF. There are ultrafaint dwarf, which seems to be low-luminosity dSph, more metal poor, dark matter dominated, thus, probably not globular clusters but galaxies, with low surface brightness. We also observe ultra compact dwarf similar in size to globular clusters, observed in other galaxy clusters.

dIrr are optically dominated by star-forming regions and OB associations with clumpy morphology. Background of older stars emits a more extended, smooth, and symmetric component. DSph are smooth, few have nuclei and M32 is believed to have a black hole. Profiles are generally fitted with King model, preferentially for earlier type, or exponential model for late type. dSph appear as gas-free dIrr, due to SF and/or ram-pressure stripping, but discrepancies remain on central surface brightness or structures (Hunter & Gallagher 1985, Bothun et al. 1986, and James 1991). If a dwarf galaxy lives near a massive one, it can have tidal distortions: stars become unbounded to their galaxy. Then the host galaxy elongates and finally can disrupt the dwarf galaxy to form streams and partially populate the halo of the massive galaxy.

SFH of dwarf galaxies is derived from photometry, by using different classes of stars, each being witness for a typical age of SF: Wolf-Rayet for the past 10 Myr, Blue-loop stars for 100–

[1]Surface delimiting the volume where attraction of the Local Group balances the Hubble expansion field. Mateo (1998) exposes a refined method. He distinguishes galaxies bound to the Local Group or just travelling inside.

500 Myr, red supergiants for 10–500 Myr, AGB for ∼1 Gyr, RGB for $\gtrsim$ 1 Gyr, red-clump and horizontal branch stars for 1–10 Gyr and $\gtrsim$ 10 Gyr respectively, subgiant branch stars for $\gtrsim$2–4 Gyr, main sequence with the help of subgiant for $\gtrsim$1–2 Gyr with a good resolution (∼ 1 Gyr). SFH is also built by comparing synthetic color-magnitude diagram with observed one. This latter method is affected by age-metallicity degeneracy.

Dwarf galaxies have various moderate SF with short quiescent phases. Old population for dIrr are younger than 10 Gyr, recent SF display short bursts (10–500 Myr duration). Due to their gas-poor nature, dSph have not formed stars since at least 100 Myr ago. Transition type have HI gas but no SF. BCD display a recent and high SFR.

dIrr galaxies can have gas-to-total mass ratio from 7% to 50% while transition galaxies typically have 1–10% and spheroidals $\leq$ 0.1%. **New:** *Since we will study especially dust, we are interested in gas rich galaxies.* Although dIrr display HI clumps of 100–300 pc generally located near SF regions, HI emission is generally centered with optical emission and is more extended. Dust as well as CO clouds in dIrr have generally a size of 20–40 pc and a mass of few 100 $M_\odot$, near SF regions, dust is also found near the core of some dSph. HII regions $\lesssim$ 200–400 pc are detected in all dIrr, whereas no HII is detected in most galaxies of earlier types.

Chemical abundances are estimated from photometry or spectroscopy of RGB stars or emission lines in HII regions or planetary nebulae. For stellar component, [Fe/H] is underabundant (< -1 dex Tab. 6 of Mateo 1998) and has significant dispersion in a galaxy (from $\sim 0.3 \pm 0.1$ to $\sim 0.7 \pm 0.2$ dex). For HII regions, oxygen abundances is well studied, dispersion seems to be insignificant, implying an uniform abundance, thus a good mixing from gaseous hot phase. There is a bimodal correlation (Fig. 7 from Mateo 1998) between luminosity and metallicity, for dIrr on one side and dSph and transition type on other side. The bimodality is expected to be due to SF in dIrr.

From radial scale length and central surface brightness, velocity dispersions should be $\leq$ 2 km $\times$ s^{-1} while observations give $>$ 7 km $\times$ s^{-1}. Moreover, rotating galaxies have kinematic not consistent with mass derived from their luminosity. To be in equilibrium, dwarf galaxies must have an important mass of dark matter.

Oh et al. (2011) derive rotation curves as well as gaseous mass distribution of THINGS dwarf galaxies from HI data. They assume a stellar mass distribution from infrared and visible data. Then they compute dark matter profile and find it is better described by a core model. They therefore choose to use pseudo-isothermal halo model.

2.4 Dust

2.4.1 Effects on radiation

Although dust has little fraction of mass in ISM, it has strong effects on light. It absorbs and scatters light causing extinction, preferentially for shorter wavelengths called the reddening. The extinction of a distant background star is the difference in magnitude between light observed through dust and light which should be observed without dust, for a given waveband. Reddening, or color excess, is caused by stronger extinction at short wavelength. The ratio of extinction to reddening is therefore constant when grains properties are uniform, and amount is only determined by the column density of dust.

Energy captured from photons from UV to IR is emitted by NIR to submillimeter radiations, depending on the properties of grains. Small grains are not in thermal equilibrium and can emit in NIR/MIR, showing pronounced features like PAH. For longer wavelength grains responsible for emissions are in thermal equilibrium and approximately emit radiations with a blackbody

law modified by emissivity ϵ:

$$I_T(\lambda) = \epsilon(\lambda) \frac{2hc^2}{\lambda^5} \frac{1}{e^{\frac{hc}{\lambda k_b T}} - 1}, \tag{2.4}$$

$$\epsilon(\lambda) = \epsilon_0 \left(\frac{\lambda}{\lambda_0} \right)^{\beta}. \tag{2.5}$$

β usually spans from 1 to 2, and seems to be anti-correlated with the temperature of dust.

Spitzer and Herschel are powerful instruments to explore dust emission from near-infrared to far-infrared and obtain spectral energy distribution (SED). Submillimeter data allow to add constraints on SED fitting at longer wavelength. In addition to the previously described greybody model, more complete models have been designed over years (Li & Draine 2001, Zubko et al. 2004, Draine & Li 2007, Meny et al. 2007, Paradis et al. 2011, and Compiègne et al. 2011). They make use of Galactic observations to include a size distribution and a chemical composition of dust.

2.4.2 Composition

Although exact dust composition is still debated, dust compounds seem to form three main and distinct classes: silicates, carbon and iron.

In mass, ~ 0.5 of dust are silicates. Forsterite Mg_2SiO_4 and Fayalite Fe_2SiO_4 are components of olivines, enstatite $MgSiO_3$ and ferrosilite $FeSiO_3$ are pyroxenes. Silicates are a mixture of olivine and pyroxene. According to Zhukovska et al. (2008), silicates composition has been derived from local ISM using meteoritic materials, depletion, extinction curve, and infrared emission. They find Mg based compounds (forsterite and enstatite) are major components, up to 80 % of silicates, from constraints of silicate-to-carbon dust mass ratio. From ratio of Mg and Si locked into dust they deduce a fraction of olivine of 0.32 in diffuse phase. Dust mixture is therefore pyroxene rich.

Carbon dust is another major component, available, for instance, in form of silicon carbides SiC. However, in molecular clouds, available C is reduced by 20–40 % due to formation of molecular CO. This could reduce dust formation rate in ISM. PAH are big molecules, up to 10^3 C, contributing for few per cent of total dust mass.

Iron based dust is the last component, for remaining Fe not locked into silicates.

2.4.3 Box model

Semi-analytic chemical models use partial differential equations to compute time evolution of galaxies. They aim to reproduce the global evolution of gas and stellar mass or density and chemical abundances found for stars and/or in gas. Simple models are "closed box": matter does not infall nor outflow. Unfortunately, without infall, models are unable to reproduce the metallicity distribution of metal poor stars. This is the "G-dwarf" problem (van den Bergh 1962, Pagel 1997, and Cowley 1995). Thus, exponentially decreasing infall rate is added. For massive galaxies, outflows by galactic winds from SNe feedback are neglected while they are necessary for dwarf galaxies. Refinement is also possible using "one-zone" approximation. Evolution is therefore computed for a grid of radius for a disk galaxy and assuming no radial mixing nor migration. Then star formation rate is derived from the Schmidt law or the approximation proposed by Dopita & Ryder (1994).

Stellar enrichment is added usually with instantaneous recycling approximation: stars die immediately after they born. This is an useful approximation for core-collapse SNe with lifetime

$\lesssim$ 100 Myr. However, for SNIa and AGB, the last known as the major producer of stardust in the Milky Way (Zhukovska et al. 2008), the lifetime is about $\sim$ 1 Gyr, thus enrichment must be delayed.

To follow dust mass, models are designed for three main goals: study of dwarf galaxies with low-metallicity ISM, chemical study of massive galaxies similar to the Galaxy predicting elemental depletion, and to solve the problem of high dust mass found in young quasars at redshift $z > 6$.

They usually introduce dust injection by core-collapse SNe, SNIa, and AGB, destruction by shocks from SNe. To avoid high dust destruction rate, models usually add grain growth by accretion in MC.

Lisenfeld & Ferrara (1998) have designed a model of dust mass evolution in dwarf galaxies. Stars produce dust with instantaneous recycling approximation. A fraction of metal is therefore injected in form of grains into ISM. Various values of this fraction have been tested to fit observations. Grains are destroyed in shock induced by SNe. Gas is ejected with galactic outflows and the fraction of dust in these outflows is also a varying parameter. To check the model, Lisenfeld & Ferrara (1998) have used a sample of dIrr and BCD galaxies with oxygen abundance and dust mass fraction, expected to be related by a linear relation. They found that this relation is not compatible with data of dIrr, then explained the deviation with outflows.

Dwek (1998) was interested by the Galaxy. In his model, galaxy forms by infalling gas and a star formation following Dopita & Ryder (1994) law. Enrichment is delayed and dust is produced by SNII and less massive stars as well as SNIa. The model also includes destruction. Grains grow by accretion in dense ISM. Moreover, it is a multizone model, eg. evolution depends on radius. However he assumes that there is no radial motion and/or mixing of dust. Evolution of multiple dust species, carbon grains and other considered as "silicates", are followed. In this model C, O, Mg, Si, S, Ca, Ti, and Fe depletes and elemental depletion pattern is derived. Dwek (1998) found linear dependence of dust mass abundance with oxygen abundance using radial gradient. The model is also compatible with data from Lisenfeld & Ferrara (1998) if we allow an offset.

Zhukovska et al. (2008) is an update of the work of Dwek (1998). It includes a computed grid (mass, metallicity) of dust condensation from AGB stars, a more detailed growth recipe. The model adds SiC and iron grains and considers C, O, Mg, Si, and Fe can be locked into dust grains.

Dwek & Cherchneff (2011) design a model to explain the surprisingly high dust mass $\sim 4 \times 10^8$ $M_\odot$ observed in the quasar J1148+5251 at high redshift. They found that either SNe or AGB are able to produce such high quantity of dust with special SFH. Indeed, they reproduce the observed high amount of dust if an intense starburst, producing dust, is followed by a more quiet period, preserving dust from destruction. Their model includes infall and outflow, destruction, and delayed dust production.

The papers exposed here are a sample of numerous existing dust mass evolution model. For instance, we can also cite Edmunds (2001) who distinguishes a grain core and mantle growth in ISM. Hirashita (1999a,b,c) has adapted a model to dwarf and spiral galaxies and multiphase model. Gall et al. (2011a,b) was interested in production of dust at high redshift. Hirashita et al. (2002) have designed another model for BCD galaxies from Lisenfeld & Ferrara (1998). They found that dust-to-oxygen mass ratio varies quickly with the variation of destruction from SNII during one star formation episode at $12 + \log(\mathrm{O/H}) = 8$.

I have adapted their recipes to design my model, taking advantages of local description allowed by chemodynamical simulations. My main goal is to design an unique numerical model for dwarf, massive and young galaxies, while semi-analytic approach needs to adapt models to each study. I have included all of the common processes of semi-analytic models: production by AGB stars and SNe, destruction by shocks, accretion in ISM. However, since I include my

model in numerical simulation, outfall, enrichment from long-lived stars, star formations, are all provided by the simulation and do not need to be approximated and/or modeled.

2.4.4 Production and destruction

The model is fully exposed in Sect. 3.2. We present here an introduction of the processes included to compute the evolution of dust mass in simulations (see Fig. 2.1).

As we have seen in the previous section, three main production processes have to be included: production from AGB stars, from SNe, and growth in ISM. Destruction occurs through shocks produced by SNe. On contrary to the semi-analytic model, in order to design our model, we have paid attention to have local description of all phenomena thanks to numerical simulations.

AGB stars highly enrich the ISM. Indeed, when thermally pulsing, they produce winds sufficiently cold, where materials condense and form dust grains. SNe are also thought to produce dust. In sufficiently dense ISM like molecular clouds where grains are also protected from destructive radiation, growth of grains, by accreting atoms and molecules on surface, allows for dust production. Destruction of grains is theoretically known. The main process is the destruction through shocks. These shocks, produced by highly energetic events like exploding SNe, submit grains to sputtering (gas-grain interaction) process and grain-grain collisions. Finally, when stars form in cores of molecular clouds, dust is incorporated in forming stellar system and/or destroyed by the radiation of new stars. Thus, dust is likely to be destroyed with star formation. Since dust production in ISM depends on the density of gas, we expect variations of abundances according to the phases of ISM. Then, there is also dust transfers between these phases.

2.4.5 Observations

Dust and oxygen gradients

Magrini et al. (2011) use Herschel observations of four Sbc galaxies in Virgo cluster to reproduce dust map. With available HI and CO maps they are able to compare dust-to-gas mass ratio profiles with metallicity gradients. However, they derive dust-to-gas ratio from metallicity by using a constant fraction of metal abundance – approximated by oxygen abundance – locked into dust, and use this ratio as a witness to check various $X_{\rm CO}$ used to convert CO-maps to molecular density maps, thus to have dust-to-gas ratio maps from HI and infrared data. By comparing dust-to-gas ratio from metallicity with such ratio from infrared and H maps, they constrain $X_{\rm CO}$.

While Magrini et al. (2011) assume a relation between dust abundance and metallicity for radial gradients, others have checked this relation, assuming $X_{\rm CO}$. For instance, Bendo et al. (2010) find slope of dust-to-gas ratio is in agreement with oxygen gradient for NGC2403. Pohlen et al. (2010) use ratio of 500 μm flux to gas mass including molecular gas. They assume this ratio reflects dust-to-gas ratio and find it radially decreases for M99 and M100.

Muñoz-Mateos et al. (2009) derive dust-to-gas profiles of THINGS galaxies and compare with oxygen profiles. Contrary to Magrini et al. (2011), $X_{\rm CO}$ is fixed and they look for the relation between dust and oxygen abundance using their gradient. They find a negative slope for dust-to-gas ratio profile, steeper than the slope of metallicity profile.

These papers show there is a great interest in dust gradient, related to metallicity one. Mattsson et al. (2012) and Mattsson & Andersen (2012) have recently emphasizes that by designing a dust production and destruction model. This model depends on galactic radius such that they can derive theoretical gradients. Then they fit profiles from Muñoz-Mateos et al. (2009) and look for dust processing and history in ISM. Indeed, the involved processes shape dust-to-gas and dust-to-oxygen gradients.

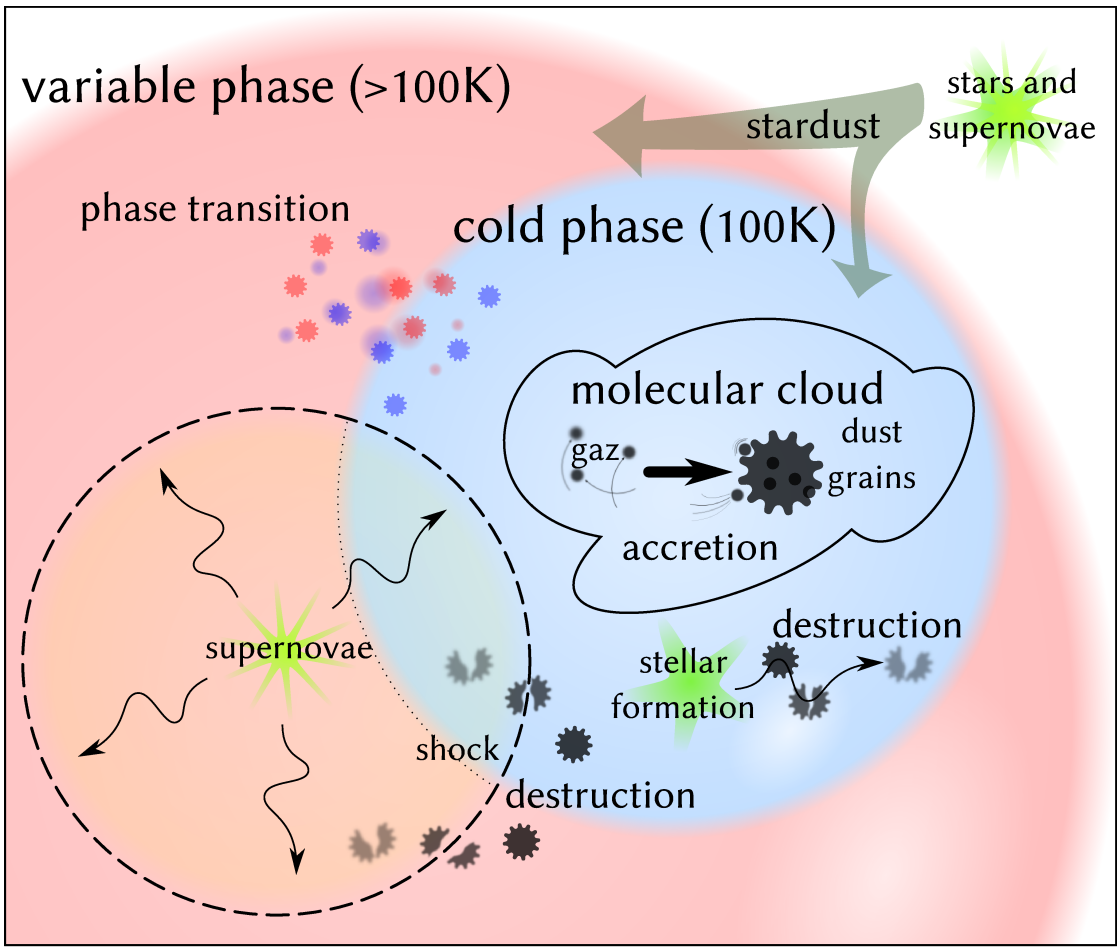

Figure 2.1: Sketch of the dust processes.

Dust is produced by SNII, few tens of Myrs after star formation, AGB stars, and growth in ISM, while it is destroyed by shocks mainly produced by SNII. Oxygen enrichment mainly occurs through SNII feedback. The difference of processes involved for dust and oxygen production – their time scale and dependences with star formation – implies differences on the shape of radial profile of dust-to-oxygen ratio and the slope of gradients. Reader should note here that behaviour of the two gradients relates to the relation between dust and oxygen abundances we will study.

Especially we expect SNII destruction and ISM growth make dust gradient different from oxygen gradient. This is the aim of Mattsson et al. (2012) and Mattsson & Andersen (2012). They find gradient sign provides an indication for dust history, thus dust processing. More precisely, they find more important dust accretion make dust-to-oxygen gradients negative and more important dust destruction make them positive.

Dust evolution

Bertoldi et al. (2003a,b) find a large amount of stardust for quasars at redshift 6.4. Although AGB stars are known to be major producers of dust in evolved galaxies, they need $\gtrsim 1$ Gyr time, assumed to be too long for these young objects. Many semi-analytical models try to address this issue. They can assume a higher SNe dust yield than observed in local universe (Dwek et al. 2007). Dwek & Cherchneff (2011) have done a study about the necessity of SNII production in early universe. They find that AGB are sufficient to produce high dust mass in quasars at high redshift, constraining SFH of such early objects. Pipino et al. (2011) and Valiante et al. (2011) add grain growth in interstellar medium (ISM). Gall et al. (2011a,b) emphasize effects of the choice of initial mass function. For a recent review see Gall et al. (2011c).

Dust–oxygen diagrams

For a first approximation one can assume that a constant fraction of heavy elements is locked in solid phase, giving rise to the proportionality:

$$\frac{\mathrm{M_{dust}}}{\mathrm{M_{gas+dust}}} = 0.01 \frac{(\mathrm{O/H})}{(\mathrm{O/H})_{\mathrm{MW}}}, \tag{2.6}$$

where the factor comes from local model of Draine et al. (2007) with (O/H) oxygen number or mass abundance.

For the need of our work we have used data from three papers.

Lisenfeld & Ferrara (1998) study dust-to-gas mass ratio of dwarf irregulars and blue compact disc galaxies, all have low metallicity. Oxygen abundances are taken from literature. To derive dust mass they fit a black body model to 60/100 μm flux. They consider errors from the contamination of very small grains in 60 μm radiation, cold dust possibly not detected in these short wavelengths, and finally errors from their estimation of H mass. They estimate the final error to be a factor of 4. They find a correlation for dwarf irregulars between oxygen abundance and dust-to-hydrogen mass ratio:

$$(O/H) \propto \left(\frac{\mathrm{M_{dust}}}{\mathrm{M_{HI}}}\right)^{0.52\pm0.25}. \tag{2.7}$$

The power is inconsistent with eq. (2.6). For BCD no clear correlation is found. Nevertheless, it may be only due to dispersion and a smaller range of available metallicities.

Draine et al. (2007) use physically motivated dust models (Li & Draine 2001 and Draine & Li 2007) for a subset of SINGS galaxies (Kennicutt et al. 2003). They check the error associated with cold dust to be less than 2.2 using SCUBA observations of 17 galaxies, they include PAH, and they use more data, having a spectral energy distribution with up to 7 bands from 3.6 to 160 μm. Oxygen abundances are taken from Moustakas et al. (2010), which provide measures using two calibrations. We choose the strong-line theoretical Kobulnicky & Kewley (2004) calibration. Their galaxies are more metallic than galaxies from Lisenfeld & Ferrara (1998).

Engelbracht et al. (2008) compute dust mass for a sample of starburst and star-forming galaxies observed up to the 160 μm wavelength, spanning a middle range of metallicities. To derive dust mass, they use emission model from Li & Draine (2001). In order to get oxygen abundances, they use electron temperature method for a majority of their galaxies, or a strong-line empirical method.

Each paper comes with a set of different galaxies, fortunately we can find a subset of galaxies common to two papers: 4 for Lisenfeld & Ferrara (1998) and Draine et al. (2007), and 10 for Lisenfeld & Ferrara (1998) and Engelbracht et al. (2008). To build up the diagram we define two offsets by paper, for both metallicity and dust mass ratio. The offset is the averaged difference (of dust or oxygen abundances) of the subsets of common galaxies (joined with a line in diagrams hereafter), the "error" of each offset is the unbiased standard deviation of the difference. These offsets are applied in the final diagrams to have consistent data. We must warn that the small size of each subset cannot allow for robust statistics, but we consider hereafter it is sufficiently indicative of errors, specially bias, coming from each sample.

Oxygen abundances for Engelbracht et al. (2008) and Lisenfeld & Ferrara (1998) are consistent (0.01 ± 0.11 offset). Data from Moustakas et al. (2010) (their theoretical "strong-line" R_{23}-based calibration from Kobulnicky & Kewley 2004) are 0.42 ± 0.14 dex above data from Lisenfeld & Ferrara (1998). This discrepancy is not surprising, Moustakas et al. (2010) themselves find a systematic over-abundance of 0.6 ± 0.06 dex when comparing with an empirical calibration (from Pilyugin & Thuan 2005). For more details about the $\sim$0.4–0.5 dex offset between theoretical "strong-line" and direct T_e method see Kewley & Ellison (2008) and references therein. Absolute reference for oxygen abundances (eg. null offset) is taken from Engelbracht et al. (2008) galaxies.

Lisenfeld & Ferrara (1998) underestimate by 0.68 ± 0.18 dex ($\times4.8$ factor) dust abundances according to Draine et al. (2007) values, a slightly higher value than their roughly estimated error "to be about a factor of 4". They also underestimate by 0.25 ± 0.43 dex dust abundances of data from Engelbracht et al. (2008). As Lisenfeld & Ferrara (1998) claim, despite high absolute error relative error is better constrained (0.43 dex $\sim \times2.7$ factor comparing with Engelbracht et al. 2008 down to 0.18 dex $\sim \times1.5$ factor with Draine et al. 2007). Finally, for dust mass ratio we use data from Draine et al. (2007) as absolute reference.

We use this bias-corrected dust versus oxygen abundances diagram as main diagnostic tool for our model. Observed galaxies are plotted on diagram (see Fig. 2.2) the grey line gives the maximum dust abundance in ISM as sum of C, O, Mg, Si, Fe mass in solar mixture, with a circle to locate solar metallicity (from Asplund et al. 2009). Then depending on real relative abundances (ie. the varying α/Fe) dust mass can exceed this indicative maximum.

Submillimeter excess is reported either in our galaxy (Reach et al. 1995) and local dwarf galaxies (Lisenfeld et al. 2002, Galliano et al. 2003, Galliano et al. 2005, Meixner et al. 2010, and Gordon et al. 2010). To take into account this excess, SED fits with modified black body model often include a very cold dust component at $\lesssim 10$ K (Galametz et al. 2009, O'Halloran et al. 2010, Planck Collaboration et al. 2011a, and Zhu et al. 2011). However the excess remains even with more complicated models. This leads to higher dust mass estimation than using only IR

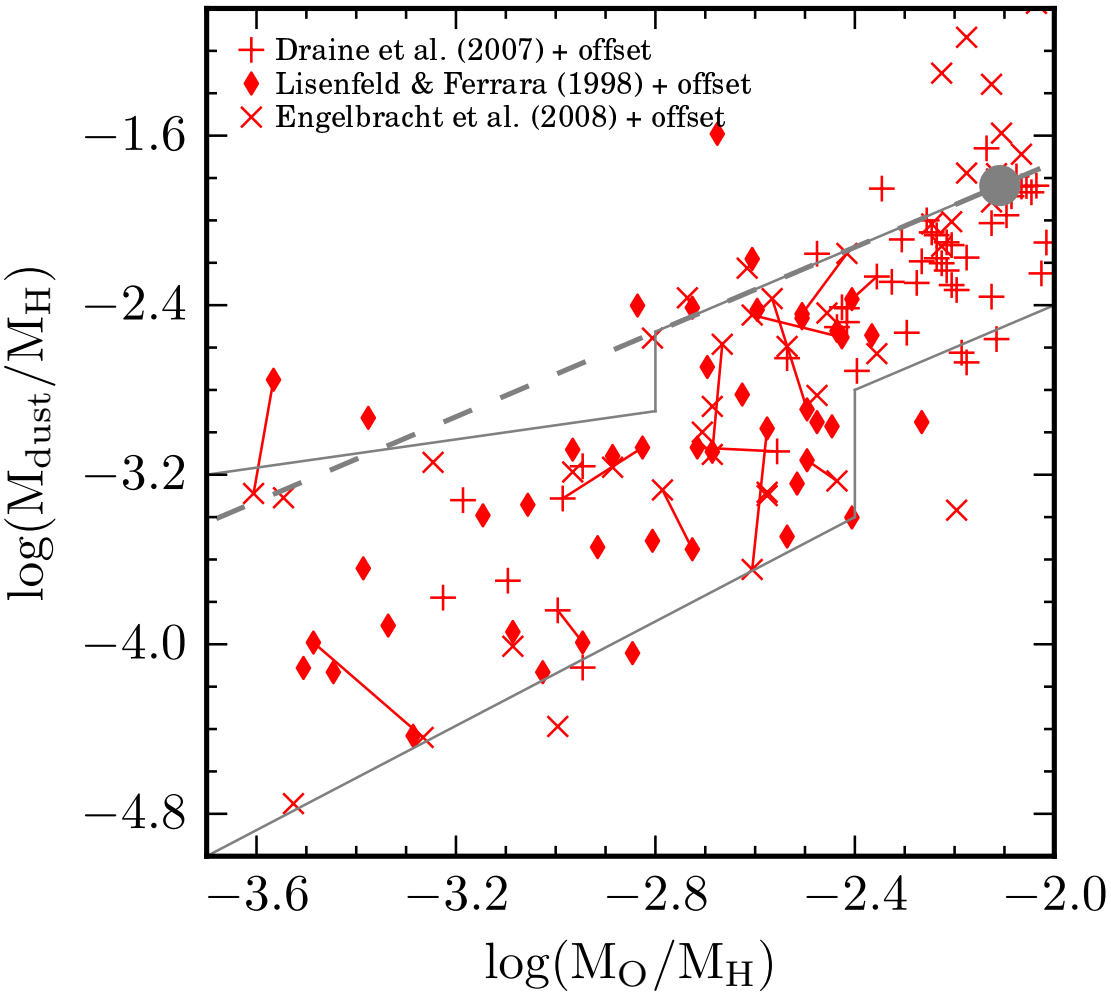

Figure 2.2: Dust–oxygen diagram with observed galaxies using offsets described in the text. The grey line is maximum dust abundance allowed for solar mixture of abundances. Plain circle locates solar metallicity.

data (Dunne et al. 2000, Dunne & Eales 2001, James et al. 2002, and Vlahakis et al. 2005, this is also true adding FIR to NIR observations: Popescu et al. 2002). Galametz et al. (2011) show the excess makes dust mass sensitive to the availability of submillimeter data. They find that induced error lowers estimated dust mass for metal rich galaxies. Indeed, few of such galaxies have much more dust abundance than allowed by their metallicity (above grey line in our diagram).

For few galaxies dust mass is over-estimated according to available metal. For II Zw 40 (from Lisenfeld & Ferrara 1998, diamond symbol), $M_{dust}/M_H = 10^{-1.59}$ is a maximum limit, not an estimation; Engelbracht et al. (2008) found $10^{-3.53}$ for this galaxy. Four galaxies of Engelbracht et al. (2008) are dust overabundant: Mrk 331, NGC 3079, NGC 5236, and NGC 5953; and they have dust-to-oxygen: 11.5, 8.3, 11.0, and 5.9 respectively, over the available metal/O ratio $\lesssim$2, even considering errors. Dust-to-gas ratio appears overestimated here. This can be due to an overestimation from observations: for NGC 5953, Galametz et al. (2011) found a dust-to-hydrogen ratio of $10^{-2.11}$, compatible with our oxygen abundance. Indeed they estimate a bigger H mass and a smaller dust mass thanks to available submillimeter data. Moreover, dust mass can appear overestimated because of an under-estimation of metallicity, our correcting offset could also be in fault, wrongly assuming a constant error on the entire range of metallicity.

Anyway, including submillimeter data flattens the slope in dust–metallicity diagrams. Similar conclusion can be drawn from Fig. 8 of Dale et al. (2012). If they exclude Herschell/SPIRE (250, 350, 500 μm) and use only Spitzer/PACS (70, 100, 160 μm) data, dust mass estimation decreases for metal-poor galaxies. They have also studied error on dust mass induced by the choice of SED model, either Draine & Li (2007) or modified black body law. The later underestimates dust mass by nearly 2. However, Draine et al. (2007) have included a submillimeter excess in their model, and have no submillimeter SCUBA observations for metal-poor dwarf galaxies. Moreover, this excess can be explained with many assumptions, sometimes preferred: varying spectral emission index β due to physical variation of the properties of grains, spinning dust emission, or cosmic microwave background (Reach et al. 1995 and Paradis et al. 2012 for the Galaxy, Dumke et al. 2004 and Bendo et al. 2006 for NGC4631, with insight into the Magellanic Clouds by Israel et al. 2010, Bot et al. 2010, Planck Collaboration et al. 2011b, and Galliano et al. 2011).

Although we have corrected for error bias our dust–oxygen diagram, a peculiar problem remains in estimating dust mass, specially for dwarf galaxies. It appears that reliability of our diagram is highly dependent on used calibration for oxygen abundances and model to compute dust mass, specially allowing or not for cold dust with the availability of submillimeter data. In all case, we have assumed there is no cold dust mass associated with the submillimeter excess when we have built our dust–oxygen diagram for observations. Especially this excess does not depend on metallicity, it does not increase with decreasing oxygen abundance as it could be assumed. Despite the error induced in our diagram we will take a somewhat speculative view. We hope our effort to correct all bias to the dataset allows for our optimistic interpretations of observations, but readers must remember data are indicative and can be interpreted in very different manners. Our hope here is to bring them a new view on this diagram with simulations. We consider that observations are reliable within a 0.5 dex = $\times$3.2 factor error, likely to be correlated with metallicity in favour to a flattening of the distribution of galaxies on the diagram.

Chapter 3

Chemodynamical Code

3.1 Overview

Current hydrodynamical galaxy evolution codes typically follow the evolution of both the stars and the interstellar medium of a galaxy. Chemodynamical evolution codes also follow the evolution of both the stars and the ISM of a galaxy, with exchange terms that allow for the birth of new stars and for the thermodynamical feedback of dying stars. These codes often account for the chemical nature of the components: nucleosynthesis products of generations of stars modify the composition of the ISM and the composition of the stellar populations themselves. The chemodynamical code I have used as a starting point for this work is described in detail in the thesis of Champavert (2007). I summarize the main ingredients in this subsection. My work was to design and implement a model for the production and destruction of dust in the ISM. That model is described in subsection 3.2.

The chemodynamical code has to simulate the basic features of a galaxy, including gravitational dynamics for stars and the ISM, and hydrodynamical forces on the diluted components. The stars are modeled as a collisionless system. Both stars and gas are treated with an N-body code. At each step, the gravitational potential is computed using a particle-mesh algorithm. In that process, the mass of each particle is distributed by linear interpolation onto a grid. This cloud-in-cell method allows to obtain the density field of the simulation. One can show that the potential field is the convolution of a constant function with this density field. This allows to use Fast Fourier Transform to reduce computation time. The gravitational forces applied to each particle are computed by linearly interpolating the grid. The code uses a polar grid with increasing resolution towards small radii and regular subdivisions for azimuth and altitude. Since the grid is not cartesian, self-force appears and must be corrected. At large distances from the galaxy center, the potential is approximated by using a central point mass. The ISM is treated as a fluid. Smooth Particle Hydrodynamics (SPH) are used to solve the Navier-Stokes equation (the algorithms are adapted from Friedli & Benz 1993). This lagrangian method uses particles, simplifying N-body calculations. Hydrodynamic fields are approximated by smooth fields thanks to the kernel W of size h. This kernel tends to be a Dirac function when h tends to zero. A field f can be computed through a summation over particles p:

$$f(\vec{r}) = \sum_p \frac{m_p}{\rho_p} f_p W_h(|\vec{r} - \vec{r}_p|), \tag{3.1}$$

with ρ_p the density, and m_p the mass of particles. The code uses the smooth and finite kernel:

$$W_h(r) = \begin{cases} 1 - \frac{3}{2}\left(\frac{r}{h}\right)^2 + \frac{3}{4}\left(\frac{r}{h}\right)^3 & \frac{r}{h} \leq 1 \\ \frac{1}{4}\left(2 - \frac{r}{h}\right)^3 & 1 \leq \frac{r}{h} \leq 2 \\ 0 & 2 \leq \frac{r}{h}, \end{cases} \tag{3.2}$$

with variable h computed to keep the number of neighbours, thus $\rho_p h_p^3$, approximately constant. From standard hydrodynamical equation, one can derive SPH equation. The method naturally respects the conservation of mass. However, to close the hydrodynamical system of equations, we use the ideal gas law

$$P = (\gamma - 1)\rho u \tag{3.3}$$

with $\gamma = 5/3$ the adiabatic index.

Two phases have been implemented. They are fully mixed and kinematically coupled. Thus, SPH particles have two phases in equilibrium pressure. The cold phase `CP` has a fixed specific energy. For a primordial gas, this energy gives a temperature $T = 100$ K to gas. The variable phase `VP` has a variable temperature, above 100 K. The variable phase can be heated by stellar feedback and hydrodynamical equations and can cool. Finally the code computes chemical abundance for 9 elements: H, He, C, N, O, Mg, Si, S, Fe.

Our scheme of integration is a Runge-Kutta of order 2, with adaptive time step.

3.1.1 Interaction of gas and stars

Feedback from stars

New: *Stellar particles created during the simulation* use a model of single stellar population with a birthdate, a mass, and a metallicity. The IMF of such population follows a power law inspired by Kroupa (2001):

$$\mathrm{d}n = m^{-\alpha}\mathrm{d}m, \tag{3.4}$$

with the values actually used in the code (Champavert 2007):

$$\alpha = \begin{cases} 1.3 & m \in [0.1, 0.5]\,\mathrm{M}_\odot, \\ 2.3 & m \in [0.5, 100]\,\mathrm{M}_\odot. \end{cases} \tag{3.5}$$

Stars evolve, eject energy into ISM, and enrich gas, using a delayed model and interpolating from a grid of age and metallicity. The grid was computed from Starburst99 and Kobayashi et al. (2000) for SNIa.

New: *The injected energy heats the variable phase. The evolution of a stellar particle allows to heat and enrich gaseous particles at a distance smaller than their size h. For feedback provided by SNe, the code computes the radius of the remnant using a model of the propagation of shocks from Thornton et al. (1998).*

New: *We have not explicitly included winds, outflows and/or inflows in our code. In our study we will see that powerful galactic flows are detected. However they are a consequence of the local heating followed by a conversion of the thermal energy into momentum through the standard hydrodynamical equations.*

Star formation

New: *Simulations starts with a formed stellar component. This component does not evolve, produce metals nor heat the ISM. However stars are formed during the simulation. A stellar particle is created if a gaseous particle meets a few conditions, taken from the theory of star formation.* There are four criteria:

- Temperature $T < T_{\rm crit} = 10^4$ K
- Mass fraction of the cold phase $X_c > 0$
- Mass of gaseous particle $M < M_j = \frac{\pi\rho}{6}\left(\frac{\pi v_s^2}{G\rho}\right)^{3/2}$, with v_s the sound speed
- small free-fall time $t_{ff} = \sqrt{\frac{3\pi}{32G\rho}} \lesssim 10$ Myr, implying a density criterion $\rho > 0.65\ \mathrm{M_\odot\,pc^{-3}}$

Gaseous particles form stellar particles at same location and velocity and mass

$$M_g = n_{\rm frag}\mathrm{SFR}_{\rm cluster}t_{\rm SF} \tag{3.6}$$

with $\mathrm{SFR}_{\rm cluster} = 10^{-3}\ \mathrm{M_\odot\,yr^{-1}}$ the rate of stellar formation, $n_{\rm frag} = \lceil M/M_j \rceil$ the number of collapsing fragments, $t_{\rm SF} = \max(5t_{ff}, 10^6\ \mathrm{yr})$ the time to form the stellar particle.

Mass exchange between phases

Condensation and evaporation exchange gas mass between the cold and the variable phase. The formulae are the result of a model from Cowie et al. (1981). **New:** *The model computes the thermal evaporative mass loss rate from an idealized situation. It uses a multiphase approach with thermal conduction between dense, cold clouds, and ISM filled with low density and hot gas. Since our model is similar, we take the numerical equation from Cowie et al. (1981).* Therefore, the variation of the mass of the variable phase M_v is:

$$\frac{\mathrm{d}M_v}{\mathrm{d}t} = \begin{cases} 3.75\times10^4 T_v^{5/2}\left(\frac{r_c}{\mathrm{pc}}\right)\sigma_0^{-5/8} & \mathrm{g\,s^{-1}} & 1 < \sigma_0 \\ 2.75\times10^4 T_v^{5/2}\left(\frac{r_c}{\mathrm{pc}}\right) & \mathrm{g\,s^{-1}} & 0.03 < \sigma_0 \le 1 \\ -8.25\times10^2 T_v^{5/2}\left(\frac{r_c}{\mathrm{pc}}\right)\sigma_0^{-1} & \mathrm{g\,s^{-1}} & \sigma_0 \le 0.03, \end{cases} \tag{3.7}$$

using

$$\sigma_0 = \frac{T}{1.54\times10^7\ \mathrm{K}}\left(\frac{n}{\mathrm{cm^{-3}}}\frac{r_c}{\mathrm{pc}}\right)^{-1} \tag{3.8}$$

with $r_c = h f_c^{1/3}$ the radius of the cold phase, $f_c = V_c/V = X_c u_c/u$ being the filing factor and n the atomic density.

Cooling

Gas cools by emitting radiation. Cooling rate is computed from calculations of the photoionization code Mappings III, assuming optically thin gas in collisional equilibrium, with temperature T from 10^2 to 10^9 K. The code approximates the rate by linearly combining cooling rate of each chemical element at solar abundance and interpolating He rate from a grid (Champavert & Wozniak 2007).

3.2 Dust Mass Evolution

3.2.1 The model

We present hereafter the model used to compute mass locally **New:** *(eg. for each particle in the simulation)* locked in dust, separately for both phases of our ISM model. We assume dust is uniformly distributed in each phase and is exchanged with gas when the cold phase (`CP`) evaporates and the variable phase (`VP`) condenses. Moreover, dust is dynamically coupled with gas. **New:** *Thus, each gaseous particle has a dust abundance.* This assumption is supported by the fact that dust mass is nearly proportional to oxygen mass (see eq. 2.6) and that dust in HI-deficient galaxies is well stripped (see Cortese et al. 2010, and references therein).

We produce the so-called stardust from SNe and AGB stars which eject dust into ISM where grains grow by accretion. Finally destruction mainly occurs in shocks produced by SNe.

3.2.2 Production

Stardust is injected into each phase of ISM separately, in proportion of the volume filling factor of the phases. Piovan et al. (2011a) reviews adopted values in literature and references for production by stars. For AGB they cite Dwek (1998) and Ferrarotti & Gail (2006) who review all possible stellar sources of dust, updated by Zhukovska et al. (2008). For SNe they refer to Dwek (1998) revised in Pipino et al. (2011), Todini & Ferrara (2001), Nozawa et al. (2003, 2006, 2007), Bianchi & Schneider (2007), Dwek & Cherchneff (2011). For accretion in ISM we use a specific condition to activate the process in the cold phase of a SPH particle.

By Asymptotic Giant Branch stars

AGB stars are expected to be the main stellar source of dust in their Thermally Pulsing AGB (TPAGB) phase (Gehrz 1989, Morgan & Edmunds 2003, and Ferrarotti & Gail 2006). They take up to many Gyrs to return dust to ISM, unlike SNe.

In simulations, each particle represents a stellar population with a slope $\alpha = -2.3$ for initial mass function (IMF) at stellar mass above 0.5 $M_\odot$. In this stellar population, $M_\mathrm{m}(t)$ is the minimal mass of stars in the TPAGB phase at time t after the birth ($M_\mathrm{m}(t) \in [1, 7]$ $M_\odot$). Consequently all stars having a mass between $M_\mathrm{m}(t)$ and 7 $M_\odot$ have finished their TPAGB phase, and they have ejected all the associated dust. We therefore have to integrate dust ejected by stars which have masses from $M_m(t)$ to 7 $M_\odot$ to get dust produced by the entire population. TPAGB phase has lifetime from $\sim 10^5$ to $\sim 2 \times 10^6$ yr depending on initial mass and metallicity of stars, whereas mass lost duration is much shorter since it occurs at nearly end of the phase, only for few last pulses during $\lesssim 10^5$ yr (Vassiliadis & Wood 1993, Willson 2000, Morgan & Edmunds 2003, and Otsuka et al. 2011, see also Fig. 9 in Ferrarotti & Gail 2006). Then, we assume here that the TPAGB phase is instantaneous and we take its end as time release of dust condensated around a star. Note that ejecting dust 10^5 yr earlier changes dust production of the population by less than $\sim$10% the few Myrs after the most massive stars have begun the AGB phase, and less than $\sim$0.5% the rest of the time, which supports the previous approximation of the instantaneous AGB phase. Zhukovska et al. (2008) gives the grid of dust production (enhanced model of Ferrarotti & Gail 2006) and Girardi et al. (2000) gives the grid of $M_\mathrm{m}(t)$. The two grids are both linearly interpolated:

$$P_i(M, Z) = a_i(Z)M + b_i(Z), \tag{3.9}$$

$$M_j(t) = c_j t + d_j, \tag{3.10}$$

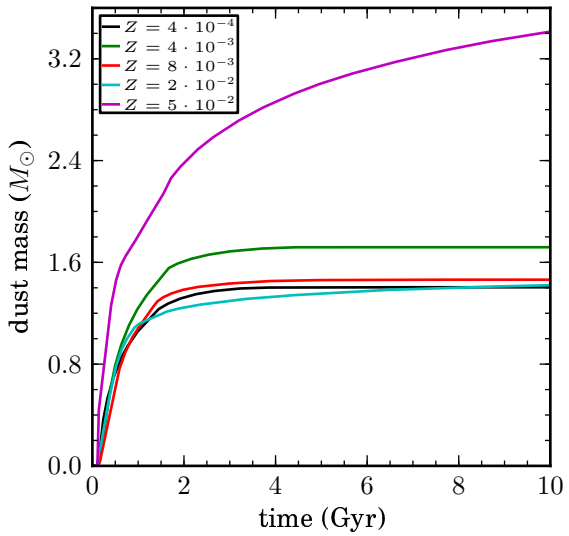

Figure 3.1: Dust returned into ISM by stellar populations of 1000 $M_\odot$ with different metallicities Z, computed from a grid of stellar mass and metallicities. We use these values as input for simulations.

respectively. Dust production for a 1 $M_\odot$ stellar population is:

$$P(Z,t) = \frac{1}{\int M f(M) \mathrm{d}M} \tag{3.11}$$

$$\times \int_{M_\mathrm{m}(t)}^{7\,M_\odot} P(M,Z) f(M) \mathrm{d}M. \tag{3.12}$$

splitted to have sums of integrals of power of M for each interpolated segment (i and j). Then, we can obtain totally analytic, and simple, sum of integrals to compute our input grid of metallicities and times (see Fig. 3.1).

By Supernovae

SNe are expected to be a dust progenitor in order to explain the high abundance of dust found in high-z universe (Morgan & Edmunds 2003, Kozasa et al. 2009, and Cherchneff & Dwek 2010), the extinction curve of quasars (Maiolino et al. 2004), the properties of gamma-ray burst afterglow (Perley et al. 2010) and particular composition found in presolar meteorites and interplanetary grains (Clayton & Nittler 2004). But little is know about quantities produced and survival of dust in ejecta returned to ISM (Nozawa et al. 2007 and Dunne et al. 2009). Recently Perley et al. (2010), confirmed by Jang et al. (2011), have found a significant dust column without trace of destruction, using the dust SED+extinction model of Maiolino et al. (2004). For SNIa Gomez et al. (2012) have not found evidence of stardust even if the theoretical work from Nozawa et al. (2011) predicts it.

To determine the quantity of dust returned we assume a constant fraction δ_{II} of ejected metal from SNII locked in dust. We use the value $\delta_{II} = 0.22$ derived by Morgan & Edmunds (2003) for solar metallicity (from theoretical model of Woosley & Weaver (1995)). Indeed, their table 2 shows that above $Z = 10^{-4}$, the δ_{II} fraction is approximately constant. For SNIa we take a

constant fraction $\delta_{Ia} = 5\times10^{-3}$ of ejected iron only, following Zhukovska et al. (2008). We have done a simulation without production by SNe for comparison.

While our chemodynamical code takes 8 $M_\odot$ for the lower mass limit of SNe, Zhukovska et al. (2008) use 7 $M_\odot$ for the upper mass limit of AGB stars. Stars with initial mass in $[7, 8]$ $M_\odot$ are therefore unproductive in dust. Considering these stars are SNe, this actually lower δ_{II} given in the previous paragraph. However SNe with initial mass in $[7, 8]$ $M_\odot$ account for 7% of total SNe mass in $[7, 100]$ $M_\odot$ with our IMF. If we assume metal enrichment fraction from this population is similar to its mass fraction, the true δ_{II} is therefore likely to be lowered by $\lesssim 10\%$ from the value given in the previous paragraph.

3.2.3 Accretion

Accretion is suspected to be an important process for dust production, needed to have a dust mass budget consistent with high depletion level contradicting high theoretical dust destruction in SNe shocks (McKee 1989 and Tielens 1998). Draine (2009) claim that stardust could account for only 4% of observed dust, comparing the time rate of the involved processes. Moreover there is a correlation between density of gas and depletion (see Jenkins 2009, and references therein), and accretion is a good candidate to fit observations. Indeed, accretion is more effective in dense gas, due to higher grain–gas collisions supporting growth process of grains. Moreover, dense (molecular) gas, providing a shield, prevents dust destruction from starlight. Note that stardust is always necessary as progenitors. As example Edmunds (2001) explicitly form core grains with stars and use mantle growth in ISM. In our model, accretion will implicitly needs pre-existing grains.

Our model accretes all elements that highly deplete and that have significant mass fraction in ISM, from Savage & Sembach (1996) and Pipino et al. (2011) we take C, O, Mg, Si, Fe as the main atomic components of dust. Calura et al. (2008), Piovan et al. (2011a), Piovan et al. (2011b), and Piovan et al. (2011c) add S and Ca to the previous elements in their model but we assume that their mass fraction is negligible in solid phase, because of their low gas-phase abundance (Asplund et al. 2009) and/or their low depletion (Savage & Sembach 1996). Other elements can deplete but they have also negligible mass fraction.

For a given specie A, the number density of particules incorporated in the grains with radius a is $n_{d,A}(a)$ and obeys the relation:

$$\frac{\mathrm{d}n_{d,A}}{\mathrm{d}t} = \alpha_A \pi a^2 n_{g,A} n_d(a) v_{th}, \tag{3.13}$$

where α_A is the sticking coefficient, $n_{g,A}$ is the number density of specie A in gas, $n_d(a)$ is the number density of dust grains, and

$$v_{th} = \sqrt{\frac{8kT}{\pi\mu_A}} \tag{3.14}$$

the thermal velocity – μ_A is the mass of the atom A relative to hydrogen. We want to integrate over the radius of grains to get a set of partial differential equation for each specie A. Thus, we define the distribution of grains by:

$$\mathrm{d}n(a) \propto a^{-\beta}\mathrm{d}a, \tag{3.15}$$

with parameters given table 3.1. We do not include PAH since they have negligible contribution to total dust mass, Draine et al. (2007) actually found PAH mass fraction $< 5\%$.

We assume here the grain size distribution does not evolve, this is a strong assumption since this implies that grains reprocess in ISM to keep the distribution constant by shattering from

Table 3.1: Chosen parameters for the distribution of grains: β is the exponent in the formula (3.15) giving the distribution between a_{min} and a_{max} from Desert et al. (1990).

type	β	$a_{\min}$ (nm)	$a_{\max}$ (nm)	ρ_{gr} ($\mathrm{g\,cm^{-3}}$)
small grains	2.6	1.2	15.	2.3
big grains	2.9	15.	110.	3.0

grain–grain collisions, while accretion and coagulation increase grain size and change the size distribution, affecting the growth rate in return (see Hirashita & Kuo 2011 and Hirashita 2012).

In their semi-analytic model, Zhukovska et al. (2008) choose to accrete "key" species which have the lowest growth rate. Indeed, they assume "key" species govern the global accretion rate of chemical compounds and limit the accretion of others species. But Jenkins (2009) found that each specie can accrete onto grains without – or with little – apparent effects from depletion level of other species. This is especially true for oxygen, depleting at higher level than standard oxygen-rich compounds allow (see discussion in the previously cited paper), while Zhukovska et al. (2008) did not include oxygen-rich compounds nor oxygen as "key" specie. This might induces a lowered oxygen depletion and accretion rate. Whatever the underlying nature of compounds to allow oxygen-rich dust, we assume here that oxygen, as well as the other accreting species, can deplete independently.

Moreover, we need to assume that mixture in dust is the same than in the gas. Jenkins (2009) notes that each individual atomic depletion have a linear relation to another – in logarithmic space – along a line-of-sight. Then he defines a generalized depletion factor. Then, each atomic depletion relates to this factor, depending on the line of sight and correlated to the averaged hydrogen column density. We can therefore use an unique, global, depletion factor (or dust locked fraction) without the need to follow each atomic specie. However each specie accrete on its own rate falsifying our assumption, but we expect the final result to be a good approximation considering global depletion factor.

We do not consider gas-phase CO molecules. Hence, we may overestimate dust mass (when accreting) by $\lesssim 20\%$ ($\sim$0.1 dex), taking solar mixture and assuming that CO can account for up to 40% of C and 20% of O (van Dishoeck & Blake 1998). Although this is clearly significant, considering dust mass and/or dust-to-gas ratio error from observations and range involved, this can be neglected. For the more critical dust-to-oxygen ratio, one can correct it by assuming a constant correction factor $\times 0.8$ when accretion is activated. The gas-phase CO obviously change accretion rate, however, this cannot be included as long as accretion mechanisms and CO formation in ISM are poorly known.

Finally all partial differential equations can be resumed by this one:

$$\frac{\mathrm{d}\rho_d}{\mathrm{d}t} = \tau^{-1}\rho_d\left(1 - \frac{\rho_d}{\rho_M}\right) \tag{3.16}$$

where the maximum accreting density is

$$\rho_M = \sum_A Y_A, \tag{3.17}$$

with Y_A the abundance in mass of the atom A. The accretion rate is

$$\tau^{-1} = 3\sqrt{\frac{kT}{2\pi}}\frac{<a^2>}{<a^3>}\frac{\rho_t}{\rho_{gr}}\sum_A \frac{\alpha_A}{\sqrt{\mu_A}}Y_A, \tag{3.18}$$

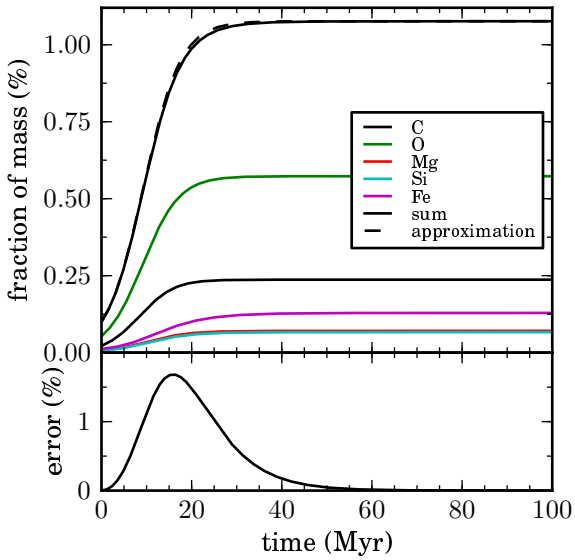

Figure 3.2: Accretion in a cloud with a density $\rho = 300$ cm^{-3}, resolving the partial differential equations and using our approximation. We use abundances of Asplund et al. (2009), eg. for C, O, Mg, Si, and Fe, in mass, 2.37×10^{-3}, 5.73×10^{-3}, 7.08×10^{-4}, 6.65×10^{-4}, 1.29×10^{-3} respectively. For the approximate formula (3.20) we found $\tau = 4.1$ Myr. Initial condition set a locked mass in dust of 0.1% for each element.

with $< a^n >$ the average of a^n over all radius a, according to the distribution given by the formula (3.15), ρ_t is the density in ISM (gaz and dust), $\rho_{gr} = 3$ g cm^{-3} the density of a dust grain (table 3.1). This is the current formula used in my model. However, a more convenient formula, for the reader, computed with solar abundance, is the accretion time:

$$\tau = \frac{12.3 \text{ Myr}}{\rho_t / 100 \text{ cm}^{-3}}. \tag{3.19}$$

The solution, and actually implemented formula, which will compute dust mass produced during a time step t is:

$$\rho_d(t) = \frac{\rho_d(0)}{\left(1 - \frac{\rho_d(0)}{\rho_M}\right) e^{-t/\tau} + \frac{\rho_d(0)}{\rho_M}} \tag{3.20}$$

We have done the exact resolution of the full partial differential equations set and compare it to our approximate solution (see Fig. 3.2).

We choose to apply accretion only in the SPH particle which can be considered as part of MC. In the presented simulations we apply accretion in the cold phase with a density superior to a threshold cold density $\rho_{\rm mc} = 10^3$ cm^{-3} or 10^4 cm^{-4} if it is explicitly stated.

New: *Our simulations (see chapters 4 and 5 for a complete description) have two kinds of initial conditions. We perform runs for one model of a massive galaxy similar to our Galaxy (simulations labelled* `low_res`*,* `full_3`*, and* `full_4`*). Their gaseous mass is 5 % of stellar mass.* `low_res` *is an early try to check our model at low resolution (5,000 gaseous particles, 100,000 stellar particles, 2×10^6 M$_\odot$/particle) while* `full_3` *and* `full_4` *have a higher resolution (50,000 gaseous particles, 1,000,000 stellar particles, 2×10^5 M$_\odot$/particle), using a density threshold of 10^3 and 10^4 cm^{-3} respectively. All these three simulations use the complete dust model (we will introduce later, in chapter 4, simulations switching off a few parts of the model). The second*

simulation	*power law index* α	*mass range*	($M_\odot$)
caaa	1.01	4×10^1	10^3
caab	1.10	2×10^0	4×10^1
caac	1.63	10^0	10^1
caad	1.52	10^0	4×10^2
caae	1.82	2×10^0	10^2
caaf	1.15	2×10^1	10^3

Table 3.2: Power law index of MC mass distribution and mass range where maximum likelihood analysis has been done. See the chapter 5 for description of the simulations of dwarf galaxies.

kind of simulation is designed for dwarf galaxies (simulations labelled caaa*,* caab*,* caac*,* caad*,* caae*, and* caaf*). However, even if initial conditions change with the massive galaxy and between individual dwarf simulations, the dust model and recipes for molecular clouds are the same. For dwarf galaxies, each simulation is described in chapter 5. The important difference to note here is that* caaa *is extremely gas rich, with a gas-to-stellar mass ratio of 1, while the others (*caab*,* caac*,* caad*,* caae*,* caaf*) have a ratio of 40 %.*

The simple criterion adopted to consider the cold phase as MC gives quite good statistics, thus provides a good proxy for activation of dust growth in ISM.

We exclude MC with lifetime $< 10^5$ yr. They cause a bump in lifetime distribution located around the mean time step duration. This is a numerical effect. Particles switches on/off dust growth each (few) time step. They have a negligible dust production since their integrated mass ($\sum_i t_i m_i$) is lower than 0.01% of total integrated mass of molecular clouds.

New: *Simulations sometimes reproduce power law mass distributions with a slope consistent with observations (see eq. 2.2) although they still struggle to reproduce the slope and the average MC mass simultaneously. For instance* low_res *is a low resolution simulation of massive galaxy and has a power index* $\alpha = 1.34$ *for MC mass between* 10^5 *and* 10^6 $M_\odot$*, giving realistic molecular cloud masses despite this small power index. For* full_4 *and* full_3*, higher resolution lowers the particle mass, thus molecular cloud masses.* However the slope is more consistent with observations: $\alpha = 1.81$ and $\alpha = 1.79$ respectively (Fig. 3.3). For dwarf galaxies, although the number and specially the masses of MC are clearly too low, we retrieve a power law distribution with the index given in Tab. 3.2.

The lifetime of giant MC is ∼30 Myr (see discussion in Krumholz et al. 2006, and references therein), with decreasing tendency for the most massive. Semi-analytic models often applies factor to the growth rate under assumption on the relative values of accretion timescale and MC lifetime (see Hirashita & Kuo 2011, and references therein). Zhukovska et al. (2008) support that dust growth timescale can be quite similar to clouds lifetime. They introduces a model assuming a distribution of cloud lifetime to infer galactic dust production rate in ISM from dust growth rate and MC lifetime.

These considerations imply to check our recipe for activation of dust growth. That is why our criterion to transform the cold phase of a particle to a "MC" must have lifetime similar to the lifetime of real MC. Fig. 3.4 displays the distribution of all "MC" formed during simulations implementing the full dust physic with a growth threshold density $\rho_{\rm mc} \in [10^3,\ 10^4]$ cm^{-3} (see chapter 4 and 5). Each time a particle switch on then off dust growth, we consider that it has been a MC. The lifetime of the MC is the duration of dust growth. The distribution is quite extended but have its main mode located around 10 Myr for the massive galaxy and caaa, while the dwarf galaxies have lifetime around 2 Myr. We have reported statistics of the truncated ($10^5 < t < 10^9$ yr) lifetime distribution for MC of our simulations in Tab. 3.3, using gamma distribution. This time, the mean lifetimes are between 1 and 10 Myr.

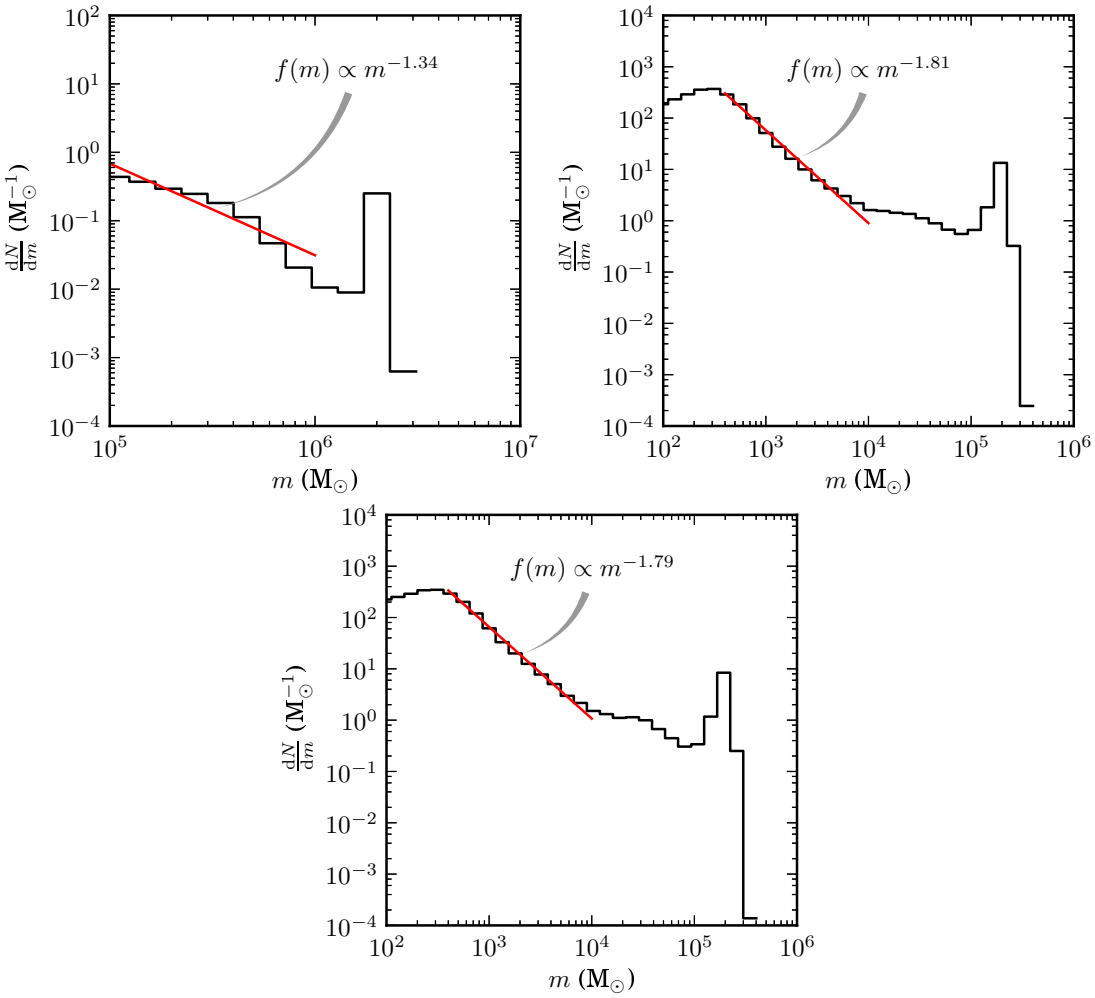

Figure 3.3: Mass distribution of all MC created during our simulations of massive galaxies `low_res` **New:** *(a low resolution simulation of a massive galaxy)*, `full_3`, and `full_4`(the same massive galaxy at higher resolution, with 10^3 and 10^4 cm-3 density threshold for molecular cloud, respectively). Each MC is counted once and its mass is the cold phase one. Fits are done using a maximum likelihood analysis. See the chapter 4 for description of the Milky Way-like simulations.

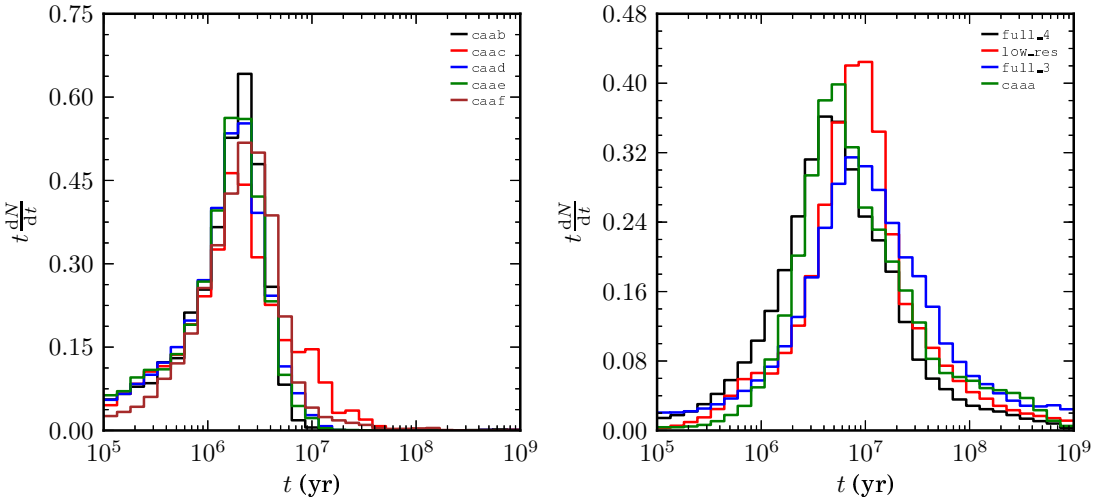

Figure 3.4: Distribution of lifetimes of all "MC". Particles are "MC" when density of their cold phase is above a threshold and accretion is therefore activated. The lifetime is the duration of "molecular" state of a particles. See the text for a simple description of the simulations, and the chapters 4 and 5 for a complete description.

simulation	$\rho_{\rm mc}$	μ (dex)	σ (dex)
`caaa`	10^4	6.95	0.61
`caab`	10^3	6.16	0.40
`caac`	10^3	6.26	0.50
`caad`	10^3	6.16	0.41
`caae`	10^3	6.14	0.41
`caaf`	10^3	6.28	0.42
`low_res`	10^4	6.95	0.59
`full_3`	10^3	7.01	0.70
`full_4`	10^4	6.74	0.61
`no_sne`	10^4	6.75	0.61

Table 3.3: log(MC lifetime/yr) statistics (mean μ and standard deviation σ) in the simulations of galaxies. We have previously selected lifetime spanning from 0.1 Myr to 1 Gyr in order to eliminate effects from tails in the distributions. See the chapters 4 and 5 for description of simulations.

3.2.4 Destruction

By supernovae

Depletion of metal in a cloud is anti-correlated with its velocity (Cowie 1978). This suggests destruction occurs in shock waves induced by SNe. Draine & Salpeter (1979) conclude shock waves is the main destruction mechanism after a review of all destructive mechanisms.

We takes the same estimation than McKee (1989) and Hirashita et al. (2002) for the mass of gas accelerated at least to a velocity v_s:

$$M_{\rm s}(v_{\rm s}) = \frac{E/10^{51}\ {\rm erg}}{(v_{\rm s}/10^7\ {\rm cm\,s^{-1}})^2} \times 6800\ {\rm M_\odot}, \tag{3.21}$$

with E the energy released by the SN at the origin of the shock. Since the shock propagates in the less dense phase we can find the covered radius by the shock in the variable phase. Then we assume that all of the cold matter inside this radius is shocked at the same velocity. This is equivalent to assume that energy of the SN is released in proportion with the filling factor to each phase: we will replace E in equation (3.21) by $E_{\rm h} = f_{\rm h}E$ and $E_{\rm c} = f_{\rm c}E$ to know the shocked mass in the variable and the cold phase respectively: $M_{\rm h,s}$ and $M_{\rm c,s}$.

Jones et al. (1996) have computed a (sparse) grid of destruction efficiency of dust as a function of the velocity of shock and density of ISM before shock: we take $\epsilon_{\rm h} = 0.1$ and $\epsilon_{\rm c} = 0.4$. For the hot phase, $\sim$0.1 is the mass-averaged value when linearly fitting the efficiency of Jones et al. (1996), for density $n_0 = 0.25\ {\rm cm^{-3}}$ along shocked velocities from 45 to 345 $\rm km\,s^{-1}$ ($\epsilon_{\rm h}(v_s)$ from 0 to 1), so we will choose $v_s = 45\ \rm km\,s^{-1}$ hereafter, as velocity to compute shocked gas mass from formula (3.21). This leads to the destroyed mass of dust by a SN:

$$M_{\rm h/c,d} = \epsilon_{\rm h/c} Y_{\rm h/c,dust} M_{\rm h/c,s}. \tag{3.22}$$

Finally we choose to implement the destruction of dust mass using

$$M_{\rm h/c,d}(E) = M_{\rm h/c,d}(0)\left[1 - \epsilon_{\rm h/c}\frac{M_{\rm SN}}{M_{\rm h/c}}\right]^{E_{\rm h/c}/E_{\rm SN}}, \tag{3.23}$$

New: *where $E_{\rm h/c}$ is the injected energy by SNe in a particle of hot/cold mass $M_{h/c}$, and $M_{\rm SN}$ is the shocked gas mass by a SN ejecting $E_{SN} = 10^{51}$ ergs applying formula (3.21) with $v_{\rm s} = 45\ km\,s^{-1}$.* The first advantage of this formula is that it is time step independent. Indeed, for one time step, we have a given $E_{\rm h/c}$ energy released into particles. This released energy change with the choice of time step, but total released energy by a stellar population at the end of a simulation does not change with the choice of time steps. Exponential form allows the destroyed mass to be a function of only the final released energy. The second advantage is the decreasing destruction when multiple SN events occur. Indeed, efficiency is obtained for one SN event, but averaged efficiency over all shocks produced by an entire stellar population is lower when multiple neighbour SNe events occur in the same time step. This is due to the decreasing dust abundance after each shock. The efficiency of a SN event therefore applies on dust abundance not destroyed by previous shocks.

When gas mass is too low to satisfy $M_{\rm h/c} > \epsilon_{\rm h/c} M_{\rm SN}$, eg. all dust will be destroyed with one SN event, we can fall back to the simple relation of equation (3.22). This occurs because SNe energy is released into neighbour particles with a summed mass smaller than the real shocked mass.

By star formation

We assume here we have no formal destruction but dust incorporated to stars is no longer available in ISM. Then, we destroy dust locked in cold gas which forms a new stellar particles, eg. we destroy a dust mass:

$$M_{\rm d} = Y_{\rm c,dust} M_{\star,\rm new}, \tag{3.24}$$

for a newly formed stellar mass $M_{\star,\rm new}$. This lets dust abundance unchanged in the remaining cold phase.

Chapter 4

First Result: The Milky Way

4.1 Simulation

New: *Our first set of simulations perform the evolution of a large, massive spiral galaxy such as the Milky Way. These simulations have identical initial conditions. Indeed, they are intended to study variations in the dust model. This is the subject of this chapter.*

An *initial* stellar population is set up to reproduce a typical disc galaxy. These stellar particles do not evolve, enrich ISM, nor produce energetic feedback. Positions for 10^6 particles are found from a superposition of two axisymmetric Miyamoto & Nagai (1975) discs of mass $M_1 = 10^{10}$ and $M_2 = 10^{11}$ $M_\odot$, of scalelengths 0.5 and 3 kpc respectively, and a common scaleheight of 0.5 kpc. Initial velocity dispersions are computed solving numerically the Jeans equations according to the Hernquist (1993) method **New:** *with a dissipative component.* Initial velocity dispersion was chosen to be anisotropic with $\sigma_r = \sigma_z$ and $\sigma_\theta^2 = \sigma_r^2\kappa^2/(4\Omega^2)$, where σ_r, σ_θ and σ_z are the three components of the velocity dispersion along radial, azimutal and vertical directions and, respectively, κ and Ω are radial and angular epicyclic frequencies.

The initial disc radius is 30 kpc. Gaseous component is represented by 50,000 particles for a total mass of 5.5×10^9 $M_\odot$ distributed in a 3 kpc scalelength Miyamoto-Nagai thin disc.

The dark matter halo is a Plummer potential ($\varphi(r) = -GM/\sqrt{(r^2 + a^2)}$ of scalelength $a = 6$ kpc and mass $M = 6.42 \times 10^{11}$ $M_\odot$.

New: *We have performed a set of simulations, varying parameters related to the dust model. These simulations start all with the same initial conditions. Recipes, and their associated parameters, do not change from one simulation to another, excluding the dust model.* We perform for ∼500 Myr cylindrical symmetric simulations without star-formation, cooling and cloud condensation/evaporation, then we switch them on in symmetry free simulations. There is no initial dust abundance. The simulations labelled `full_3` and `full_4` include all processes previously described for the dust model, using a density threshold $\rho_{\rm mc} = 10^3$ and 10^4 cm^{-3} respectively. The simulation `no_acc` removes grain growth by accretion while `no_sne` removes the production of dust by SNe. See Table 4.1 for a summary.

New: *The initial abundances for the gaseous component are primordial, and have no effect for initial stellar particles since they do not evolve, enrich nor heat the ISM. There is no initial dust abundance in any simulation.*

Table 4.1: Parameters for dust model for each run.

run	description	accretion threshold $\rho_{\rm mc}$	duration
`full_4`	full model	10^4 cm^{-3}	4.034 Gyr
`full_3`	full model	10^3 cm^{-3}	3.516 Gyr
`no_acc`	no accretion	n/a	3.835 Gyr
`no_sne`	no SNe production	10^4 cm^{-3}	3.973 Gyr

4.2 Analysis

4.2.1 Radial distribution of dust

In Fig. 4.1, we compute radial gradient integrating either dust and oxygen density over cylinder for a given radius R and using SPH formula:

$$\int_{0,-\infty}^{2\pi,\infty} (Y_X \rho_{\rm gas})(R,\theta,z){\rm d}\theta{\rm d}z = \int \sum_p \frac{Y_{X,p}\rho_p}{\rho_p} M_p W_p(R,\theta,z){\rm d}\theta{\rm d}z, \quad (4.1)$$

$$= \sum_p Y_{X,p} M_p \int W_p(R,\theta,z){\rm d}\theta{\rm d}z. \quad (4.2)$$

where Y_X is the mass fraction of element X (either dust or oxygen), ρ the density, M the mass, W the SPH kernel function, summed over all gaseous particles p. We compute both dust and oxygen density, then we get ratio $\rho_{\rm dust}/\rho_{\rm O}$ (or dust-to-oxygen) radial distribution. We use this quantity to discuss the effects of various physical processes implemented to describe dust creation and destruction cycle. However, it must be noted that similar conclusions can be drawn from dust-to-Fe ratio.

The two simulations with the full dust model implementation (`full_3` and `full_4`) show very similar radial distributions at t=1 Gyr. This implies that our choice of density threshold $\rho_{\rm mc}$ has no dramatic effects on gradients on short timescales. However, integrated over a longer timescale (e.g. up to 2 Gyr), the factor ten in $\rho_{\rm mc}$ has an impact on the absolute value of $\rho_{\rm dust}/\rho_{\rm O}$. `full_4` shows a lower dust-to-oxygen ratio, decreasing with radius. For this simulation, $\rho_{\rm dust}/\rho_{\rm O}$ at $R \gtrsim 3$ kpc decreases from t=1 to 2 Gyr. `full_4` displays a small depression around $R \approx 2$ kpc at t=1 Gyr. This depression extends to larger radius and is responsible for the decrease of dust-to-oxygen ratio and the small negative gradient at $t = 2$ Gyr. It is due to an increase of oxygen abundance at large radius. Since there is no such bump in `full_3`, this means that accretion is efficient to lock oxygen into dust at large radius in `full_3`, while it is not in `full_4`. However it could be argued that this effect remains rather small on this timescale (a factor of $\approx$2 on dust-to-oxygen ratio at R=10 kpc). For `full_3` and `full_4` dust-to-oxygen ratio increases in central part of the galaxy.

Accretion and destruction from SNe have clear effects, on galactic value of dust-to-oxygen fraction, as well as gradients. The simulation without accretion, `no_acc`, demonstrates the strong effect of accretion process on the amplitude of dust-to-oxygen ratio. The mean dust-to-oxygen ratio is more than a factor of 10 lower than ratio in the two simulations `full_3` and `full_4`. However, it increases by a factor of 4–5 between t=1 and 2 Gyr but still remains well below the values for `full_4` and `full_3` (see also Fig. 4.5).

`no_acc` also displays positive gradient for $R \lesssim 2.3$ kpc at early stage of the run t=1 Gyr. The positive gradient evolves towards a plateau from R=0 kpc to $R \approx 7$ kpc at t=2 Gyr. Since SF and

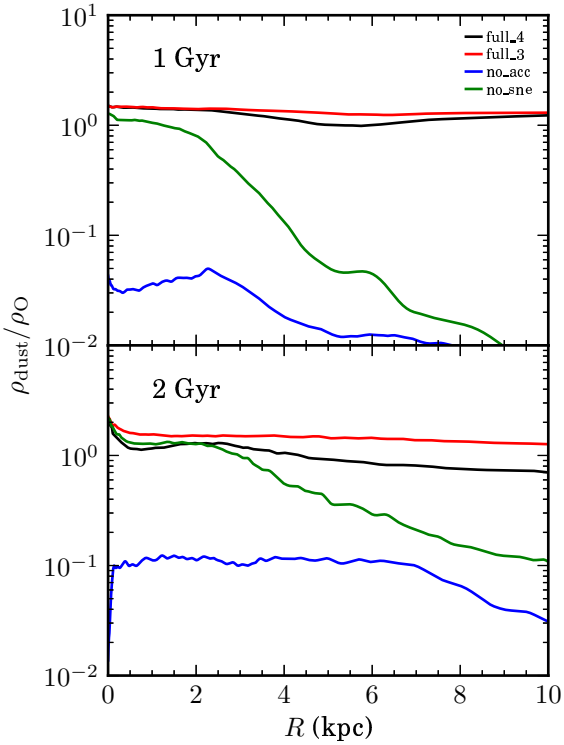

Figure 4.1: Dust-to-oxygen gradients after 1 and 2 Gyr, computed using the SPH formula (4.2).

SNe are concentrated in the central part and at the beginning of the simulation, this suggests destruction plays a major role in formation of positive dust-to-oxygen gradient.

The dust-to-oxygen ratio strongly decreases with radius at both times of `no_sne`, as displayed in Fig. 4.1. The gradient is steeper for `no_sne` than for the full models (`full_3` and `full_4`), with a break at $R{\approx}2$ kpc, where $\rho_{\rm dust}/\rho_O$ strongly decreases. This simulation shows that the production of dust by stars, then accretion, is mostly concentrated in the central part, where most of the star formation occurs. Between t=1 and 2 Gyr, the dust-to-oxygen ratio also shows a strong increase in the external part ($R{\gtrsim}2$ kpc). The slope therefore decreases during ≈1 Gyr.

The dust-to-oxygen gradient is steeper for `no_sne` than for `full_3` and `full_4`. This suggests an efficient dissemination role for SNe, formed in the central part of the galaxy. When SNe release high energy into ISM, producing flows, they also release dust. Indeed, Fig. 4.2 shows an outward flow for radii above ∼5 kpc, due to energy released by core-collapse SNe just after star formation was allowed. When dust is produced by these SNe, it can be efficiently disseminated with the flow, which therefore flattens the dust-to-oxygen gradient. **New:** *With our model, dust and gas dynamics are coupled since components are mixed. The flows are an effect of heating by SNe, mainly at the center of the galaxy: pressure increases, then gas starts to have a radial velocity to the outer part of the galaxy. Indeed, outflows and/or infall are not explicitly implemented as recipes. Consequently, assuming only that dust is transported with gas, flows can disseminate the dust, as our model does.*

In Fig. 4.3, gradients for `no_sne` evolve just after star formation. Star formation rate (SFR) briefly increases from 0.30 $\mathrm{M}_\odot\,\mathrm{yr}^{-1}$ the 131 Myr before $t = 1.50$ Gyr to 1.62 $\mathrm{M}_\odot\,\mathrm{yr}^{-1}$ after. This

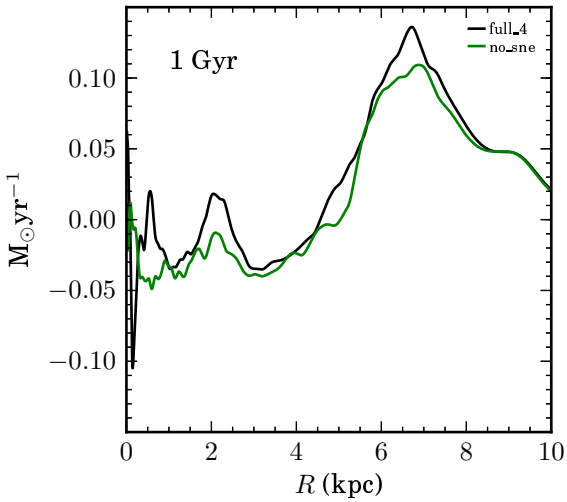

Figure 4.2: Radial gaseous flow, outflows are positive. For a given cylindrical radius R, we compute the field ρv_R integrated on the cylinder of radius R with a formula similar to (4.2), where ρ is gas density and v_R radial velocity of gas.

extends dust-to-oxygen gradient. This shows that star formation extends dust disk more than oxygen.

Discussion

Many authors have reported a dust gradient in galaxies (Muñoz-Mateos et al. 2009; Bendo et al. 2010; Pohlen et al. 2010; Smith et al. 2010) implied by metallicity gradient and approximately constant fraction of metal locked in the solid phase. Magrini et al. (2011) compare dust gradients with metallicity gradients.

Mattsson & Andersen (2012) have used dust and oxygen gradients to find out the so-called *net* dust evolution of SINGS galaxies from gradients derived by Muñoz-Mateos et al. (2009). They argue that respective values of dust and metallicity gradient sign provide a good proxy for dust history of galaxies. Assuming negative oxygen gradient (oxygen taken as an estimator of metallicity), which is the case for most of the snapshots in our simulations, we are able to use their global result to interpret our gradients: *net* destruction make positive dust-to-oxygen gradients and grain growth renders negative dust-to-oxygen gradients.

Our self-consistent chemodynamical simulations confirm the analysis proposed by Mattsson et al. (2012). This allows to know contribution of each dust processes: stardust, destruction and accretion. The idea is to exploit differences of dust and oxygen production. Indeed, we find simulation without powerful production process, `no_acc` makes positive dust-to-oxygen gradient in the central part of the galaxy, where stars form, at $t = 1$ Gyr. However dust density continuously increases in this simulation, in spite of the effect of destruction. Indeed, the destruction has a visible effect on gradients because of differential increase between dust and oxygen abundances. Galaxy has an efficient destructive effect from SNe in the central part. For outer radius, gradient is negative indicating a *net* production effect since SNe rate decreases, thus destruction is less efficient. Production therefore tends to flatten gradients or make them negative.

Mattsson et al. (2012) and Mattsson & Andersen (2012) have implicitly assumed there is

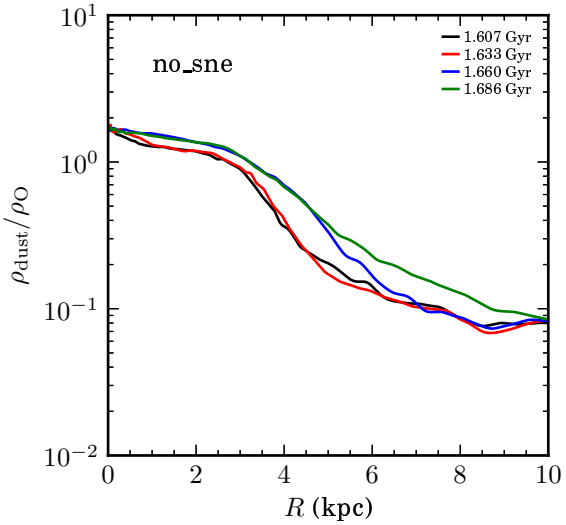

Figure 4.3: Radial dust-to-oxygen ratio in the simulation without SNe dust production, for four consecutive snapshots just after an increasing SFR.

no mixing of gas since evolution is followed independently for each radius, assuming no radial migration and/or diffusion of gas and dust. However, we show:

- dust disk extends, more than oxygen disk, when we have a burst of star formation;
- dust is efficiently disseminated when SNII dust production is activated, flattening dust-to-oxygen gradient.

Our simulations show dust gradients cannot be properly determined if hydrodynamic and energetic feedback from SNe is not included in models. This results in a flattening of dust-to-oxygen gradient (see Fig. 4.1, `full_3` and `full_4`) due to flows induced by feedback from SNe (see Fig. 4.2). The idea of dust propagation was first proposed by Jones (2005) which argues shocks from SNe transports dust, contrary to stellar winds.

4.2.2 Vertical distribution of dust

Fig. 4.4 is obtained with formula similar to equation (4.2) integrating on planes at height z. Similar conclusions can be drawn from dust-to-oxygen ratio behaviour with distance to galactic plane z. Since our disc is thin, vertical scale height is small compared to radial scale. Vertical gradients are thus steeper.

For `full_4` and `full_3`, $\rho_{\rm dust}/\rho_O$ ratio is almost constant with varying z. This means that $\rho_{\rm dust}$ and ρ_O remain strongly correlated when they decrease with z, following decreasing gas density. However, this is not the case for the runs `no_sne` and `no_acc`. Lack of dust production in these two simulations creates vertical gradient. For z profiles, like radial distribution, lower dust-to-oxygen ratios are obtained when accretion mechanism is switched off (`no_acc`). Dissymetry of `no_sne` profile changes at each snapshot (one per 25 Myr) depending on SNe winds that eject dust and metals to high $|z|$. Hence, vertical gradient of $\rho_{\rm dust}/\rho_O$ ratio is a diagnostic on potential imbalance in various dust production and destruction mechanisms. Like radial gradients, vertical gradients should be useful to understand these mechanisms of dust production and destruction.

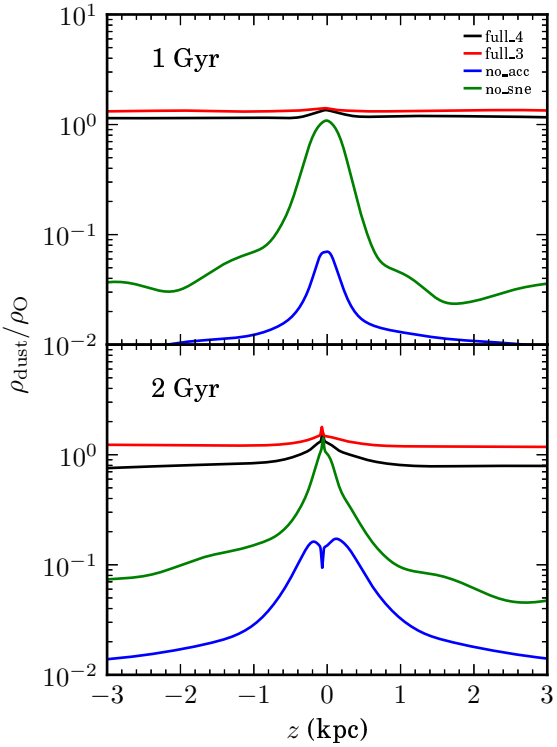

Figure 4.4: Vertical gradients computed like radial gradients, integrating along planes at height z.

4.2.3 Evolution of the dust-to-gas ratio

Fig. 4.5 shows time evolution of M_{dust}/M_{gas} ratio until t=2 Gyr. `full_3` and `full_4` simulations, which implement a complete description of production and destruction mechanisms, produce the largest relative amount of dust among the four simulations, as it could be expected according to our discussion on radial distribution.

New: *Despite the same initial conditions, we have not the same evolution. This is likely to be due to slight differences of the performed runs, that may be amplified by numerical errors. However, these differences do not change the results exposed hereafter, provided we consider the star formation history as the basis for the analysis.*

Indeed, different star formation histories produce different evolutions of dust-to-gas ratio. Thus, dust fraction of `full_4` increases above `full_3` at $t\approx$1.25 Gyr while star formation increases for `full_4` and continues to decrease for `full_3`. The dust fraction of `full_3` increases to reach the dust fraction of `full_4` only when star formation begins to increase for the former simulation, at $t\approx$1.5 Gyr. This shows that with accretion activated, star formation helps to form dust.

Accretion process is mainly responsible for very short production timescale. Indeed, for `no_acc` simulation, dust-to-gas mass ratio remains well below $\approx 10^3$, the upper limit reached for the other cases. The effect is spectacular since dust fraction increases over two order of magnitude in roughly 100–200 Myr. It is noteworthy that the value of ρ_{mc} has no impact on the result. If dust production from SNII is set off, the evolution of galactic dust-to-gas ratio is delayed by $\sim$ 100 Myr when the ratio increases to 10^{-4}.

Although accretion is a fast process (see Fig. 4.5), we are not able to retrieve high 7×10^8 $M_\odot$ dust mass, for quasar J1148+5251, observed by Bertoldi et al. (2003a,b) at redshift 6.42. It is not surprising because they derive a H_2 mass of 2×10^{10} $M_\odot$ for the quasar whereas our initial conditions have less gas (1.1×10^{10} total molecular *plus atomic* gas mass). Even if a quantitative conclusion cannot be drawn from our simulations since we do not cover galactic formations in cosmological environment, we can observe that switching off SNe production shifts dust-to-hydrogen evolution by 100 Myr. Hence, we conclude accretion provides a fast production mechanism of dust. Moreover, SNII production could have a negligible effect on dust production rate. This means that age of quasars must be precisely determined in order to discriminate model with or without SNII production of dust in the young universe. However, our simulations do not compute formation of galaxy, and these results are only indicative.

4.2.4 Evolution of the dust-to-oxygen ratio

Dust-to-oxygen ratio evolves differently depending on whether production of dust by accretion is switched on or not. Indeed, in Fig. 4.6 we plot dust-to-oxygen evolution for `full_3` and `no_acc`. We have chosen to compare `no_acc` with only `full_3` since their SFH are quite similar during the first 1.55 Gyr and both simulations display a moderate burst of star formation at same epoch and with same duration ($\approx$250 Myr) around $t\approx$1.45 Gyr.

The SFR of `full_3` and `no_acc` begins to significantly increase at $t\approx$1.3 Gyr, above 1.2 $M_\odot$/yr. For `full_3`, dust-to-oxygen ratio increases from $\approx$1.4 to $\approx$1.7 Gyr in 250 Myr, while `no_acc` displays a plateau on the same epoch. On contrary, when star formation is low before the burst, 1 Gyr$\lesssim t\lesssim$1.3 Gyr, or after, 1.55 Gyr$\lesssim t\lesssim$1.7 Gyr, dust-to-oxygen ratio remains nearly constant in `full_3`, at $\approx$1.4 before and at $\approx$1.7 after the burst. For `full_3`, dust-to-oxygen ratio increases by $\approx$0.02 in 200 Myr.

Since the difference between the two simulations is the switch on/off of accretion process, production of oxygen is not in question. It is clear that with accretion dust fraction increases with star formation, whereas without accretion dust fraction stops to increase when stars form. On Fig. 4.5, departure between `full_3` and `full_4` for $t\in[1.25, 1.5]$ Gyr can be attributed to

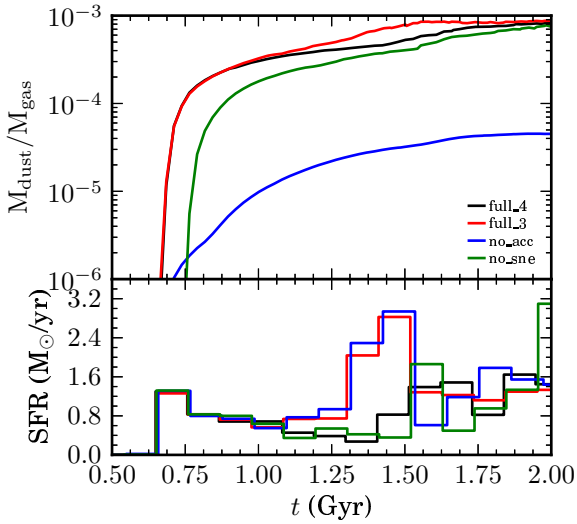

Figure 4.5: **Top:** average dust abundance in simulations, summing mass of dust and mass of gas, then computing ratio, for each snapshot. **Bottom:** star formation rate (100 Myr bins).

difference of SFH between the two simulations. This will have important implication for oxygen versus dust abundances diagram studied in the following section.

4.2.5 Dust–metallicity diagram

Combining dust abundance with oxygen abundance provides an important diagnostic tool since it directly checks simulations against previous observational works, in particular those cited Sect. 2.4.5. Hence, we have followed two different approaches to compute dust–metallicity diagram (cf. Fig. 4.7 and 4.8).

For *global* diagram (Fig. 4.7), each snapshot of a simulation is displayed as a point. Masses of all gas particles, for the whole extent or inside a given limiting cylindrical radius R, is summed up. Repeating the operation for each snapshot gives a path indicating evolution of each simulation.

For *local* diagram, we populate 2D histograms in $\log(M_{dust}/M_H)$–$\log(M_O/M_H)$ space, using a spatially uniform sampling of $20 \times 20 \times 2$ kpc region, for a given snapshot at time t. We display logarithm of the histogram. This adds local information on dust–metallicity distribution that is not available when global metallicity or dust content is computed.

It is tempting to make a direct and naive comparison with data taken from literature (see Sect. 2.4.5). However, a point cannot be stressed enough: observations are done with samples spanning a wide range of galaxy masses and sizes, whereas all of our four simulations are performed starting with same total high mass.

The *global* diagram (Fig. 4.7, top panel) displays the path followed by our four simulations taken as a whole. Trend is the same for the four cases, that is any simulation moves from metal-poor, dust-free region to metal-rich, dusty part of the diagram. The simulations are however far from reaching solar abundance after 2 Gyr only. This is clearly due to the fact we have computed the properties for the whole disc, including the outermost regions, without any star formation nor dust production. If we plot only the values obtained for central 1 kpc (Fig. 4.7, bottom panel), the paths extend to upper right region, up to solar values. Hence, enrichment of central region is obviously quicker.

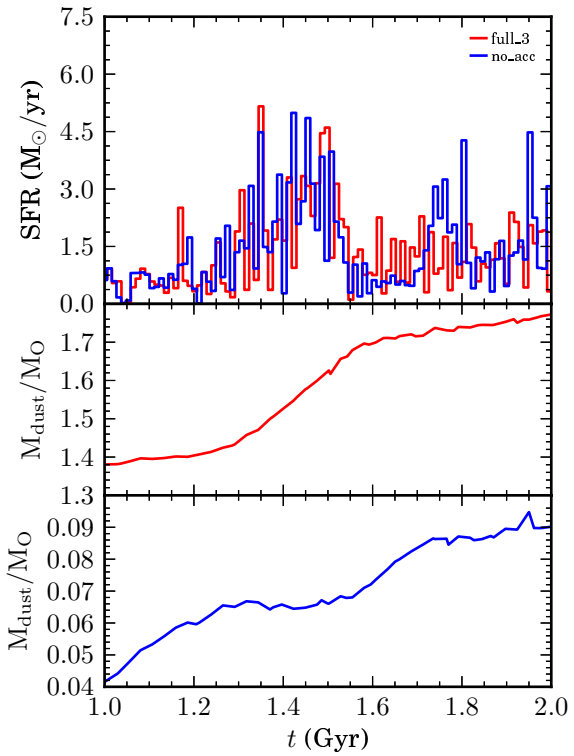

Figure 4.6: **Top:** SFR (10 Myr bins) of the full model and simulation without accretion. We have a "starburst" at 1.4–1.5 Gyr. **Middle:** dust-to-oxygen fraction for the full model. **Down:** dust to oxygen fraction for the model without accretion.

full_4 and full_3 are not distinguishable on this plot since their evolution is very similar. They are in good quantitative agreement with the more dusty galaxies, whatever their metallicity is, while no_acc, setting off grain growth, agrees with the more dust-poor galaxies. Our simulations therefore bracket the full range of dust abundance.

full_3 and full_4 nearly follow linear relation like eq. (2.6). This implies that O/Fe ratio, depending on SNe versus long-lived stars enrichment and consequently star formation history, has a little noticeable effects. Then, thanks to the tiny impact of varying O/Fe, we can consider oxygen as a good tracer for metallicity in (our) studies.

no_sne quickly reaches dust fraction of full_3 and full_4. On the contrary, at very low metallicity ($M_O/M_H \lesssim 10^{-3.4}$), metal locked into dust is lower than for full_3 and full_4. no_acc reproduces dust abundance of metal-poor galaxies, thanks to efficient destruction which keeps dust abundance nearly constant, $M_{dust}/M_H \lesssim 10^{-4}$, over a large range of metallicity. Setting off accretion lowers dust abundance down to $\sim$1 dex at low metallicity and $\sim$2 dex at high metallicity.

For no_acc in Fig. 4.7 (top panel), we obtain a knee at $M_O/M_H \approx 10^{-3.2}$ (also visible in bottom panel at higher metallicity) due to an increase in dust mass without oxygen enrichment. We have seen in the Sect. 4.2.4 that dust fraction is constant while oxygen increases. This occurs before the knee. After that low SFR produces low oxygen enrichment while stardust mass increases, then the knee is produced after starburst. For full_3 and full_4, the knees located at the same metallicity are produced during burst of SF. Since stars enrich ISM also with oxygen, knees are less obvious.

The *local* diagram Fig. 4.8 (left panels) confirms the need to add accretion to have dust abundances similar to observations, specially for high metallicity galaxies. For very low metallicity galaxies, we retrieve observed dust abundances, $\rho_{dust}/\rho_H \simeq 10^{-4}$, using the model without accretion, no_acc. This suggests again that low metallicity galaxies have dominant destruction process when compared with accretion. Since low metallicity galaxies are dwarf, accretion should be efficient only for massive galaxies.

Fig. 4.8 (right panels) compares full_4 with no_sne. For low metallicity environment, destruction process appears a little more efficient if SNe do not produce any dust. Reader should note here we do not necessary mean no SNe production at all, however SNe do not enrich ISM with dust, because of destruction in remnants by reverse shocks. In all case, even with accretion, regions have dust abundance as low as abundance in dwarf and metal-poor galaxies.

To conclude, the full model is able to reproduce the linear relation of dust and oxygen abundances. This model computes dust abundance giving systematically the highest abundances reported by observations. Hence, at low metallicity the full model computes a upper limit of observation, and the model without accretion is necessary to provide a lower limit. At high metallicity, and for massive galaxies, dust abundance is likely to be a constant ratio of metallicity, and the simulations are in agreement with observations.

4.2.6 Other diagrams

We have studied dust behavior with similar diagram replacing O abundance with Fe. Fe provides an interesting tracer because it is more related to long-lived stars than oxygen which is typical of α elements produced by core collapse SNe. Fig. 4.9 displays an approximately linear relation for full_3 and full_4, quickly reached by no_sne. Then long-lived populations begin to enrich ISM after $t \approx 1.6$ Gyr, Fe abundance continues to increase while α production decreases. This results in a broken path and a plateau ($M_{dust}/M_H \approx 10^{-2.6}$ for full_3, full_4, and no_sne and $\approx 10^{-4}$ for no_acc). This is also visible on the *local* diagram of full_4.

Figure 4.10 is a dust-density weighted diagram in [$\log(M_{dust}/M_O)$, $\log(M_O/M_{Fe})$] space.

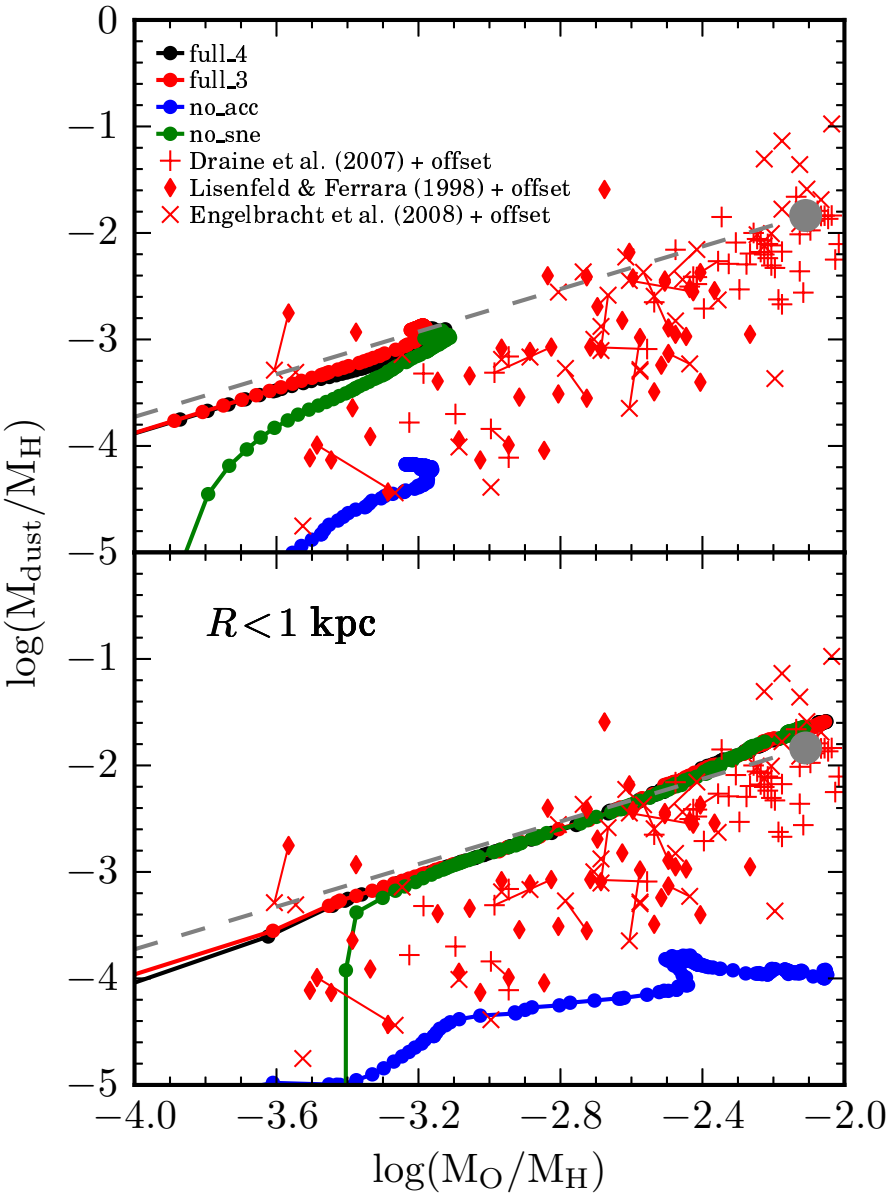

Figure 4.7: Metallicity and dust abundance evolution. The simulations move from bottom left to upper right with chemical evolution. See the Sect. 2.4.5 for description of observed points from three papers. The dashed grey line is the maximum dust possible for solar abundances, and the filled circle indicates solar abundance ($12 + \log[\mathrm{N(O)/N(H)}] = 8.69$ from Asplund et al. 2009). **Top:** entire galaxies. **Down:** central 1 kpc.

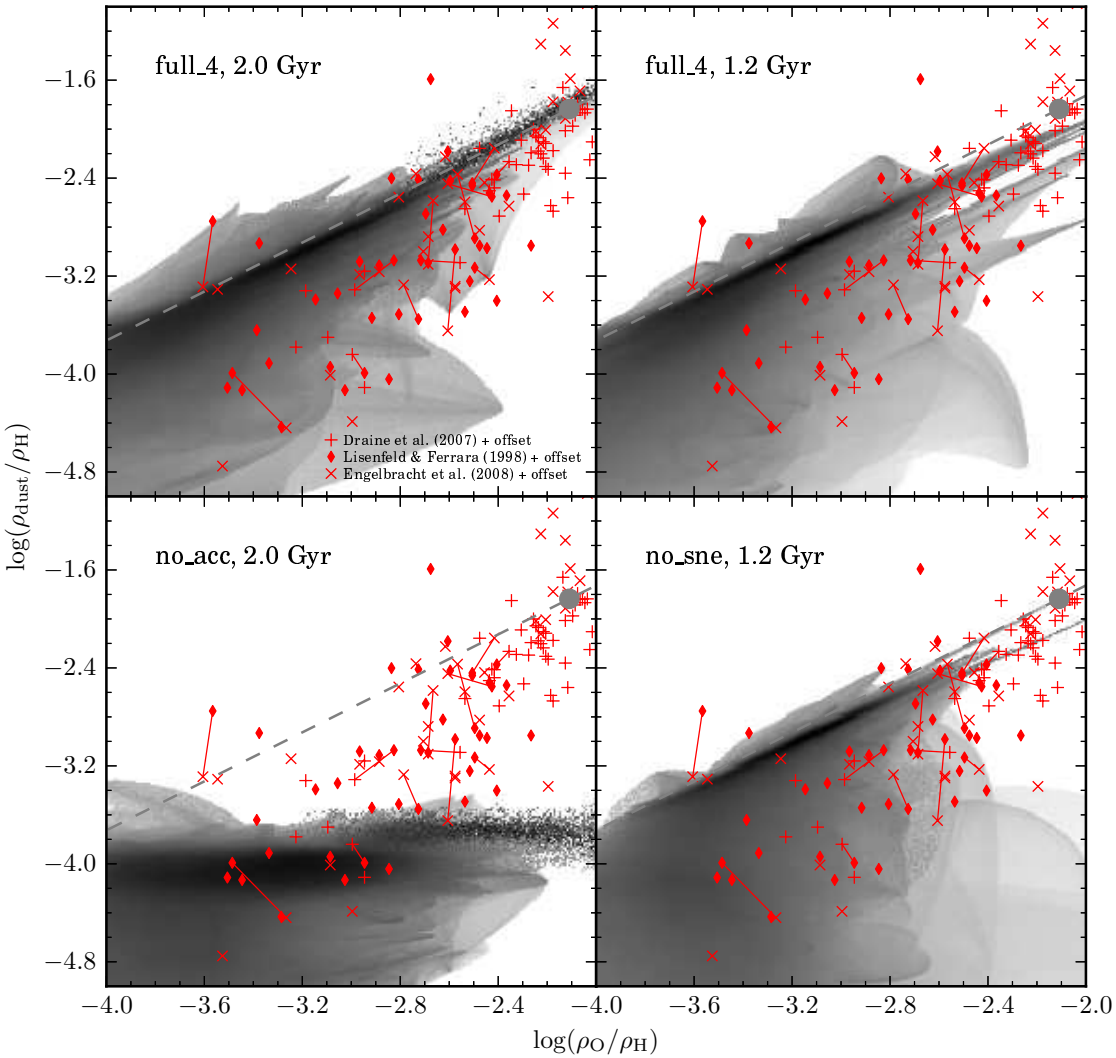

Figure 4.8: **Left top:** *local*, mass distribution, diagram for the full model at ∼2 Gyr with accretion threshold $\rho_{\rm mc} = 10^4$ cm^{-3}. **Right top:** the same model at 1.2 Gyr. **Left down:** the model without accretion at 2 Gyr. **Right down:** the model without SNe production at 1.2 Gyr.

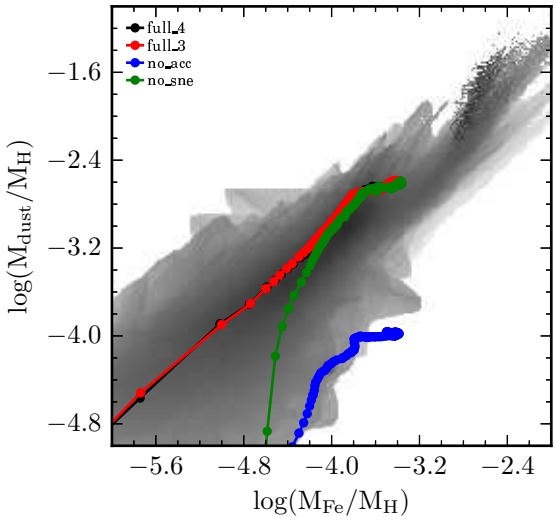

Figure 4.9: *Global* diagram for the four simulations, inside $R < 5$ kpc and *local* diagram for `full_4` at $t = 3$ Gyr.

Long-lived population also change chemical behaviour of ISM. When the galaxies evolve they move toward low oxygen-to-iron ratio and increasing dust-to-oxygen. We can distinguish three regimes in the path followed by `full_3` and `full_4`. The first, for $M_O/M_{Fe} \gtrsim 10^{0.9}$ has a low fraction of oxygen and iron locked in dust. The second regime displays an increasing dust-to-oxygen ratio without a change in oxygen-to-iron ratio. It is due to production of AGB stars since this regime is also reached by `no_sne`. The third regime for $M_O/M_{Fe} \lesssim 10^{0.9}$ displays an increasing dust-to-oxygen ratio as well as a decreasing oxygen-to-iron ratio, such that constant fraction of oxygen and iron is locked in dust (see grey line which assumes dust mass is proportional to oxygen plus iron mass). The *local* diagram shows dust mass distribution mainly agrees with a constant fraction of dust according to oxygen and iron.

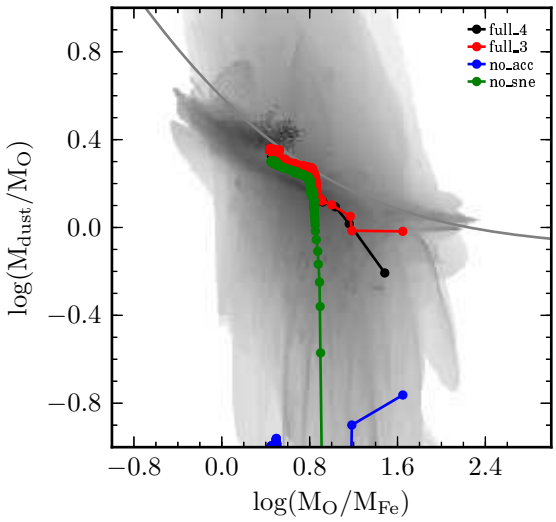

Figure 4.10: *Local* dust-density weighted diagram for `full_4`, in α–$\log(\mathrm{M_{dust}}/\mathrm{M_O})$ space, at $t = 3$ Gyr and *global* diagram inside $R < 5$ kpc. Grey line is an eye-guide which assumes $\mathrm{M_{dust}} \propto \mathrm{M_O} + \mathrm{M_{Fe}}$

Chapter 5

Second Result: The Dwarf Galaxies

5.1 Simulations

New: *In the previous chapter, we have studied simulations of a massive galaxy. Now, we will study production and destruction of dust in dwarf galaxies. This allows us to decrease the low limit of metallicity down to metal-poor galaxies in order to include them in dust–oxygen diagrams. We expect a different behaviour of dwarf galaxies, to explain their underabundance of dust.*

We want to perform simulations of a grid of dwarf galaxies. Each dwarf galaxy has a different set of parameters to compute initial conditions of the simulation. However, we need to reduce the number of parameters fixing a subset and using relations. Indeed, the method should reduce the total number of simulation and gives simulated galaxies similar to real galaxies.

5.1.1 Dark matter

Oh et al. (2011) use HI data of seven dwarf galaxies from THINGS. They derive rotation curves. NIR, 3.6 μm IRAC data, luminosity profile allows to know the mass distribution of the stellar component. Gas surface density is directly known using THINGS data, assuming constant gas-to-HI mass ratio of 1.4. Dark matter mass distribution is fitted with pseudo-isothermal halo model thanks to rotation curves subtracting contribution from baryons. The pseudo-isothermal halo model is used in our simulations, with two parameters, the central density ρ_0 and the radius $r_{1/2}$ where the density is $\rho_0/2$:

$$\rho(R) = \frac{\rho_0}{1 + (r/r_{1/2})^2}. \tag{5.1}$$

Fig. 5.1 shows a relation between the radius $r_{1/2}$ and the central density ρ_0. One could argue that the sample is too small to conclude on the relation, but the goal here is only to find simple relations. We expect these relations to be universal. Nevertheless, they have not to be, this means that we will perform simulations of a subset of available parameter space for dwarf galaxies. However, this particular relation has been studied by Kormendy & Freeman (2004) with a bigger sample. Since the relation between radius and density is established, we choose to use a new parameter, the mass of "dark core" arbitrary defined by:

$$\mathrm{M_{DM}} \equiv \frac{4}{3}\pi\rho_0 r_{1/2}^3. \tag{5.2}$$

galaxy	*dark core mass* M_{DM}
Holmberg I	$1.3 \times 10^7\,M_\odot$
Holmberg II	$1.4 \times 10^7\,M_\odot$
M81 Dwarf B	$4.2 \times 10^7\,M_\odot$
DDO 154	$2.7 \times 10^8\,M_\odot$
NGC2366	$3.7 \times 10^8\,M_\odot$
DDO 53	$4.2 \times 10^8\,M_\odot$
IC 2574	$6.5 \times 10^9\,M_\odot$

Table 5.1: Dark core mass of galaxies from Oh et al. (2011). Dwarf galaxies range from 10^7 to $10^9\,M_\odot$.

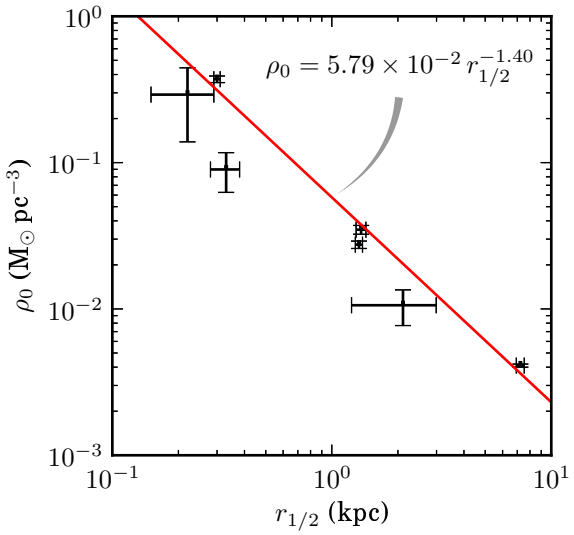

Figure 5.1: Relation between the radius and the density of dark core in few galaxies. From left to right: Holmberg I, M81 Dwarf B, Holmberg II, DDO 154, NGC2366, DDO53, and IC2574 (not a dwarf). Data from Oh et al. (2011).

For a given value of dark core mass we compute the density and the radius of the dark core using the relation

$$\rho_0 = \alpha\,M_\odot\,\mathrm{kpc}^{-3}\left(\frac{r_{1/2}}{1\,\mathrm{kpc}}\right)^{-\beta}. \tag{5.3}$$

We find and use $\alpha = 5.79 \times 10^7\,M_\odot\,\mathrm{kpc}^{-3}$ and $\beta = 1.40$. For instance, Kormendy & Freeman (2004) find $\alpha = 7.94 \times 10^7\,M_\odot\,\mathrm{kpc}^{-3}$ and $\beta = 1.20$.

5.1.2 Stellar and gaseous components

Fig. 5.2 displays mass of stars and gas as a function of dark core mass. Mass of baryons does not relate to dark mass. However, it spans from $\sim 6 \times 10^8$ to 10^9 $M_\odot$ for dwarf galaxies, and it is 3.1×10^9 $M_\odot$ for IC2574. We choose to perform simulations of galaxies with a baryon mass from 4×10^8 to 3.1×10^9 $M_\odot$. Stellar component does not evolve, contrary to stellar particles born during the simulation.

Gas-to-stellar mass ratio is highly variable, from ~ 5 % to above 100 %. I choose to use a constant fraction 40 %, except for `caaa`, a gas rich galaxy with the same mass of gas and stars.

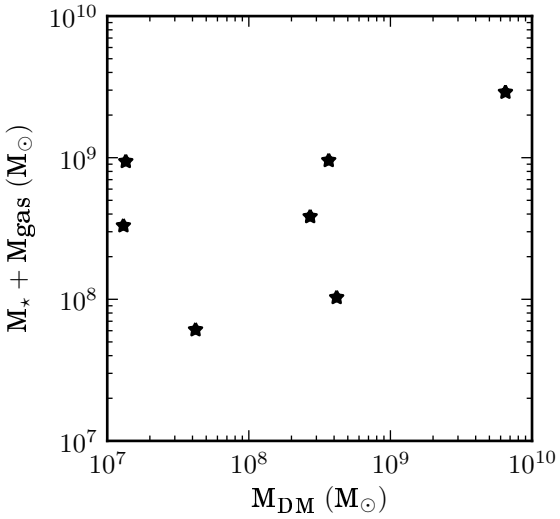

Figure 5.2: Mass of stars+gas versus mass of dark core of dwarf galaxies using data from Oh et al. (2011).

To relate radius scale length to solar mass, I use Fig. 5.3. Size is about 0.8 kpc, up to 2 kpc for dwarf galaxies, more massive galaxies allow for bigger extent. I choose to have constant radius to height scale length of 5 (Oh et al. 2011). Consequently, I have a fully defined exponential stellar disk. However, the code cannot set exponential disc for initial conditions and I had to use a Miyamoto-Nagai profile, with potential:

$$\varphi(r,z) = \frac{GM}{\{R^2 + [a + (z^2 + b^2)^{1/2}]^2\}^{1/2}}. \tag{5.4}$$

To convert exponential to Miyamoto parameters, minimization algorithm has been applied to the integral of the squared difference of each profile.

HI discs are known to be extended (Walter et al. 2008). To confirm this we use observations from THINGS to fit a simple model of thin exponential disk with least square method (see Fig. 5.4). From Tab. 5.2, we choose to have constant gas-to-stellar scale length ratio of 3. The disk is thin (scale height of 10^{-4}).

5.1.3 Summary

Resulting choice of simulations is given Tab. 5.3. Simulations are performed ~ 1 Gyr in axisymmetric mode (~ 0.5 Gyr for `caaa`), without star formation to stabilize initial conditions, before a full chemodynamical run during ~ 9 Gyr.

`caaa` is one of the less massive galaxies, specially for its halo mass. The first performed simulation of this galaxy did not chemically evolve with a gas-to-stellar mass ratio of 40 % like other simulations. Consequently I have set gas-to-stellar mass ratio to 1. The second simulation, `caab`, has the same dark halo. However, its stellar mass, and disk size are bigger. `caac`, `caad`, and `caae` have the same disk sizes than `caaa`. `caac` and `caad` share same dark halo while stellar mass varies. On contrary, `caad` and `caae` have the same baryonic mass while dark halo mass varies. Finally `caaf` is a simulation of a medium-sized galaxy.

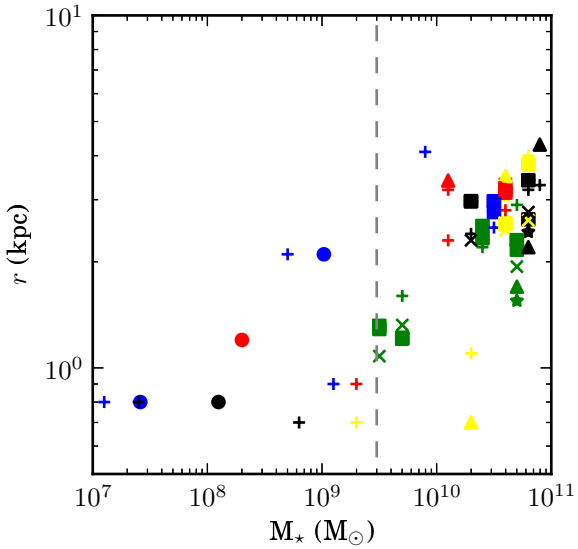

Figure 5.3: Mass versus exponential scale length of stellar disc of galaxies. Data from Regan et al. (2001), Draine et al. (2007), Leroy et al. (2008), Tamburro et al. (2008), and Oh et al. (2011). All dwarf galaxies are at the left of the vertical line $M_\star = 3 \times 10^9\,M_\odot$.

name	*source*	$R_\star$ (kpc)	$R_{\rm HI}$ (kpc)	$R_{\rm HI/\star}$
NGC2403	L	1.6	7.1	4.4
	T	1.2	7.2	4.5
NGC2903	R	1.7	7.0	4.1
NGC2976	L	0.9	1.6	1.8
NGC3521	R	1.7	7.3	4.3
	L	2.9	10.8	3.7
	T	2.2	10.2	4.6
NGC4214	L	0.7	2.4	3.4
NGC4736	R	0.7	2.1	3.0
	L	1.1	2.3	3.4
DDO154	L	0.8	3.1	3.9

Table 5.2: Stellar and HI scale length of few galaxies. Error on distances induces differences on the scale lengths. However the error vanishes since we consider ratio of the scale lengths. Sources for the distance of galaxies and the stellar scale length are Leroy et al. (2008) for L, Regan et al. (2001) for R, Tamburro et al. (2008) for T.

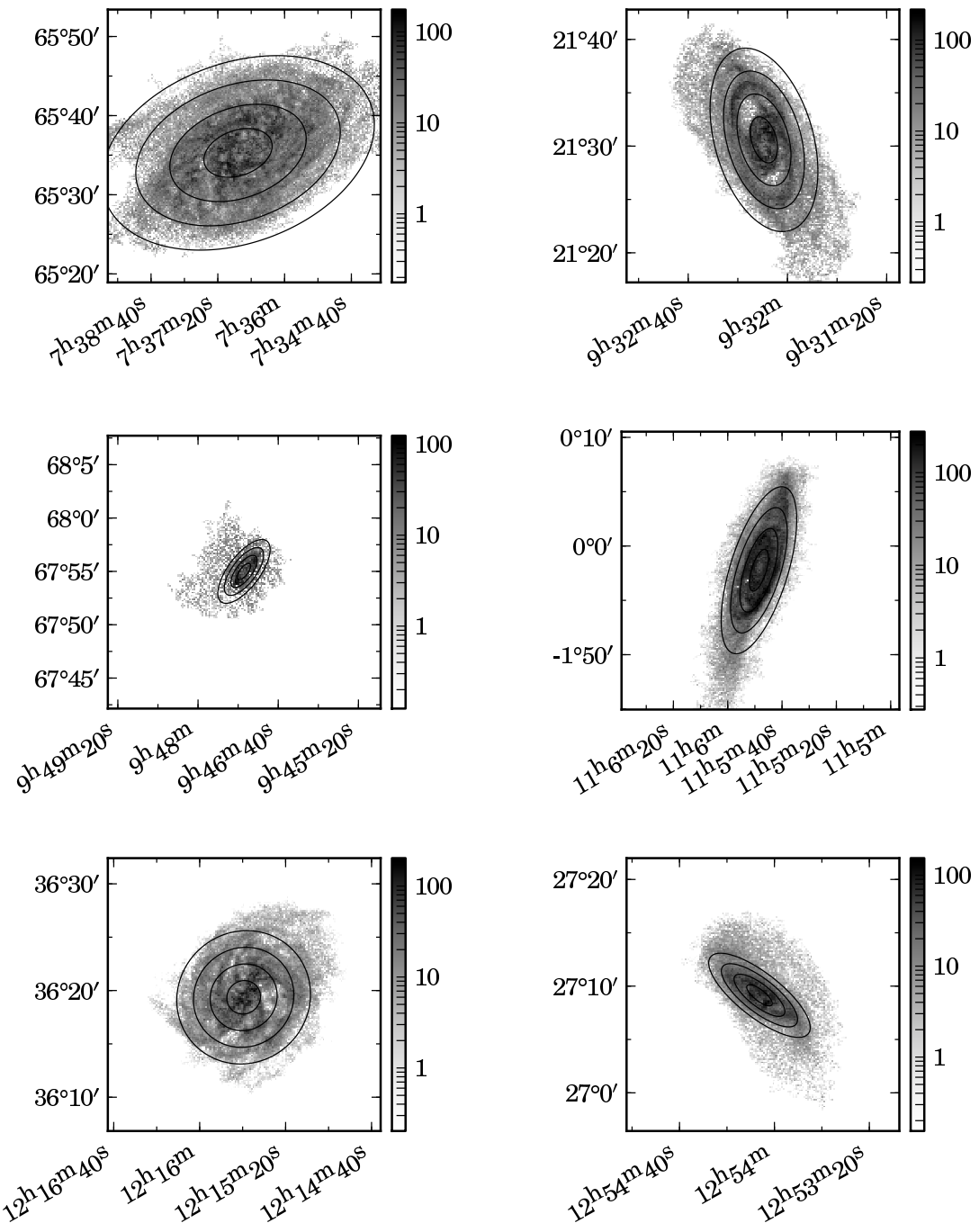

Figure 5.4: HI fits of NGC2403 and NGC2903, NGC2976, NGC3521, NGC4214, DDO154. The two last are dwarf galaxies

Our grid of galaxies is not representative of the various galaxies found by observers. Nevertheless our aim is to reproduce a set of parameters for few typical dwarf galaxies and one medium-sized galaxy. Moreover, we do not reproduce an entire evolution of these dwarf galaxies, from formation in early universe to their current state in local universe. We look for a numerical experiment which emphasizes evolution of dust, and do not search to reproduce realistic simulations of galaxies. We therefore start with contradictory initial conditions allowing an initial old stellar population and no dust. Our interest is to look at evolution of dust mass considering the stars formed during the simulation.

	Stellar Miyamoto component			*Gaseous Miyamoto disk*			*Dark matter halo*	
name	*Mass* ($M_\odot$)	*a* (kpc)	*b* (kpc)	*Mass* ($M_\odot$)	*a* (kpc)	*b* (kpc)	*core radius* (kpc)	core mass ($M_\odot$)
`caaa`	6.0×10^8	0.81	0.19	6.0×10^8	2.6	10^{-4}	0.14	10^7
`caab`	7.2×10^8	1.2	0.29	2.8×10^8	3.9	10^{-4}	0.14	10^7
`caac`	2.8×10^8	0.81	0.19	1.1×10^8	2.6	10^{-4}	0.57	10^8
`caad`	5.0×10^8	0.81	0.19	2.0×10^8	2.6	10^{-4}	0.57	10^8
`caae`	5.0×10^8	0.81	0.19	2.0×10^8	2.6	10^{-4}	2.42	10^9
`caaf`	2.2×10^9	2	0.48	8.8×10^8	6.5	10^{-4}	10.2	10^{10}

Table 5.3: Major parameters for simulations of dwarf galaxies and `caaf`, a medium sized galaxy.

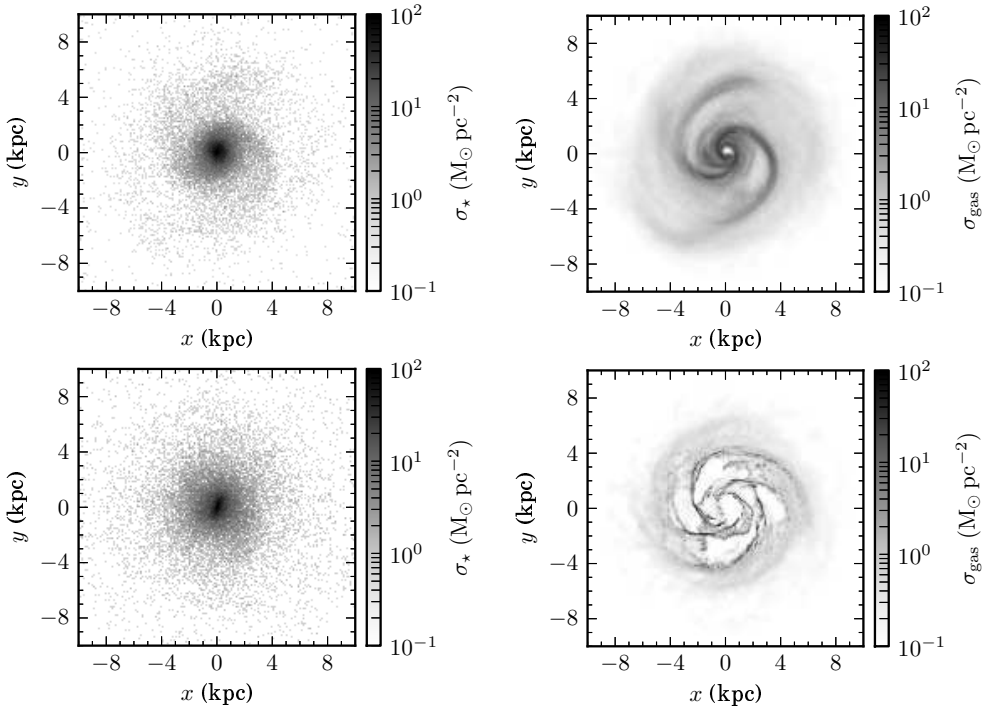

Figure 5.5: xy map of dwarf galaxies `caaa` at 2 Gyr (top) and `caab` at 3 Gyr (bottom).

5.2 Analysis

`caaa` is a simulation with high gas mass fraction. By consequence the galaxy has large patterns, in the gaseous disk as well as the stellar disk, and spirals early appears (before 1 Gyr), then bar forms. When stars form, they deplete a fraction of gas in the center. The spirals progressively fade after few Gyr (Fig. 5.5).

For `caab`, `caac`, `caad`, and `caae`, SF depletes central gas and creates long and thin, either spiraling or circular, filaments. The stellar component has a bar and sometimes weak and transient spirals. With `caaf`, the first SF episode highly depletes gas by ejection, in addition to the formation of filaments.

5.2.1 Evolution of the dust-to-oxygen ratio

For `caaa` Fig. 5.6, evolution of dust-to-oxygen ratio follows three regimes clearly distinguishable. During the first regime, before ~ 3.5 Gyr, the ratio abruptly increases after the first SF peak. After that, SF is episodic with several SFR peaks. During each peak, the ratio rapidly decreases. However dust abundance as well as oxygen abundance increase. Between peaks, SF is quiescent, the ratio increases. Indeed, oxygen abundance is nearly constant while dust abundance continues to increase. The second regime begins with the SF peak at $\sim 4 \times 10^{-3}$ $\mathrm{M}_\odot\,\mathrm{yr}^{-1}$, where dust-to-oxygen ratio, oxygen abundance, and dust abundance increase. A continuous SF follows. The third regime displays an episodic SF like the first, and the ratio decreases while oxygen and dust abundances continue to increase.

For the first regime, SF peaks tend to reduce dust-to-oxygen ratio. Since dust and oxygen abundances increase, evolution is actually related to the respective rates of enrichment for dust

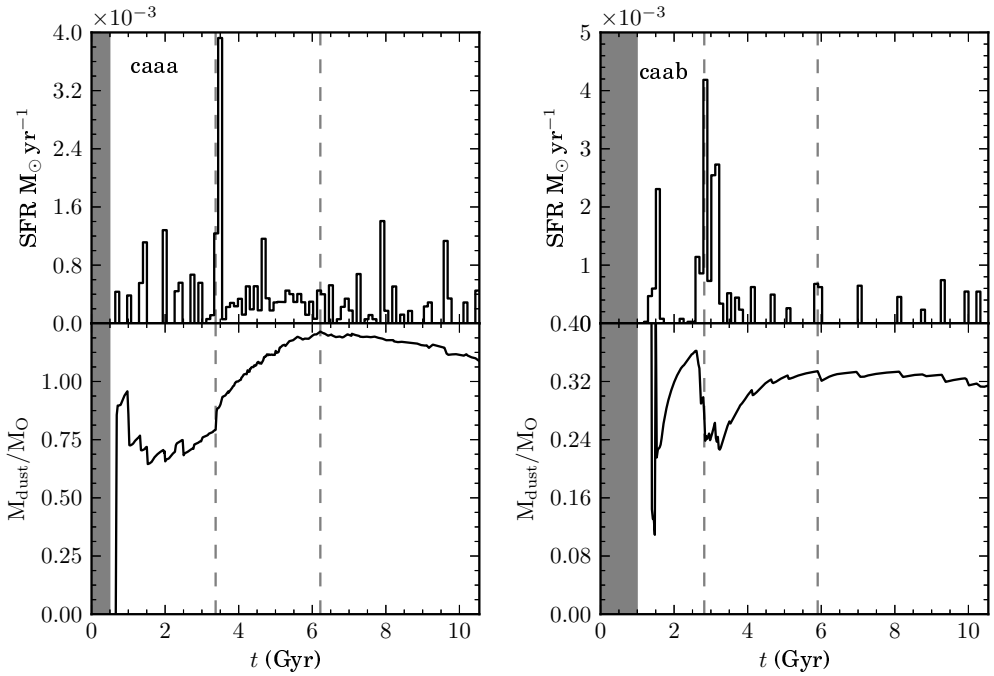

Figure 5.6: Evolution of dust-to-oxygen ratio for `caaa` and `caab` with SFR (bins of 100 Myr).

and oxygen. This means dust is produced at lower rate than oxygen enrichment rate. We have look for two assumptions in order to explain such lower rate for dust production. The first one is that stars themselves enrich the gaseous medium with much more oxygen than dust. Indeed, oxygen rich and dust-poor stellar winds, such that their dust-to-oxygen ratio is lower than the ratio in ISM, will lower the ratio in ISM. Nevertheless the ratio decreases while SF peak occurs, eg. in same time. This implies only SNII have time to enrich ISM. Dust–oxygen mixture from enrichment is therefore likely to be similar to previous mixture also originating from previous SNII enrichment. Indeed, long-lived stars had not so much time to efficiently change dust-to-oxygen ratio during the first few hundred of Myr. One can argue that accretion in ISM increase the ratio. This is actually the case. Indeed, during quiescent periods, oxygen abundance is nearly constant while dust abundance continues to increases. Consequently, stars do not enrich ISM and dust is therefore produced by grain growth. Then, SF peak enriches gas in oxygen and dust, with a dust-to-oxygen ratio lower than the ratio in ISM, lowering the later. In the second possible scenario, dust is efficiently destroyed by shocks produced by SNII. Dust production continues with SNII enrichment, while destruction balances production. Thus, net dust production rate, actually enrichment minus destruction rate, is still positive but reduced. On contrary SNII efficiently enrich ISM with oxygen. This implies a reduction of dust-to-oxygen ratio.

For the second regime, dust and oxygen abundances as well as dust-to-oxygen ratio, increase. The regime begins at 3.4 Gyr with a star formation of $1.2 \cdot 10^{-2}$ $M_\odot\,yr^{-1}$ during 10 Myr while dust-to-oxygen ratio abruptly increases. At ~ 3.5 Gyr, the bigger SF peak of $\sim 4 \cdot 10^{-3}$ $M_\odot\,yr^{-1}$ in 100 Myr bins (or $2.1 \cdot 10^{-2}$ $M_\odot\,yr^{-1}$ in 10 Myr bins) does not impact, either increasing nor decreasing, on dust-to-oxygen ratio. This excludes our first assumption on the effects of dust poor, oxygen rich winds to lower dust-to-oxygen ratio of ISM. Indeed, such effect should have the

same impact on global value, with a trend to the same value (eg. the ratio found in winds), at each star formation peaks. On contrary, previous star formation peak, in the first regime, lowers the ratio below 0.75 while the ratio increases above with the first peak of the second regime. This means destruction was responsible for the decrease of the ratio in the first regime. Since destructive effects are local, in the second regime, destruction is not efficient to destroy large amount of dust, and SNII enrichment actually increases dust-to-oxygen ratio. Moreover, SF is continuous in this regime, as well as dust and oxygen enrichment. In this second regime, dust-to-oxygen ratio continues to increase, with decreasing rate, indicating the influence of long-lived stars and/or a lower production rate of dust, maybe due to less efficient grain growth.

In the third regime, SF retrieves an episodic rate. However, peaks are much less influent in dust-to-oxygen ratio than for the first regime. SNII are therefore negligible when compared to long-lived stars, specially AGB and/or SNIa, decreasing dust-to-oxygen ratio.

For `caab`, the first regime, before $\sim$ 2.5 Gyr, displays an increasing dust-to-oxygen ratio. However, oxygen abundance is nearly constant. Indeed, there is very low SFR in this regime, between the first peak and the second at 2.5–3 Gyr. Hence, there is no or little enrichment from SNII and/or long-lived stars during this regime, and dust grains grow by accretion, increasing dust abundance. The second regime begins with a peak of SF up to 4×10^{-3} $M_\odot\,yr^{-1}$. Dust-to-oxygen ratio quickly decreases while oxygen abundances increases and dust one also increases at lower rate. We have previously seen it is due to destruction, from SNII. After that, during both second and third regime, dust-to-oxygen ratio increases between peak of SFR and decreases when SF occurs. Actually, oxygen abundance is nearly constant between peak, and only short-lived stars like SNII therefore enrich ISM, while dust abundance continuously increases thanks to accretion. In the third regime dust-to-oxygen ratio decreases, while dust and oxygen abundances continue to increase. This implies dust is produced at lower rate than enrichment of oxygen in ISM. This suggests an influence of long-lived stars and/or a lower production rate of dust, maybe due to a less efficient grain growth.

SFH of other simulations `caac`, `caad`, `caae`, and `caaf` look like `caab`: an important SFR during few 100 Myr around $\sim$ 2 Gyr, followed by episodic SF at lower rate. Dust-to-oxygen ratio displays similar behaviour. It increases between SF peaks thanks to accretion, and SNII produce shocks destroying dust and lowering the ratio during SF. During the first important SF episode, the ratio decreases down to a value from 0.07 (`caad`) to 0.15 (`caaf`). After that the ratio increases on long term asymptotically up to 0.23 (`caae`) to 0.27 (`caaf`) and remains stable over Gyrs. Nevertheless, in this third regime, the ratio varies on short term: dust is produced and destroyed approximately in same amount during quiet and SF periods respectively. `caaa`, due to its higher gas mass fraction and SFR, has decreasing dust-to-oxygen ratio during the third regime.

5.2.2 Maps of the dust-to-oxygen ratio

xy maps

`caaa` snapshots from 0.98 to 1.03 Gyr (Fig. 5.7) displays dust-to-oxygen mass ratio which decreases abruptly due to the second starburst. This starburst allows SNII to quickly enrich ISM with oxygen. We obtain similar behaviour at 1.98 Gyr: the ratio decreases down to $\lesssim 1$ in the central part of the galaxy after the star formation of $\sim 1.3 \times 10^{-3}$ $M_\odot\,yr^{-1}$. This destruction is visible for all simulations when stars form. Oxygen abundance quickly increases while dust abundance slowly increases, implying the decreasing ratio. As we have seen in previous section, dust is destroyed when SNII enrich ISM. Dust-to-oxygen ratio decreases, since dust destruction efficiently balances dust production. Although global ratio of Fig. 5.6 increases at $\sim$ 3.5 Gyr, at the center and visible part of the galaxy the ratio actually decreases.

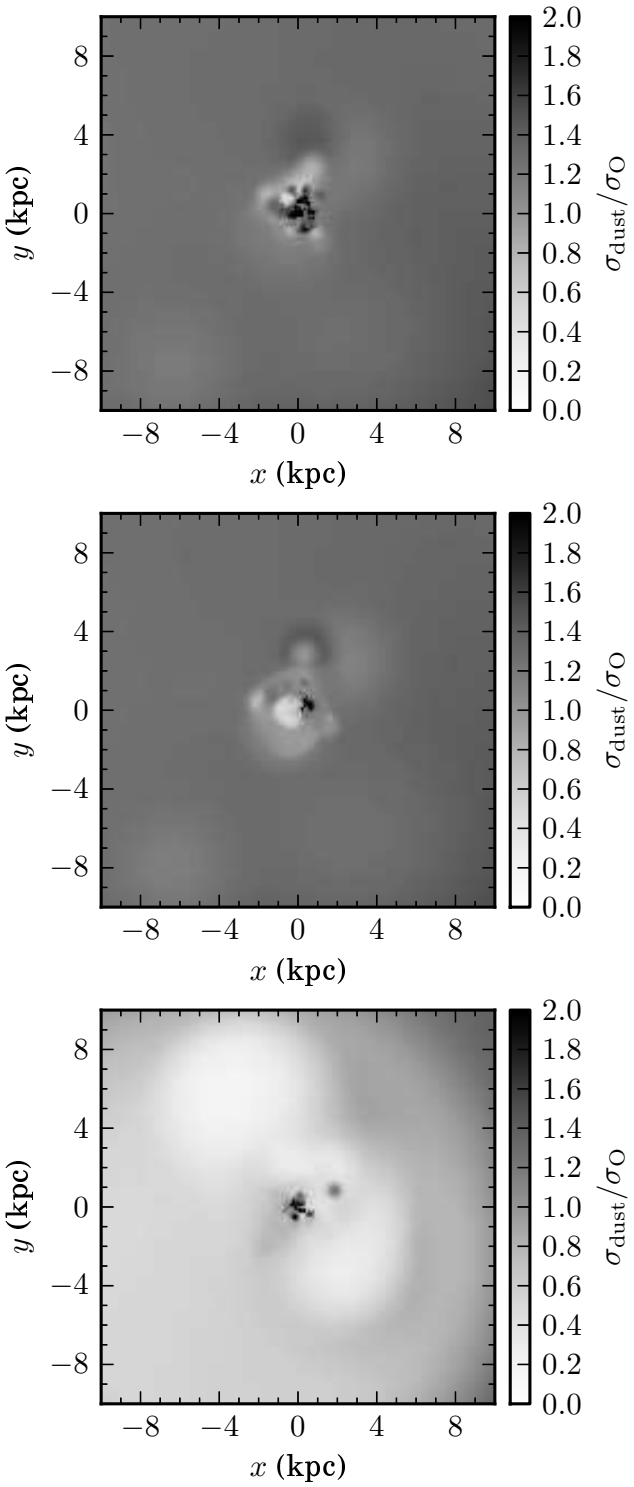

Figure 5.7: xy maps of dust-to-oxygen ratio for the dwarf galaxy `caaa` from 0.98 (**top**), 1 (**middle**), to 1.03 Gyr (**bottom**). σ is surface density.

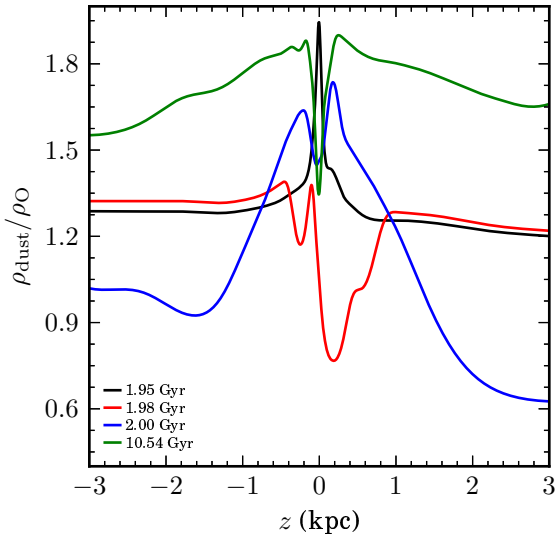

Figure 5.8: z maps of dust-to-oxygen ratio for the dwarf galaxy `caaa` and evolution with time.

Dust and oxygen enrichment firstly occurs at the location of newly formed stars, in the center of the galaxy, then propagates in low density medium. Abundances are lower in arms, with higher density. However, when bar forms later, dust have the highest abundance in this high density and central feature, because of enrichment inside.

`caab` has no large pattern like `caaa`, with arms and/or bar. However, mechanisms of dust and oxygen enrichment remains, with lower dust abundance in denser filaments. `caac`, `caad`, `caae`, `caaf` display similar behaviour.

z maps

We study the SF peak of `caaa` at ~ 2 Gyr, Fig. 5.8. Before SF, disk has higher dust-to-oxygen ratio, up to 2, than the ratio at high altitude ($\lesssim 1.3$). Then, SF lowers the ratio thanks to shocks destroying dust. In the same time galactic winds appear and gas is therefore ejected, specially shocked gas. At 1.98 Gyr snapshot, such gas with dust-to-oxygen ratio as low as ~ 1 is visible at low altitude (± 1 kpc) while in the disk the ratio has decreased. However, the ratio in the disk remains higher than the ratio in the ejected gas. At 2 Gyr, the ratio has increased in the disk and at low altitude such that the ratio in the disk is lower than the ratio out of the disk. Dusty gas has been expelled at higher altitude ($\gtrsim 1$ kpc) by galactic winds. This implies inefficient following destruction when considering all gas mass in the galaxy (see Sect. 5.2.1) but destruction still destroy efficiently dust in the disk. It therefore produces great and fast variation of dust-to-gas ratio, from 2 to 1.

R maps

Like xy and z map, at 1.98 Gyr of `caaa`, dust-to-oxygen abruptly decreases in the center, where stars form, and propagates at higher radius, lowering the ratio while both dust and oxygen abundances increase (see Fig 5.9).

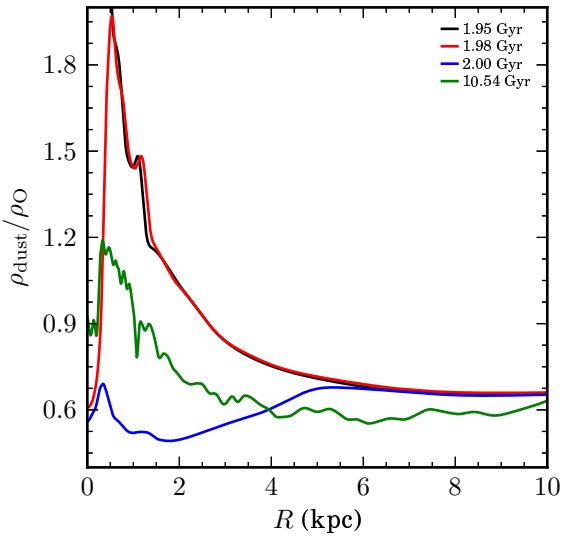

Figure 5.9: R maps of dust-to-oxygen ratio for the dwarf galaxy `caaa` and evolution with time.

Conclusion

New: *Even if we have mainly shown two simulations here, all simulations and maps of dwarf galaxies show similar behaviour.*

- The dust-to-oxygen ratio decreases in the disk while stars form, SN enrich the ISM with oxygen and limit the production rate of dust by shock destruction.
- Dust propagates with oxygen to high altitudes and large radii.
- The dust-to-oxygen ratio in the disk is lower than the ratio out of the disk, specially after star formation.

5.2.3 Local correlation

At 1.476 Myr for `caab` (Fig. 5.10), SF enrich gas because of early SNII events. Gas is also sufficiently rich to have $\mathrm{M_O/M_H} > 10^{-4}$ thanks to SF occurring between 2.5 and 3 Gyrs. On local dust-to-oxygen diagram, gas is distributed below the linear relation designed for massive galaxies (grey line). Moreover, while one snapshot shows the expected increasing dust abundance with metallicity, the two other snapshots display constant dust abundance whatever oxygen abundance of local medium is. This shows dust destruction can be important.

Snapshots can also show the expected linear relation similar to the relation of massive galaxies. It is the case of `caae` at 1.743 Myr. Metal-poor gas is dust over-abundant comparing to global abundance of dwarf galaxies when $\mathrm{M_O/M_H} \gtrsim 10^{-3}$. For oxygen-rich and massive galaxies, distribution of dust abundance of our snapshot agrees with galactic observations.

`caae` snapshots at 2.187 Myr and 2.978 Myr display constant dust abundance over the entire range of metallicity. However $\mathrm{M_{dust}/M_H}$ ranges from 10^{-5} to 10^{-4} at 2.187 Myr, while it ranges from $10^{-4.5}$ to $10^{-3.5}$ at 2.978 Myr. There is a clear increase with time.

Consequently, local abundance of dust does not follow any simple relation with oxygen abundance. This is specially true for dwarf galaxies, allowing great variance of dust abundance for any metallicity.

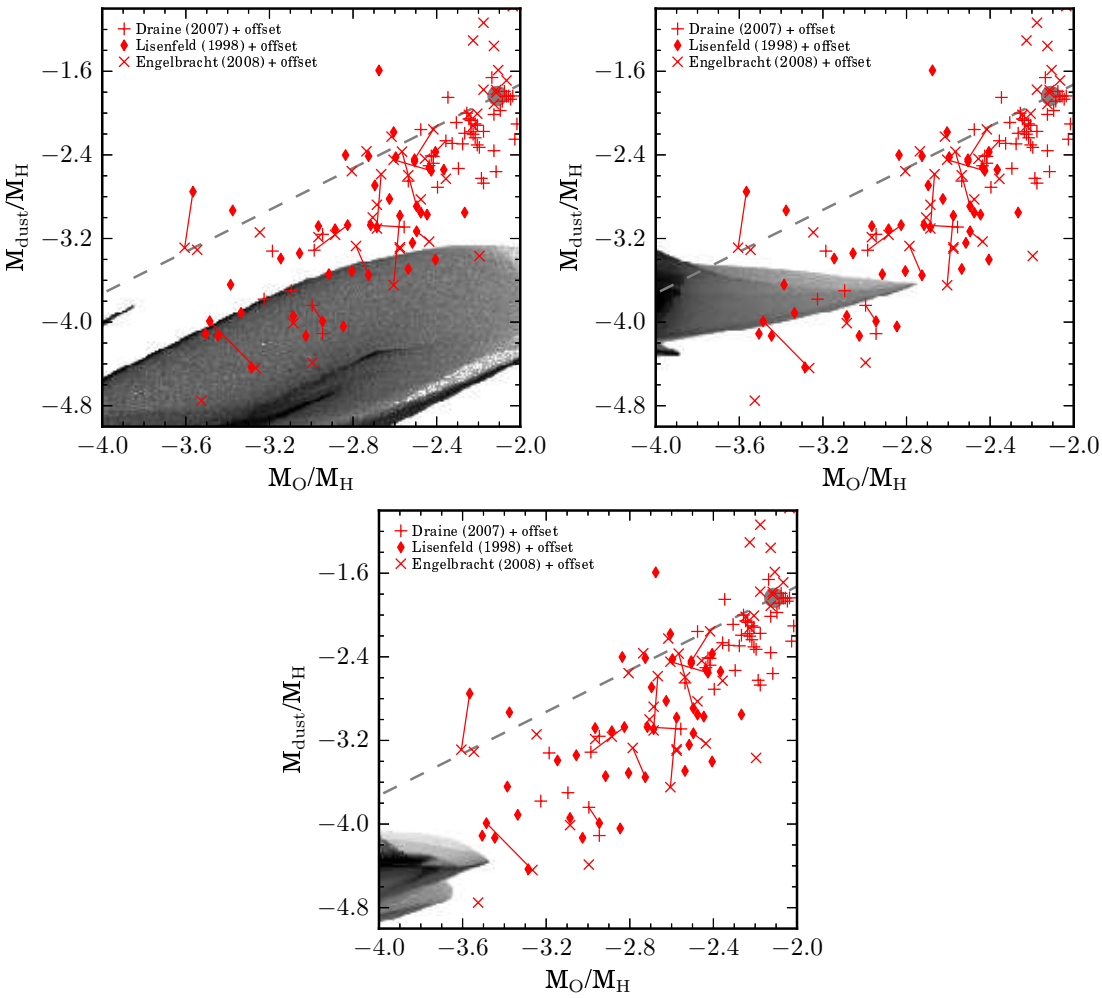

Figure 5.10: Local dust–oxygen diagram of `caab`. **Left:** snapshot at 1,476 Myr. **Right:** snapshot at 2,504 Myr. **Bottom:** snapshot at 3,004 Myr.

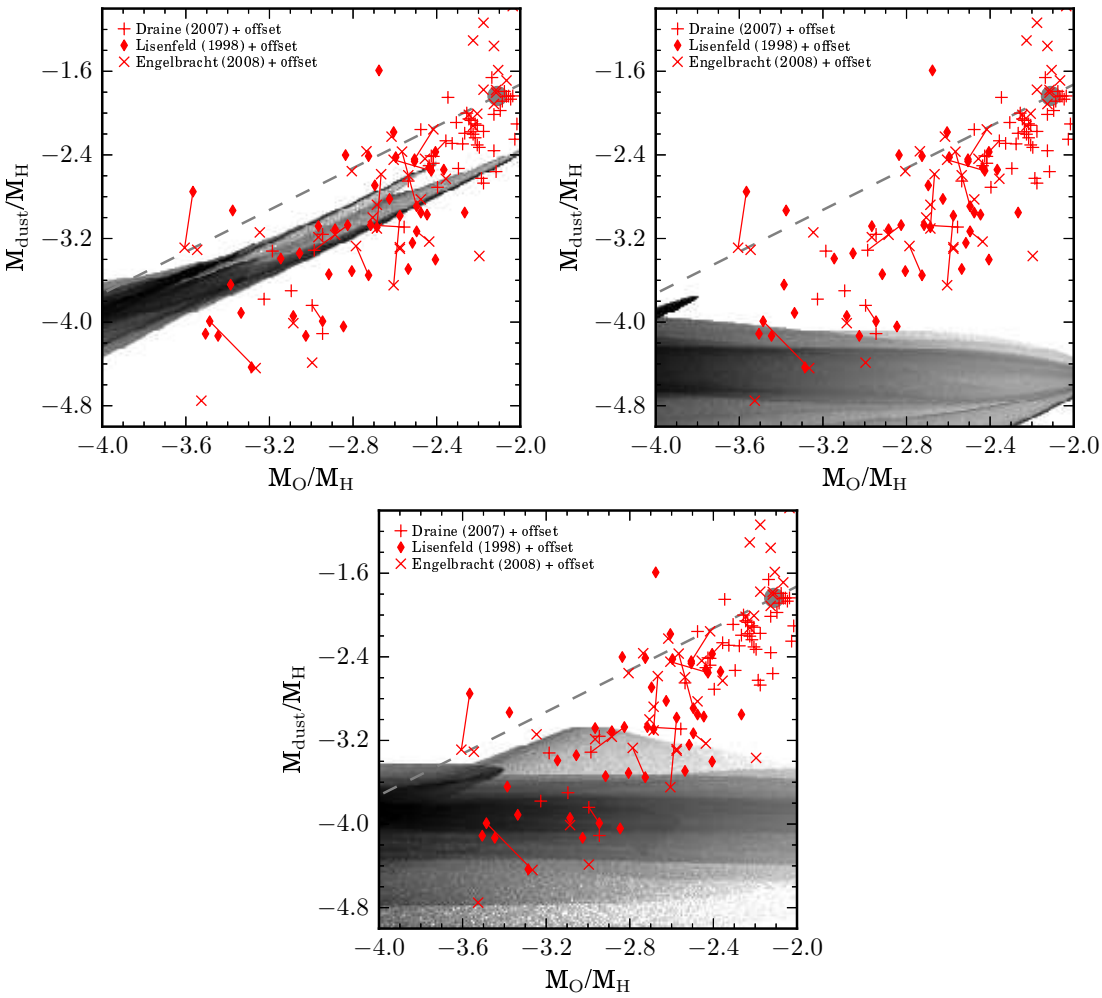

Figure 5.11: Local dust–oxygen diagram of caae. **Left:** 1.743 Myr. **Right:** 2.187 Myr. **Bottom:** 2.978 Myr.

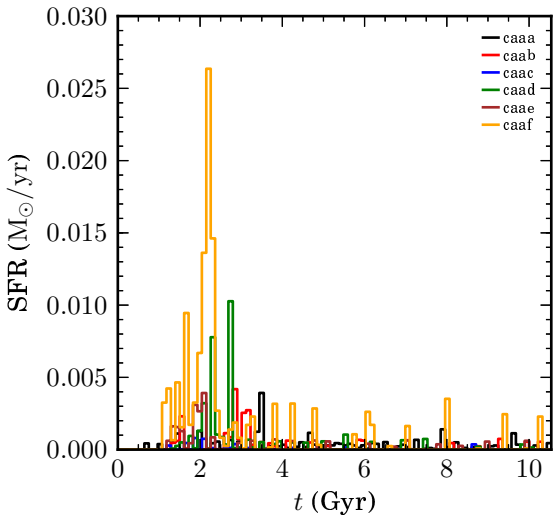

Figure 5.12: Star formation rate of dwarf galaxies, using 100 Myr bin range.

5.2.4 Global correlation

Fig. 5.13 displays dust–metallicity global diagrams for cylinder of three radius $R < 0.1, 0.5, 1$ kpc.

For $R = 1$ kpc cylinder, only `caaf` ($R_{25} \sim 3$ kpc) evolves to medium metallicity. Contrary to massive galaxies, snapshots of dwarf galaxies do not follow smooth path on the diagram. Indeed, metallicity and dust abundances abruptly change between two consecutive snapshots, depending on early enrichment after recent SF episode and propagation to higher radius through winds. `caaf` has the highest SF, up to 26×10^{-3} M$_\odot$ yr^{-1} at ~ 2 Gyr while other simulations have lower SF $< 10^{-2}$ M$_\odot$ yr^{-1}, explaining the better enrichment for this galaxy (Fig. 5.12). Moreover, dust abundance tends to decrease with oxygen abundance. I have previously concluded dust-to-oxygen ratio decreases during SF, due to dust destruction from SNII. This confirms that central gas, where stars form, is more enriched with oxygen and dust more destroyed with SF. However, despite this general trend, dust abundance shows dispersion, from $M_d/M_H = 10^{-4.8}$ to $10^{-3.4}$ for the small range of metallicity around $M_O/M_H \sim 10^{-3.4}$. This result is in agreement with observations of dwarf galaxies by Lisenfeld & Ferrara (1998). For higher metallicity $M_O/M_H \sim 10^{-2.6}$ snapshots have dust abundance lower than expected from observations.

For diagrams with radius $R < 0.5$ kpc, `caaf` displays similar behaviour, with a shift to higher dust and oxygen abundances. This time, snapshots have abundances similar to observations. Due to smaller radius of studied cylinder of gas, snapshots of less massive galaxies `caab`, `caad`, and `caae` ($R_{25} \sim 1$–2 kpc) are also displayed on the diagram, thanks to central star formation occurring in all these galaxies. Like `caaf`, there is no smooth evolving path. Dust abundance is constant or slightly decreases when metallicity increases. Dispersion of snapshots covers the full range of dust abundance given from observations.

For diagram with radius $R < 0.1$ kpc, I look for central part of dwarf galaxies. This allows to display snapshots of all simulations performed since stars form mainly at the center and efficiently enrich gas inside the considered cylinder. Snapshots cover all observed galaxies on the diagram. However, dust-poor and metal-rich snapshots also appear where no observations are found, at $M_O/M_H > 10^{-3.7}$ and $M_d/M_H < 10^{-3.6}$. For `caaa`, a gas rich galaxy, I retrieve a linear relation on the diagram, contrary to other simulations.

In most cases, simulations of dwarf galaxies are able to reproduce observations on the dia-

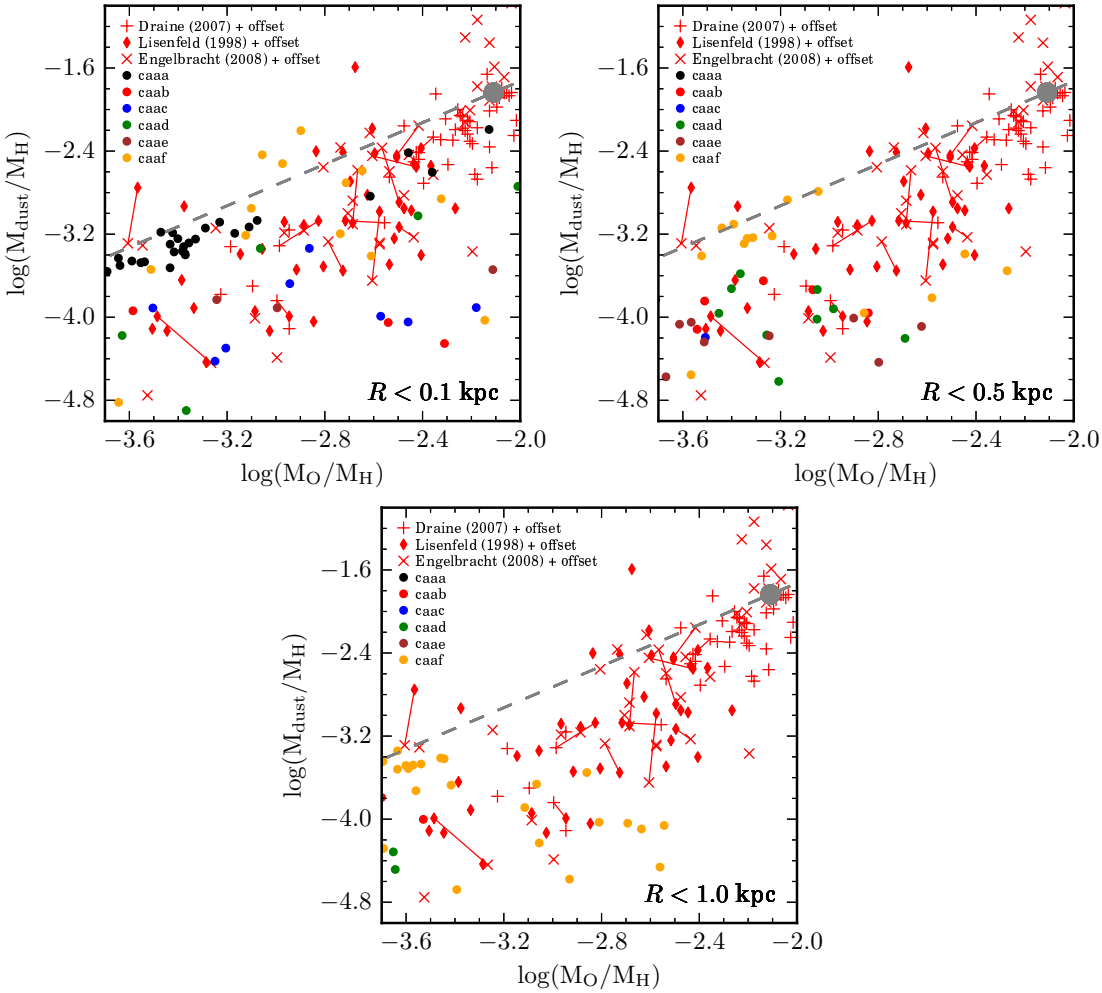

Figure 5.13: Global dust–oxygen diagrams of dwarf galaxies, abundances are taken inside a cylinder of radius $R < 0.1,\ 0.5,\ 1$ kpc from left to bottom. We plot a filled circle for each snapshot.

grams. They do not follow smooth path and reproduce dust under-abundance at low metallicity, contrary to the linear relation found for massive galaxies. Dispersion of dust abundance, for low metallicity range, is in agreement with observations of dwarf galaxies. I explain this by SF peaks. They therefore enrich gas with oxygen and destroy dust through shocks, when SNII are active.

Chapter 6

Conclusion

We have performed numerical simulations with a new model incorporating dust production and destruction processes. AGB and SNe enrichment, accretion in MC, and destruction by shocks from SNe are included. AGB stars allow for 1 Gyr timescale production while production from SNe is a faster process. This production is balanced by destruction from shocks in ISM. The model is designed to be local and fully takes advantage of the chemodynamical code. This allows to remove few assumptions usually included in semi-analytic models. Moreover simulations naturally include local dust production and destruction. The best semi-analytic models need multi-zone approximation, while simulations can describe both dynamic and chemistry in order to allow transport and mixing of dust. We have studied dust evolution over Gyrs for simulations of a massive, Milky Way-like, galaxy as well as dwarf galaxies. For the massive galaxy we have checked various combinations of dust processes: with and without accretion or SNe production. For the dwarf galaxies we have used different sizes and masses up to a medium-sized galaxy. Our main diagnostic tools include dust-to-oxygen profiles and dust–oxygen diagrams.

With the simulations of the massive galaxy, we find we need an efficient dust production process, to help AGB enrichment and to retrieve dust abundance observed for high metallicity galaxies in the local universe. Otherwise destruction from shocks does not allow for such high dust mass. We therefore follow the traditional assumption by adding grain growth in ISM. Moreover, we estimate stardust mass is ~ 10 % of total dust mass at low metallicity and ~ 1 % for high metallicity. We expect different compositions and physical properties for stardust from AGB and dust produced in ISM, since they are not produced with the same mechanisms and the same physical properties of gaseous medium. Indeed, stardust is formed in the atmosphere and winds of AGB stars while accretion occurs in molecular clouds. Each dust specie should therefore have specific emission properties. Since dust mixture depends on metallicity, we expect SED also depends on metallicity. This implies additional difficulty to design SED model in order to fit observations.

Considering the massive galaxy, we have shown that dust production is actually a fast process, provided accretion is included. SNe production is often assumed to explain the amount of dust in young galaxies. However we find a delay of only 100 Myr when we set off SNII production. Hence, SNII seems to be not important to produce dust in early universe, depending on the necessary time from first star formation to age of currently observed quasars. Moreover, we show that dust mass quickly increases in young massive galaxies, up to dust-to-oxygen ratio of metal-rich galaxies observed in local universe. Snapshots therefore follow a smooth path on dust–oxygen diagram. On contrary the dwarf galaxies obviously follow a more chaotic path, due to an efficient dissemination out of center through galactic winds. Indeed, dust-to-oxygen ratio

highly varies with time, inducing high dispersions. In these cases, dust abundance is always lower than predicted abundance from the linear relation derived with massive galaxies. Thus, we are able to reproduce dust abundance observed in real dwarf galaxies. This suggests early massive objects, even if they are metal-poor, can have an efficient production of dust, thanks to accretion, while local dwarf galaxies have lower dust-to-gas ratio.

Since observed dust abundance of metal-poor, dwarf galaxies is often smaller than predicted by the linear relation calibrated for metal-rich galaxies, one can assume, from the results previously exposed, dust mass is underestimated due to the unavailability of FIR/submillimeter data and/or the choice of SED model. However, our simulations show metal-poor, dwarf galaxies are likely to be dust underabundant. With the same model, we are able to describe the linear relation followed by massive and metal rich galaxies while dwarf galaxies are dust underabundant. Moreover, dust abundances of our simulations are in agreement with our corrected diagram from observations. Since emission of dust is hard to understand and dust mass estimation depends on models of emission, uncertainties remain on dust–oxygen diagram. However, our simulations are in agreement without any fit. This provides a good confidence on dust abundances estimated from observations and simulations.

Our result means evolution of dust abundance depends on the mass of the simulated galaxy. Constant dust-to-metal ratio is often assumed in studies. However we show that the ratio is constant only for massive galaxies, and it can be unpredictable for dwarf galaxies, since it varies with time and SFH. Thus it may be of interest to study possible relations of the ratio with mass, morphology, and SFH. Indeed, after an episodic star formation, SNII allows for oxygen and dust enrichment. The latter has slower increasing abundance thanks to shock destruction. Thanks to the local nature of the model, destruction from SNII depends on dust abundance around. Then, global behaviour of dust-to-metal ratio varies at each SF episode, specially for the simulated dwarf galaxies.

We have studied dust-to-oxygen gradients, emphasized dust transport through winds. We confirm gradients are a powerful tool to study dust evolution and processes in a galaxy. We can confirm, with our simulations of a massive galaxy, similar results from semi-analytic models. Relative strength of production and destruction rates change the sign of the gradient. Moreover accretion flattens the gradient.

However, our results challenge semi-analytic models. Indeed the latter implicitly assume there is no radial mixing nor migration of gas. Our simulations show dust disk extends faster than oxygen disk during star formation. Moreover when SNII produce dust, they efficiently disseminate it. This flattens dust-to-oxygen gradient. This effect becomes important for the dwarf galaxies, due to their smaller mass. For them, gradients is highly shaped by transport of dust outside the disk.

To conclude, we hope numerical simulations will be useful to complete theoretical studies about dust in galaxies, in addition to semi-analytical models. With the amazing resolutions reached by infrared space telescopes like Herschel, insight into galaxies are now available. Previous semi-analytical models, well designed for global evolution, cannot describe dust evolution inside galaxies. We have shown chemodynamical simulations should be of interest to study dust processes with a more accurate view inside galaxies, allowing for new results, and to be useful in order to answer and/or to help to solve the main recent debates concerning dust.

An insight into local conditions and history of galaxies is necessary to better understand mechanisms of dust production, transport and destruction. Numerical simulations allow such studies, then they will be powerful with new observations spatially resolved with a good understanding of local SFH. Nowadays, dust and oxygen gradients can be derived and our numerical simulations have shown that they are useful to study these gradients, in addition to the study of the classical dust problems.

Bibliography

Asplund, M., Grevesse, N., Sauval, A. J., & Scott, P. 2009, ARA&A, 47, 481

Barlow, M. J., Krause, O., Swinyard, B. M., et al. 2010, A&A, 518, L138+

Bendo, G. J., Dale, D. A., Draine, B. T., et al. 2006, ApJ, 652, 283

Bendo, G. J., Wilson, C. D., Warren, B. E., et al. 2010, MNRAS, 402, 1409

Bertoldi, F., Carilli, C. L., Cox, P., et al. 2003a, A&A, 406, L55

Bertoldi, F., Cox, P., Neri, R., et al. 2003b, A&A, 409, L47

Bianchi, S. & Schneider, R. 2007, MNRAS, 378, 973

Binney, J. & Merrifield, M. 1998, Galactic astronomy, Princeton paperbacks (Princeton Umiversity Press)

Binney, J. & Tremaine, S. 1987, Galactic dynamics, Princeton series in astrophysics (Princeton University)

Bot, C., Ysard, N., Paradis, D., et al. 2010, A&A, 523, A20+

Bothun, G. D., Mould, J. R., Caldwell, N., & MacGillivray, H. T. 1986, AJ, 92, 1007

Calura, F., Pipino, A., & Matteucci, F. 2008, A&A, 479, 669

Champavert, N. 2007, PhD thesis, Universit Claude Bernard – Lyon 1

Champavert, N. & Wozniak, H. 2007, in Heating versus Cooling in Galaxies and Clusters of Galaxies, ed. H. Böhringer, G. W. Pratt, A. Finoguenov, & P. Schuecker , 409

Cherchneff, I. & Dwek, E. 2010, ApJ, 713, 1

Clayton, D. D. & Nittler, L. R. 2004, ARA&A, 42, 39

Compiègne, M., Verstraete, L., Jones, A., et al. 2011, A&A, 525, A103

Cortese, L., Davies, J. I., Pohlen, M., et al. 2010, A&A, 518, L49+

Cowie, L. L. 1978, ApJ, 225, 887

Cowie, L. L., McKee, C. F., & Ostriker, J. P. 1981, ApJ, 247, 908

Cowley, C. R. 1995, An Introduction to Cosmochemistry

Dale, D. A., Aniano, G., Engelbracht, C. W., et al. 2012, ApJ, 745, 95

Desert, F.-X., Boulanger, F., & Puget, J. L. 1990, A&A, 237, 215

Dopita, M. A. & Ryder, S. D. 1994, ApJ, 430, 163

Draine, B. T. 2009, in Astronomical Society of the Pacific Conference Series, Vol. 414, Cosmic Dust - Near and Far, ed. T. Henning, E. Grün, & J. Steinacker, 453–+

Draine, B. T., Dale, D. A., Bendo, G., et al. 2007, ApJ, 663, 866

Draine, B. T. & Li, A. 2007, ApJ, 657, 810

Draine, B. T. & Salpeter, E. E. 1979, ApJ, 231, 438

Dumke, M., Krause, M., & Wielebinski, R. 2004, A&A, 414, 475

Dunne, L., Eales, S., Edmunds, M., et al. 2000, MNRAS, 315, 115

Dunne, L., Eales, S., Ivison, R., Morgan, H., & Edmunds, M. 2003, Nature, 424, 285

Dunne, L. & Eales, S. A. 2001, MNRAS, 327, 697

Dunne, L., Maddox, S. J., Ivison, R. J., et al. 2009, MNRAS, 394, 1307

Dwek, E. 1998, ApJ, 501, 643

Dwek, E. & Cherchneff, I. 2011, ApJ, 727, 63

Dwek, E., Galliano, F., & Jones, A. P. 2007, ApJ, 662, 927

Edmunds, M. G. 2001, MNRAS, 328, 223

Engelbracht, C. W., Rieke, G. H., Gordon, K. D., et al. 2008, ApJ, 678, 804

Ferrarotti, A. S. & Gail, H.-P. 2006, A&A, 447, 553

Friedli, D. & Benz, W. 1993, A&A, 268, 65

Fukui, Y. & Kawamura, A. 2010, ARA&A, 48, 547

Galametz, M., Madden, S., Galliano, F., et al. 2009, A&A, 508, 645

Galametz, M., Madden, S. C., Galliano, F., et al. 2011, A&A, 532, A56+

Gall, C., Andersen, A. C., & Hjorth, J. 2011a, A&A, 528, A13+

Gall, C., Andersen, A. C., & Hjorth, J. 2011b, A&A, 528, A14+

Gall, C., Hjorth, J., & Andersen, A. C. 2011c, A&A Rev., 19, 43

Galliano, F., Hony, S., Bernard, J.-P., et al. 2011, A&A, 536, A88

Galliano, F., Madden, S. C., Jones, A. P., Wilson, C. D., & Bernard, J.-P. 2005, A&A, 434, 867

Galliano, F., Madden, S. C., Jones, A. P., et al. 2003, A&A, 407, 159

Gehrz, R. 1989, in IAU Symposium, Vol. 135, Interstellar Dust, ed. L. J. Allamandola & A. G. G. M. Tielens, 445–+

Girardi, L., Bressan, A., Bertelli, G., & Chiosi, C. 2000, A&AS, 141, 371

Gomez, H. L., Clark, C. J. R., Nozawa, T., et al. 2012, MNRAS, 420, 3557

Gordon, K. D., Galliano, F., Hony, S., et al. 2010, A&A, 518, L89

Hernquist, L. 1993, ApJS, 86, 389

Hirashita, H. 1999a, ApJ, 522, 220

Hirashita, H. 1999b, A&A, 344, L87

Hirashita, H. 1999c, ApJ, 510, L99

Hirashita, H. 2012, MNRAS, 422, 1263

Hirashita, H. & Kuo, T.-M. 2011, MNRAS, 416, 1340

Hirashita, H., Tajiri, Y. Y., & Kamaya, H. 2002, A&A, 388, 439

Hunter, D. A. & Gallagher, III, J. S. 1985, ApJS, 58, 533

Israel, F. P., Wall, W. F., Raban, D., et al. 2010, A&A, 519, A67

James, A., Dunne, L., Eales, S., & Edmunds, M. G. 2002, MNRAS, 335, 753

James, P. 1991, MNRAS, 250, 544

Jang, M., Im, M., Lee, I., et al. 2011, ApJ, 741, L20+

Jenkins, E. B. 2009, ApJ, 700, 1299

Jones, A. P. 2005, in ESA Special Publication, Vol. 577, ESA Special Publication, ed. A. Wilson, 239–244

Jones, A. P. & Nuth, J. A. 2011, A&A, 530, A44+

Jones, A. P., Tielens, A. G. G. M., & Hollenbach, D. J. 1996, ApJ, 469, 740

Kennicutt, Jr., R. C., Armus, L., Bendo, G., et al. 2003, PASP, 115, 928

Kewley, L. J. & Ellison, S. L. 2008, ApJ, 681, 1183

Kobayashi, C., Tsujimoto, T., & Nomoto, K. 2000, ApJ, 539, 26

Kobulnicky, H. A. & Kewley, L. J. 2004, ApJ, 617, 240

Kormendy, J. & Freeman, K. C. 2004, in IAU Symposium, Vol. 220, Dark Matter in Galaxies, ed. S. Ryder, D. Pisano, M. Walker, & K. Freeman, 377

Kozasa, T., Nozawa, T., Tominaga, N., et al. 2009, in Astronomical Society of the Pacific Conference Series, Vol. 414, Cosmic Dust - Near and Far, ed. T. Henning, E. Grün, & J. Steinacker, 43–+

Kroupa, P. 2001, MNRAS, 322, 231

Krumholz, M. R., Matzner, C. D., & McKee, C. F. 2006, ApJ, 653, 361

Leroy, A. K., Walter, F., Brinks, E., et al. 2008, AJ, 136, 2782

Li, A. & Draine, B. T. 2001, ApJ, 554, 778

Lisenfeld, U. & Ferrara, A. 1998, ApJ, 496, 145

Lisenfeld, U., Israel, F. P., Stil, J. M., & Sievers, A. 2002, A&A, 382, 860

López-Sánchez, Á. R., Dopita, M. A., Kewley, L. J., et al. 2012, MNRAS, 426, 2630

Magrini, L., Bianchi, S., Corbelli, E., et al. 2011, A&A, 535, A13

Maiolino, R., Schneider, R., Oliva, E., et al. 2004, Nature, 431, 533

Mateo, M. L. 1998, ARA&A, 36, 435

Mathis, J. S., Rumpl, W., & Nordsieck, K. H. 1977, ApJ, 217, 425

Mattsson, L. & Andersen, A. C. 2012, MNRAS, 423, 38

Mattsson, L., Andersen, A. C., & Munkhammar, J. D. 2012, MNRAS, 423, 26

McKee, C. 1989, in IAU Symposium, Vol. 135, Interstellar Dust, ed. L. J. Allamandola & A. G. G. M. Tielens, 431–+

McKee, C. F. & Ostriker, E. C. 2007, ARA&A, 45, 565

Meixner, M., Galliano, F., Hony, S., et al. 2010, A&A, 518, L71

Meny, C., Gromov, V., Boudet, N., et al. 2007, A&A, 468, 171

Miyamoto, M. & Nagai, R. 1975, PASJ, 27, 533

Morgan, H. L. & Edmunds, M. G. 2003, MNRAS, 343, 427

Moustakas, J., Kennicutt, Jr., R. C., Tremonti, C. A., et al. 2010, ApJS, 190, 233

Muñoz-Mateos, J. C., Gil de Paz, A., Boissier, S., et al. 2009, ApJ, 701, 1965

Nozawa, T., Kozasa, T., & Habe, A. 2006, ApJ, 648, 435

Nozawa, T., Kozasa, T., Habe, A., et al. 2007, ApJ, 666, 955

Nozawa, T., Kozasa, T., Umeda, H., Maeda, K., & Nomoto, K. 2003, ApJ, 598, 785

Nozawa, T., Maeda, K., Kozasa, T., et al. 2011, ApJ, 736, 45

Oh, S.-H., de Blok, W. J. G., Brinks, E., Walter, F., & Kennicutt, Jr., R. C. 2011, AJ, 141, 193

O'Halloran, B., Galametz, M., Madden, S. C., et al. 2010, A&A, 518, L58

Otsuka, M., Meixner, M., Riebel, D., et al. 2011, ApJ, 729, 39

Pagel, B. E. J. 1997, Nucleosynthesis and Chemical Evolution of Galaxies

Paradis, D., Bernard, J.-P., Mény, C., & Gromov, V. 2011, A&A, 534, A118

Paradis, D., Paladini, R., Noriega-Crespo, A., et al. 2012, A&A, 537, A113

Perley, D. A., Bloom, J. S., Klein, C. R., et al. 2010, MNRAS, 406, 2473

Pilyugin, L. S. & Thuan, T. X. 2005, ApJ, 631, 231

Piovan, L., Chiosi, C., Merlin, E., et al. 2011a, ArXiv e-prints

Piovan, L., Chiosi, C., Merlin, E., et al. 2011b, ArXiv e-prints

Piovan, L., Chiosi, C., Merlin, E., et al. 2011c, ArXiv e-prints

Pipino, A., Fan, X. L., Matteucci, F., et al. 2011, A&A, 525, A61+

Planck Collaboration, Ade, P. A. R., Aghanim, N., et al. 2011a, A&A, 536, A16

Planck Collaboration, Ade, P. A. R., Aghanim, N., et al. 2011b, A&A, 536, A17

Pohlen, M., Cortese, L., Smith, M. W. L., et al. 2010, A&A, 518, L72+

Popescu, C. C., Tuffs, R. J., Völk, H. J., Pierini, D., & Madore, B. F. 2002, ApJ, 567, 221

Reach, W. T., Dwek, E., Fixsen, D. J., et al. 1995, ApJ, 451, 188

Regan, M. W., Thornley, M. D., Helfer, T. T., et al. 2001, ApJ, 561, 218

Salpeter, E. E. 1955, ApJ, 121, 161

Savage, B. D. & Mathis, J. S. 1979, ARA&A, 17, 73

Savage, B. D. & Sembach, K. R. 1996, ARA&A, 34, 279

Seaton, M. J. 1979, MNRAS, 187, 73P

Smith, M. W. L., Vlahakis, C., Baes, M., et al. 2010, A&A, 518, L51+

Tamburro, D., Rix, H.-W., Walter, F., et al. 2008, AJ, 136, 2872

Theis, C. & Orlova, N. 2004, A&A, 418, 959

Thornton, K., Gaudlitz, M., Janka, H.-T., & Steinmetz, M. 1998, ApJ, 500, 95

Tielens, A. G. G. M. 1998, ApJ, 499, 267

Tielens, A. G. G. M. 2005, The Physics and Chemistry of the Interstellar Medium

Todini, P. & Ferrara, A. 2001, MNRAS, 325, 726

Tolstoy, E., Hill, V., & Tosi, M. 2009, ARA&A, 47, 371

Trimble, V. 1995, PASP, 107, 1133

Valiante, R., Schneider, R., Salvadori, S., & Bianchi, S. 2011, MNRAS, 416, 1916

van den Bergh, S. 1962, AJ, 67, 486

van Dishoeck, E. F. & Blake, G. A. 1998, ARA&A, 36, 317

Vassiliadis, E. & Wood, P. R. 1993, ApJ, 413, 641

Veilleux, S., Cecil, G., & Bland-Hawthorn, J. 2005, ARA&A, 43, 769

Vlahakis, C., Dunne, L., & Eales, S. 2005, MNRAS, 364, 1253

Walter, F., Brinks, E., de Blok, W. J. G., et al. 2008, AJ, 136, 2563

Willson, L. A. 2000, ARA&A, 38, 573

Woosley, S. E. & Weaver, T. A. 1995, ApJS, 101, 181

Zhu, M., Papadopoulos, P. P., Xilouris, M., Kuno, N., & Lisenfeld, U. 2011, in Astronomical Society of the Pacific Conference Series, Vol. 446, Galaxy Evolution: Infrared to Millimeter Wavelength Perspective, ed. W. Wang, J. Lu, Z. Luo, Z. Yang, H. Hua, & Z. Chen, 119

Zhukovska, S. & Gail, H.-P. 2009, in The Evolving ISM in the Milky Way and Nearby Galaxies

Zhukovska, S., Gail, H.-P., & Trieloff, M. 2008, A&A, 479, 453

Zubko, V., Dwek, E., & Arendt, R. G. 2004, ApJS, 152, 211

Appendix A

Improvement

We point out that dust could be underestimated when destruction is the dominant process, specially for `no_acc` and dwarf galaxies. Indeed, Jones & Nuth (2011) have revised grains lifetime separately for carbonaceous grains and silicates. They estimate silicates survive through destructive shocks. Thus, silicates have longer lifetime than previously estimated. However, not all of their revisions and error estimations, on SNe rate for instance, are relevant for our work, since they are provided by simulations themselves.

Recipe for dust accretion assumes grains grow at constant rate whatever chemical compounds are formed. This reduces the model into a purely physical collision rate model. We therefore have assumed chemical reactions are not important for the growth rate of the chemical species which deplete. Moreover, we have chosen same accretion rate for all chemical species. However, Jenkins (2009) compiled depletion from line of sight observations for each specie individually. He found that two depletions are always related by a linear equation.

Depletion is defined by

$$[X_{\rm gas}/{\rm H}] = \log[N(X)/N({\rm H})] - \log(X/{\rm H})_{\odot}, \tag{A.1}$$

with X a chemical specie, $N(X)$ the observed column density and $\log(X/H)_{\odot}$ the cosmic reference abundance derived from solar, B-stars abundance and helioseismological studies. The linear relation between chemical depletions allows to define, for each line of sight, a parameter $F_{\star}$ and to have the relation:

$$[X_{\rm gas}/{\rm H}] = [X_{\rm gas}/{\rm H}]_0 + A_X F_{\star}, \tag{A.2}$$

where $[X_{\rm gas}/{\rm H}]_0$ and A_X are parameters common to all lines of sight, depending on chemical specie X.

Dust has a life cycle in ISM. When ISM is dense, grains accrete and dust abundance increases, while a shock through gas destroys dust. Grains can enter in accretion and destruction regime multiple times, depending on evolution of gas. However, the same, linear, relation governs depletions. This means that accretion increases depletion, then destruction acts as a backward step.

$[X_{\rm gas}/H]_0$ is assumed to be the depletion when only stardust exists in ISM, without accretion. However, the value must be taken with caution: errors from cosmic abundances are directly reported on error to depletion from stardust. On contrary, strong conclusions are allowed from the values of A_X.

A result of Jenkins (2009) is that, for highly depleted gas, oxygen depletes much more quickly than other elements forming compounds with oxygen (eg. metallic oxydes, amorphous silicates).

This suggests that the approach which accretes chemical elements into compounds is not necessary to design a model with accretion. Indeed, it seems that accretion rate does not change with depletion, indicating that other compounds are formed to sustain the rate. The propositions of the paper are the formation of carbon or hydrogen compounds (H_2O ice) or O_2.

Then, we assume a constant accretion rate is sufficient to describe grain grow, at least for a first approximation. To check this I have designed a model to introduce a specie dependant sticking coefficient such that:

$$\alpha_X \propto -A_X \sqrt{\mu_X}. \tag{A.3}$$

The formula is derived from a simplification of the eq. 3.13 assuming constant distribution of grain $n_d(a)$ in order to deplete element with the rate A_X found by Jenkins (2009).

I numerically integrate eq. 3.13 with the new sticking coefficient. For initial conditions, I take dust abundances from the work of Zhukovska et al. (2008), eg. stardust comes from a $Z = 2 \times 10^{-2}$, 10 Gyrs, AGB population. ISM have a density $\rho = 300$ cm^{-3} and a metallicity $Z = 2 \times 10^{-2}$, chemical mixture from Asplund et al. (2009). After few attempts, I choose an initial dust-to-metal ratio of 10 %, a value explained hereafter.

This simple model retrieve a nearly linear relationship of depletion of species according to each other. As a consequence of the chosen α_X formula, I retrieve slopes found by Jenkins (2009). Since I do not know the relation between $F_\star$ and the time of accretion t, I empirically choose the function $F_\star = t^{1.8}$ to get a nearly linear depletion when I plot depletion as a function of time.

Indeed, I obtain comparable figures taking results from Jenkins (2009) and my model (Fig. A.1). From comparison between the two figures we can derive some conclusions:

1. The slopes are nearly linear and are compatible with Jenkins (2009), as a consequence of our choice of α_X. Grain size distribution does not seem to be necessary since we have not included its variation.

2. The "zero point" of depletion and $F_\star$ must be changed. This suggests that cosmic reference abundance (for oxygen depletion reference) and offset for $F_\star$ (eg. stardust composition) are not compatible with my model.

3. The initial depletion of C might be due to stardust. Note that this assumption bring a strong constraint on initial dust-to-metal ratio of 10 %. Indeed, this initial depletion of C can be explained as carbonaceous grains produced by AGB stars. This therefore fixes the initial abundance of stardust necessary in ISM. Unfortunately, errors from C initial depletion does not allow to have a good confidence in the 10 % dust-to-metal ratio found.

4. For iron, we obtain an offset. One possible explanation is provided by Jenkins (2009): this can be due to the "degeneracy between the effects of dust depletion and those arising from shifts in the ratio of elements arising from α-capture processes compared to those associated with the iron peak", implying an error on the cosmic reference abundance. A second explanation is the possibility of another source of stardust, locking a high fraction of iron into dust, like SNIa producing iron peak elements and not included in this model.

5. Jenkins, in private communication, also suggests non-zero depletions are due to the fact that some elements (C and Fe) remain locked into dust even after a shock. They could better survive to destruction than other elements.

6. Using simple collision model, with appropriate sticking coefficient, is sufficient to have quite good results of the relative depletion of each specie. This supports our main assumption of a physical collision rate model without compounds formation, specially the model used in our simulations, and allow for an improvement with specific sticking coefficients.

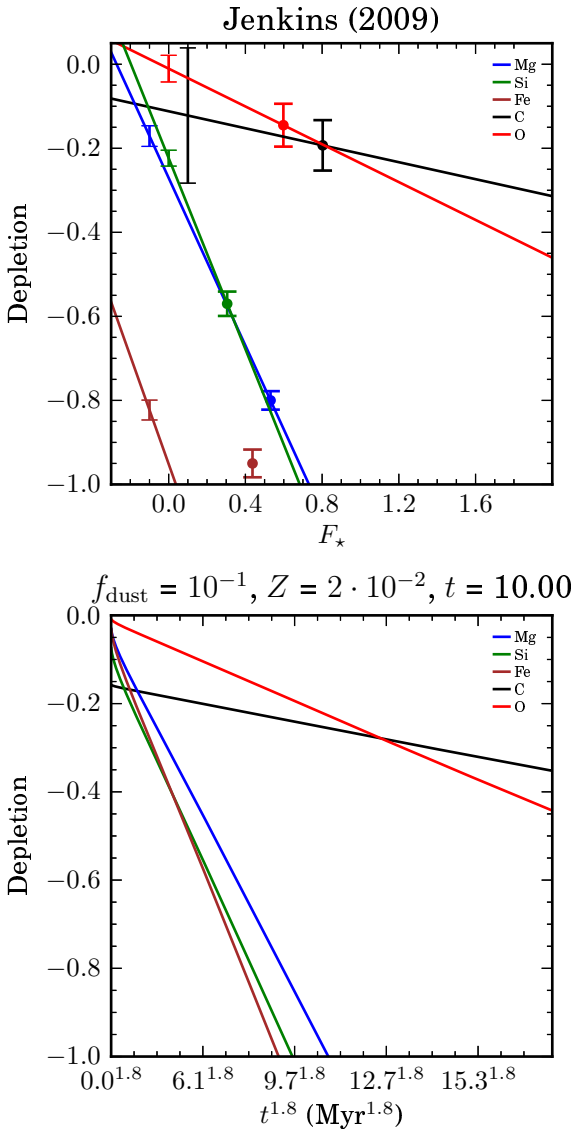

Figure A.1: **Top:** Depletion of the five depleting elements as a function of the global depletion parameter of the line of sight $F_\star$. The lines display the fit found by Jenkins (2009). The error bars with the filled circle show the offset error by vertically shifting the lines, the error bars without circle are the step error by rotating the lines around their filled circle. **Bottom:** Depletion of the five depleting elements as a function of time t. The lines display the model of depletion, with an accretion model including sticking coefficients compatible with depletion rates computed by Jenkins (2009).

By adding multiple grains species, different destructive and growth rate, we should be able to improve the model to derive depletions and physical composition of grains in simulations. This could be helpful to conclude on emission properties of grains depending on local metallicity, mass of simulated galaxies, etc.

Appendix B

Parallelization

In order to speed up simulations, I have done parallelization of few parts of the code. To perform an efficient work, I have first analysed running time of each piece of the program by performing simulations at intermediate state. The code was compiled with `-pg` option, ran, and was analysed with gprof. Results are reported Tab. B.1.

`Findneighstar` consumes most of the time. It is called to find gaseous particles near stellar particles. This function is used to compute energetic feedback and metal enrichment of the stellar component. Then, `findneigh2d` is a similar function to find neighbours within the gaseous component, for the needs of the SPH algorithm. `Accelpar` computes acceleration induced by gravitational forces, while `getphi` computes gravitational potential with numerous FFT. The two last methods have loops which are straightforward to parallelize. The following methods does not show higher performance when they are parallelized. Benefits of parallelization are likely to be balanced by the cost of threads wakeup, memory operations and locking, especially for small loops. This shows that a program not designed for parallelization, specially a program including numerous small loops, cannot easily and fully parallelized.

For neighbours search, the parallelization requires adaptation of the memory structure. The used algorithm takes advantage of a linked list. This means that all neighbours of all particles are sequentially stored in one array: the neighbours of particle i follow the neighbours of particle $i-1$. The number of the neighbours of each particles is stored in another list. Since the parallelized

method	*count*	*total (s)*	*fraction (%)*	*self (s)*
findneighstar	26,227,344	3,796	26.0	3,796
findneigh2d	235,650,000	2,664	18.3	2,664
accelpar	6,854	1,586	10.9	1,586
getphi	4,713	1,757	12.1	1,272
cool_mp_new_cooling	2,141	1,264	8.7	1,074
forces	6,854	4,419	30.3	562
steprk	2,141	5,796	39.8	463
density	6,854	461	3.2	459
star_evol_mp_evolution	2,141	409	2.8	377
getrho	4,769	273	1.9	273

Table B.1: Performances of the sequential code running a complete simulation at low resolution. Array shows the most time consuming methods, the number of call to them, the total time they run including call to other methods, the fraction this represents and finally the time excluding call to other methods.

code does not run sequentially, the new algorithm needs to store, for each particle, the position and size of its list of neighbours. I have adapted the functions computing the list of neighbours, then I have parallelized them.

OpenMP is a powerful tool to parallelize some pieces of code. Unlike MPI which needs a complete adaptation and to manage communications between threads, OpenMP allows a progressive, and easier high-level parallelization. It uses multi-threading approach, eg. computing units share memory in the main case. Thus, it does not allow to run simulations on clusters. However, it is sufficient for usual multi-core systems. OpenMP provides a high-level interface to parallelize loops, asking, in the simplest case, for the selection of the variables specific to each thread. It allows to manage memory in order to avoid concurrent access and/or modification of shared memory spaces.

In few cases, two or more threads need to access to the same array in memory. Locking thread through the appropriate OpenMP instruction has shown bad performances, often lower than the sequential run. I therefore choose to allow a convenient space of memory specific to each thread. However, large arrays are therefore sometimes involved. For instance, to get metal and energy enrichment from stars into gaseous particles, the loop occurs on the stellar particles and, for each simple stellar population they stand for, the neighbouring gaseous particles are found and temporary arrays store feedback. These arrays must be specific to each thread in order to avoid locks at each memory modification. This results in significant consumption of memory.

Finally, I have parallelized the code responsible for $\sim$ 50 % of the running time. For two running threads I therefore expect 25 % of speed increase and obtain between 20 and 25 %.